Pull-out Experiment in Granular Material

by

Yue Zhang

Department of Physics
Duke University

Date: _____

Approved:

_____
Joshua Socolar, Supervisor

_____
Alfred Goshaw

_____
Jian-Guo Liu

_____
Stephen Teitsworth

Dissertation submitted in partial fulfillment of the requirements for the degree of
Doctor of Philosophy in the Department of Physics
in the Graduate School of Duke University
2018

Abstract

Pull-out Experiment in Granular Material

by

Yue Zhang

Department of Physics
Duke University

Date: _____

Approved:

_____
Joshua Socolar, Supervisor

_____
Alfred Goshaw

_____
Jian-Guo Liu

_____
Stephen Teitsworth

An abstract of a dissertation submitted in partial fulfillment of the requirements for the degree of Doctor of Philosophy in the Department of Physics in the Graduate School of Duke University
2018

Abstract

Two-dimensional impact experiments by Clark et al. identified the source of inertial drag to be caused by 'collisions' with a latent force network, leading to large fluctuations of the force experienced by the impactor. These collisions provided the major drag on an impacting intruder until the intruder was nearly at rest. As a complement, we consider controlled pull-out experiments where a buried intruder is pulled out of a material, starting from rest. This provides a means to better understand the non-inertial part of the drag force, and to explore the mechanisms associated with the force fluctuations. The pull out process is a time reversed version of the impact process. In order to visualize this pulling process, we use 2D photoelastic disks from which circular intruders of different radii are pulled out. We check the effect of the initial depth of the intruder, as well as the widths and friction of boundaries. We present results about the dynamics of the intruder and the structures of the force chains inside the granular system as captured by high speed imaging. Before conducting the pull-out dynamic experiments, we first measured the critical pulling force that is needed to pull the intruder out. Under gradually increasing upward pulling force, a steadily strengthening force network forms in response to small displacements of intruder, then eventually fails and the intruder exits the material in a rapid event. We find that just before failure, the force chains bend in a way that is consistent with recent predictions by Blumenfeld and Ma. We found the boundary width together with friction plays an important role in this static pre-failure experiment. However,

the system boundary does not have much effect on the dynamics of the intruder once the pull-out process starts.

To my lovely and wise parents

Contents

List of Figures

List of Abbreviations and Symbols

Symbols

All symbols are also defined properly in the text.

p	The vertical pressure of the corn and the horizontal pressure of the corn.
p_s	The horizontal pressure of the corn. (in section 1.3.2) The pressure on the cylinder surface. (in section 1.3.3)
μ	The friction coefficient between corn and cell wall. (in section 1.3.2) The dynamic viscosity. (in section 1.3.3)
C	The circumference of the square. (in chapter 1) The stress-optic coefficient. (in chapter 2)
L	The side length of the quadratic box.
A	The area of the cross section parallel the bottom of box.
γ	The specific weight of the content.
e	The base of the natural logarithm.
ν	The kinematic viscosity.
$\boldsymbol{u}$	The velocity of incompressible fluid.
C_p	The dimensionless pressure coefficient.
p_0	The pressure in the free-stream flow.
U	The free-stream flow velocity.
ρ	The density of the free-stream flow.
Re	The Reynolds number.

D	The diameter of the cylinder.
I, I_0, I_1, I_2	The light intensity.
λ_l	The wavelength of the light source.
$\sigma 1, \sigma 2$	The two principal stresses.
I(x,y)	The intensity value of the pixel positioned at (x, y) in a photoelastic image.
G^2	The gradient of intensity in pixels,
W_1, W_2	The window functions that specify the subregion in each image.
R_{12}	The cross-correlation function of two subregions of images.
ϕ	The angle between the horizontal line and the left boundary of subregion used to calculate the average intensity in the angular photoelastic response calculation for various boundary widths.
h	The distance from the bottom of intruder to the bottom of granular system.
$D(F_{pulling})$	The intruder's displacement before the failure in the static pre-pull experiments, as a function of $F_{pulling}$.
$F_{pulling}$	The pulling force on the intruder minus the weight of the intruder in the static pre-pull experiments.
F_d	The force exerted by the granular material on the intruder, not including gravity.
v	The intruder's velocity in vertical direction.
$a_{intruder}$	The intruder's acceleration in vertical direction.
t	The time in the dynamic pull-out experiment. t=0 is when the intruder starts to move.However, empirically the t=0 point is chosen at certain velocity or certain displacement of the intruder.
M	Mass of the intruder.
R	Radius of the intruder.
W	The mass of the bottle pulling the thread,
T	The thickness of sample. (in chapter 2) The thread tension. (in chapter 4)

g	is the acceleration of gravity.
α	The angle under which the pressure 'ray' hits the wall. (in chapter 1) The ratio between the drag force and the particle layer thickness above the intruder. (in chapter 4)
β	The ratio between the drag force and the depth of intruder.
d	The depth of intruder.
d_0	The depth of intruder when t=0.
Z	The displacement of intruder.
a_z, b_z	Fitting parameters for the displacement of intruder.
T_p	The thickness of particle layer above the intruder.
T_0	The thickness of particle layer above the intruder at t=0 s.
a_p, b_p	Fitting parameters for the thickness of particle layers above the intruder.
r	The radial coordinate of force chain trajectories in the photoelastic image for the static pre-pull experiment.
θ	The angle between the corresponding radius of the surface point and the free-stream flow's opposite direction. (in chapter 1) The angular coordinate of force chain trajectories in the photoelastic image for the static pre-pull experiment. (in chapter 5)
λ	The slope in the linear fitting between θ and $ln(r)$.
r_0, θ_0	The polar coordinates of the force chain point that is closest to the intruder in the photoelastic image for the static pre-pull experiment.
σ	The stress tensor in the isostatic granular system.
$\sigma_{rr}, \sigma_{\theta r}, \sigma_{\theta\theta}$	The components for the stress tensor in polar coordinates.
$\boldsymbol{\pi}$	The fabric tensor in the isostatic granular system.
$\pi_{rr}, \pi_{\theta r}, \pi_{\theta\theta}$	The components for the fabric tensor in polar coordinates.

Abbreviations

All abbreviations are also defined properly in the text.

CHT	Circle Hough Transform
ODE	Ordinary differential equation.
PIV	Particle image velocimetry.
1D, 2D, 3D	One-, two-, and three-dimensional.
fps	frames per second
FFT	Fast Fourier Transform
PDE	Partial differential equation.

Acknowledgements

"Life is like a box of chocolates, you never know what you're gonna get." This sentence appeared in the 1994 film Forrest Gump. In the summer of 2013, before I came to Duke to pursue my PhD in physics, I stayed in hospital for one week after a surgery. That was the first time I felt so close to death before my doctor told me the tumor was benign. That incident totally reshaped my atitude about life. I feel so grateful that I am alive and have the chance to study at Duke. I feel even more grateful that I was caught by my advisor Prof. Robert Behringer after the first midterm exam of Classical Mechanics. That was the first time I got a grade of 30/100 in my life and I was asked for a special meeting with Bob.

I have no idea (even today) why Bob wanted me to study with him in his research group, as I did a poor job in his Classical Mechanics class. But I have to say I am really lucky to have such a nice and cute advisor. Although sometimes I could not quite get his point in some jokes. Most importantly, Bob is really patient with me when I have some dum questions about experiments or data. Without patience from Bob, I could not complete my thesis for sure. I really appreciate that I have such a brilliant and patient PhD supervisor.

I want to acknowledge not only Bob, but also everyone in LTB group. It is a great experience to work with smart and kind people. In my first year in LTB group, Abe Clark trained me on his impact experiments and his fabulous MATLAB code structure. Hu Zheng helped a lot with my experiment apparatus and he always gave

smart suggestions on the improvement of pull experiments apparatus. Dong Wang helped me most with his strong background knowledge in granular materials. Yuchen Zhao proposed the 3D version of pull experiments. Yiqiu Zhao always knows how to plot a graph with beautiful colors and symbols. Cacey Stevens Bester gave me a lot of suggestions on my presentations. David Chen is good at asking questions on the data. Aghil Abed Zadeh is really an expert in analyzing all kinds of noises. Meimei Wang is patient to help me place particles. Payman Jalali did a lot of work on the 3D version of pull experiments, which is a great supplement of 2D pull experiments.

Additionally, I also want to acknowledge my dissertation committee members: Prof. Alfred Goshaw, Prof. Jian-Guo Liu, Prof. Joshua Socolar, and Prof. Stephen Teisworth. They have provided various perspectives for the same physical problem met in my experiments.

I want to acknowledge my parents, Daowen Zhang and Rong Zheng, for their selfless love and support to pursue my goal. Last but not least, I want to acknowledge all my friends, Fang Liu, Ziyu Qing, Jianwu Gong, Mengqi Ruan, et al., for the joy and encouragement they have brought.

1

Introduction

1.1 General properties of granular material

A granular material is an aggregation of macroscopic particles with diameters greater than 10 μm. For example, snow, sand, coal and fertilizer all belong to granular materials. Because of the macroscopic size of the particles, granular materials will not be affected by thermal fluctuations. However, no matter when these particles in granular materials interact with each other, energy loss will occur. Behaviors of granular materials are very complex: sometimes they can flow like fluid, e.g. quicksand, while sometimes they can stay static like a solid, e.g. a sand castle, other times they can also act like gas, e.g. a sandstorm. (Jaeger et al., 1996)

The discreteness of granular matter greatly affects the complexity of granular properties. Particles compared with their neighbors can have very different force configurations and dynamical motions. Therefore, a granular system may not be well described by traditional hydrodynamics, using macroscopic quantities with length scales much larger than the typical microscopic scales set by particle sizes.

To understand the behaviors of particle packings, many systems have been stud-

ied, e. g. impact experiments, compression experiments, shear experiments et al.

1.2 Motivation of pull-out experiment

The initial enthusiasm for this pull-out experiment comes from a number of impact experiments (Katsuragi and Durian, 2007; Nordstrom et al., 2014; Tsimring and Volfson, 2005; Clark et al., 2012), in which multiple collisions with the network determined by the forces exerted on the intruder were discovered. However, the specific cause of the force fluctuations still remain unknown. As a comparison and alternative, I started to work on controlled pull-out experiments to explore the mechanisms associated with these fluctuations. The pull out process is, to some extent, the time reverse of the impact process. This pull-out experiment reveals interesting new results. Additionally, the pull out process from a granular material has many applications for pilings and buildings.(Nusier and Alawneh, 2004; Krishna and Murty, 2013)

1.3 Related phenomena

There are several phenomena closely related with this pull-out experiment, e.g. granular impact, Janssen effect, and fluid flow around an infinite cylinder.

The granular impact is the reverse process of the dynamic pull-out experiment in some perspective, as shown in the Fig.1.1 and Fig.1.2. Janssen effect shows the frictional boundary's effect on the internal pressure in the granular system, which also affect the static pre-pull experiment.Fluid flow around an infinite cylinder is one fluid version for the dynamic pull-out experiment with circular intruder. There are some interesting similarities when comparing those phenomena with the pull-out experiment, though some difference can still be found.

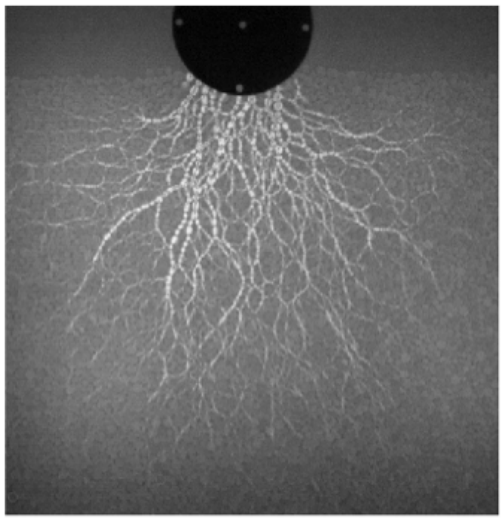

FIGURE 1.1: Typical image(Clark et al., 2015) in A.H. Clark's impact experiments in quasi-2D photoelastic granular particles with diameters 6 mm and 9 mm with elastic modulus of 10 MPa. The circular intruder radius is 6.4cm. In this experiment, the intruder freely falls on the quasi-2D particle bed from certain heights. As shown in the image, bright parts are particles inside the granular system experiencing force and the black part in the middle top is small part of the circular intruder.

1.3.1 Impact

Impact and the corresponding energy loss in granular material have attracted attention at least since 1829 (Poncelet, 1829). Recently, there have been much more research (Tsimring and Volfson, 2005; Katsuragi and Durian, 2007; Clark et al., 2012; Nordstrom et al., 2014) about impact in granular material. When an intruder hits a granular material, such as sand, the velocity of the intruder decreases due to the force exerted by the granular particles. Impact in granular materials is particularly common in applications, including spaceship landings and ballistic trajectories.

The goal of past research has been to understand the dynamics of the impact in this complex system of granular material. A slow dynamics model of the impact has been established through empirical results from experiments with intruders that have much smaller velocities than the acoustic velocity in granular materials. The force

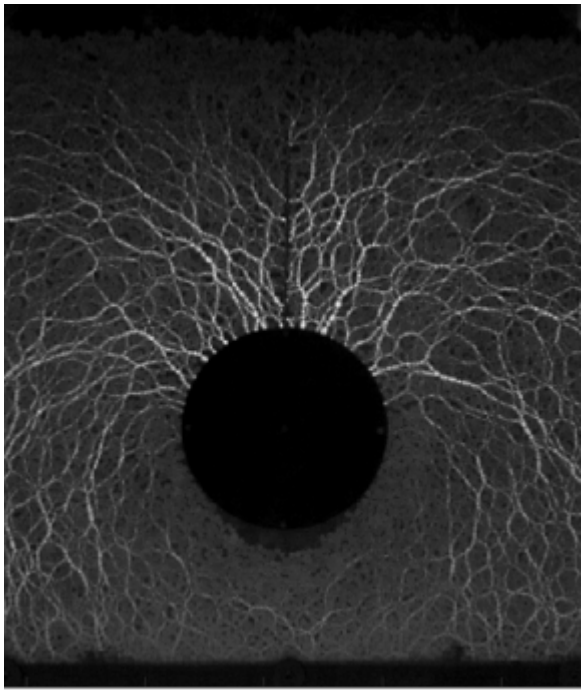

FIGURE 1.2: Typical image in dynamic pull-out experiments in quasi-2D photoelastic granular particles with diameters 6 mm and 9 mm with elastic modulus of 1 MPa. The intruder radius is 10.2cm. In my quasi-2D pull-out experiments, the intruder is buried inside the granular materials and pulled out with a constant force. Bright parts are particles inside the granular system experiencing force and the black part in the middle is the circular intruder.

exerted upon the intruder is composed of three parts: the intruder's gravitational force, a static force, and an inertial force. The gravitational force is the result of interaction between the intruder and the earth, which has no relationship with granular materials. However, the static force and the inertial force both arise from the granular material. In some experiments, the inertial term is known to be proportional to velocity squared of the intruder with a multiplicative factor that may depend on depth and shape.(Katsuragi and Durian, 2007; Umbanhowar and Goldman, 2010; Clark et al., 2012) It is called inertial term because it models the momentum and also energy transfer processes from the intruder to the particles of granular material. The static term is thought to be a function of only depth, which matters most in the

later period of the impact. This term plays an important role when the intruder is in the almost static state.

Although these macroscopic force laws can describe the intruder's trajectories on average, the deceleration of the intruder is not as smooth and simple as described by this force law. Dominated by large fluctuations, the deceleration can be connected to intermittent force pulses which carry energy and momentum away into the granular material.

Using high speed imaging experiments, A. H. Clark et al have established a collisional model(Clark et al., 2015) to connect macroscopic force laws to a grain-scale description.This approach sheds light on the stress on the intruder boundary and its space-time correlations with intruder velocity.

1.3.2 Janssen effect

In order to improve corn and fruit depositories, storage and transportation, the strength of storage silos has been widely explored. H.A. Janssen, who was a German engineer, explained novel behavior of granular materials in his paper in 1895. From simple experiments with corn he inferred the saturation of pressure with increasing depth of granular systems. Additionally, Janssen derived a formula for pressure vs. depth for a granular material from the assumption that the walls carry part of the weight. In Janssen's paper, he also mentioned earlier works: in 1829 Huber Burnand demonstrated the pressure saturation qualitatively, and Hagen predicted the saturation of pressure in 1852. I will briefly discuss Janssen's work.

In Janssen's experiments, four different wooden cuboidal boxes with horizontal side lengths of 20, 30, 40, and 60 cm are used. A box is mounted on four screws S, as is shown by Fig.1.3. The lower end of the box is separated by a movable base. This base is counterbalanced by weights on the plate G. The corn is weighed before being poured into the apparatus. The box is only filled up to the point where plate G with

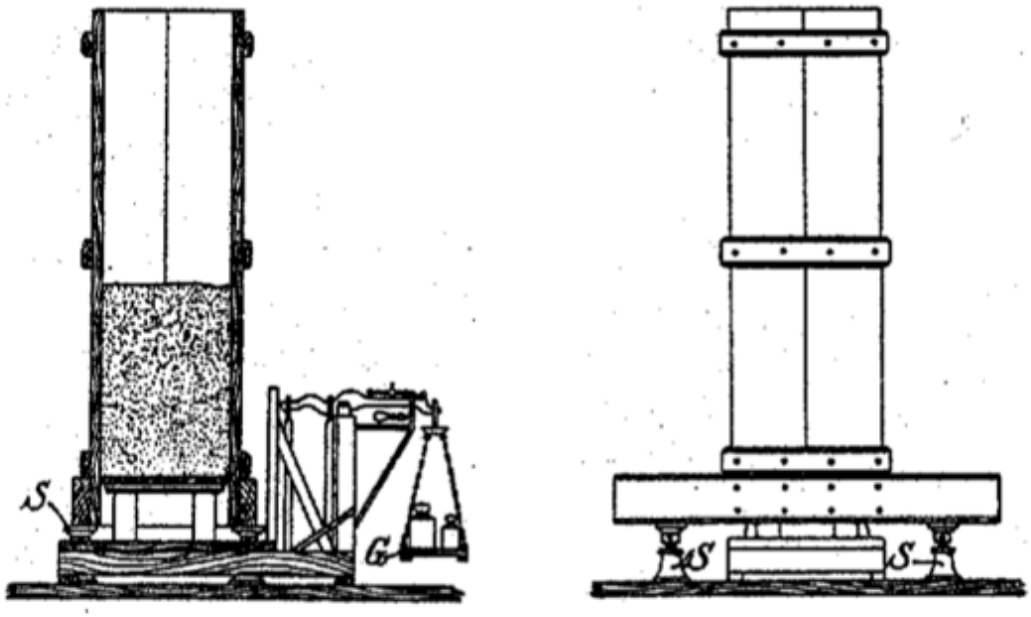

FIGURE 1.3: Apparatus for Janssen's Experiments(Janssen, 1895). A box is mounted on four screws S. The lower end of the box is separated by a movable base, counterbalanced by weights on the plate G. The box is only filled up to the point where plate G with the applied weights starts moving upwards from its center position. Weighing the remaining corn in the container, one can determine accurately the quantity of corn that is causing the pressure at the base.

the applied weights starts moving upwards from its center position. Weighing the remaining corn in the container, one can determine accurately the quantity of corn that is causing the pressure at the base. After placing an additional weight on the plate G, the apparatus is lifted with the screws S to the point where the balance is in equilibrium again. In this way it was possible to determine the bottom pressure for various filling heights while filling the box just once.

The results of Janssen's Experiments for boxes with side lengths of 20cm to 60cm are displayed in Fig. 1.4. The smooth and similar curves of the observed pressure

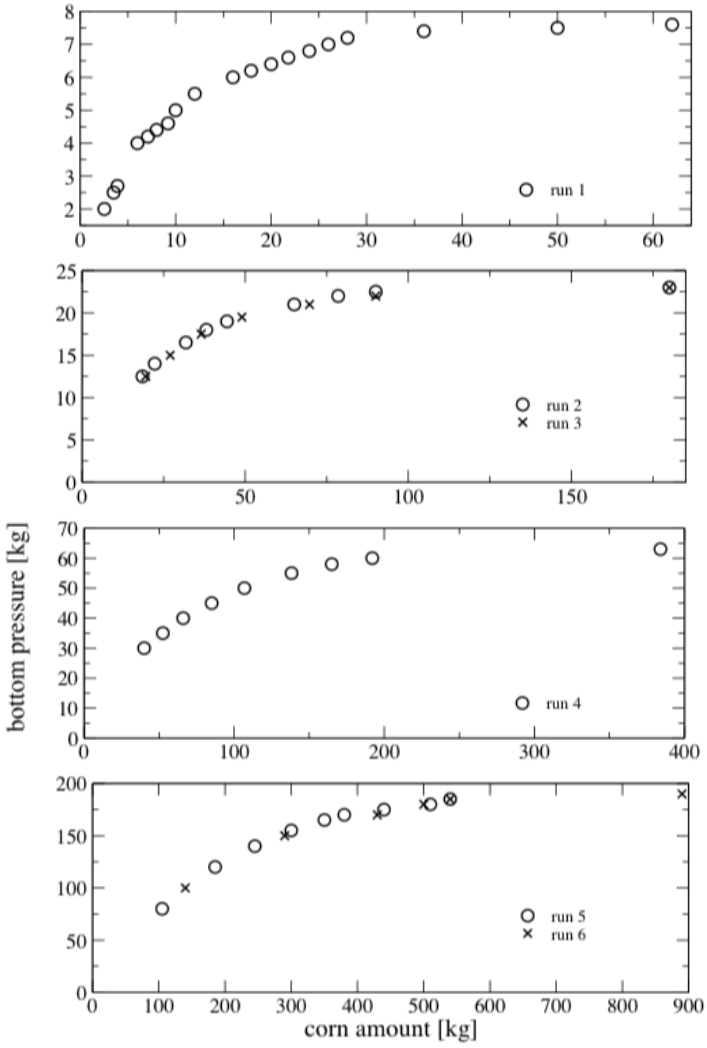

FIGURE 1.4: Graph of bottom pressure vs. corn amount for boxes with widths 20 cm, 30 cm, 40 cm, 60 cm in Janssen's ExperimentsJanssen (1895). At first, when more corn is poured into the box, more pressure the bottom will feel. Saturation of the bottom pressure appears for every box size.

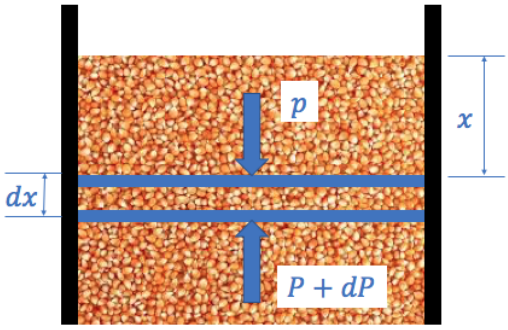

FIGURE 1.5: Jasssen's model to explain the pressure difference

persuade us that these observations are correct. If the content inside the box were a liquid, the bottom pressure would be equal to the weight of the box's content. The experiments with corn, however, yield a much smaller bottom pressure.

Janssen constructed a model for granular materials to explain this huge difference in pressure from a liquid, as shown in 1.5. From the balance of vertical forces on that layer of corn, differential equation can be written as:

$$A(p + dp - p) = \gamma A dx - \mu p_s C dx, \tag{1.1}$$

with boundary condition p(x=0)=0. Here, x=0 corresponds to the top of the layer.(Janssen, 1895)

After solving the above Eq.1.1, the expression for the pressure is as follows:

$$p(x) = \frac{L\gamma}{4K}(1 - e^{-4K\frac{x}{L}}) \tag{1.2}$$

In Eq. 1.1 and Eq. 1.2 , p is the vertical pressure of the corn, p_s is the horizontal pressure of the corn exerted on side walls, μ is the friction coefficient between corn and cell wall, K $= p_s\mu/p$, which is around 0.2, can be given by experiment data , L is the side length of the quadratic box, C=4L is circumference of the square, A is the area of the cross section parallel the bottom of box, which equals L^2, x is the

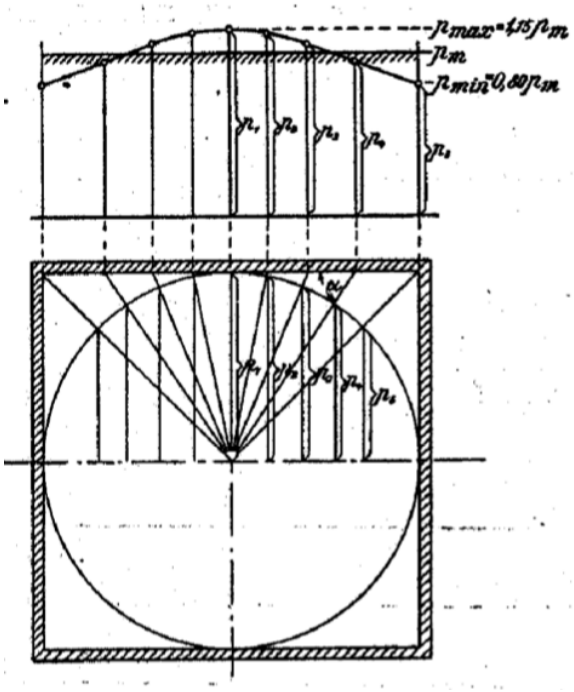

FIGURE 1.6: Jasssen's assumption on horizontal pressure distribution(Janssen, 1895)

filling depth of the corn in the box, γ is the specific weight of the content, e is the base of the natural logarithm. The friction coefficient μ, measured by Janssen with another small experiment by horizontally pulling a wood above the corn, is around 0.33. This indicates that, on average, $p_s \approx 0.7p$.

Additionally, Janssen has made some assumptions(Janssen, 1895), as is shown in Fig. 1.6. The first assumption is that near the corners of the square, the pressure is lower than this mean value, while it is higher in the center part of the walls. The second assumption is that the pressure is transmitted to the side walls radially from the center and exerts a pressure against the wall of p$sin\alpha$, with α being the angle under which the pressure 'ray' hits the wall. The maximum pressure against the wall, around 1.15 of the mean pressure, is reached in the middle of the cell wall, or $p_{s_{max}}$= 1.15· 0.7· p≈ 0.8 p.

Janssen's experiments and model(Janssen, 1895, 1896) greatly improved silo de-

sign. As Sperl (Sperl, 2005) notes, Janssen's paper had been cited 40 times before 1977. Between then and 2005, it has been cited 375 times. This indicates increasing interest in the Janssen effect in granular physics. As will be shown later, Janssen's experiment is helpful in understanding my pre-pull experiment described later.

1.3.3 Fluid flow around an infinite cylinder

In fluid mechanics, flow around a transverse circular cylinder is a classical problem. Many related calculations and experiments have been done for hundreds of years. For inviscid, incompressible fluid around a cylinder, unlike a real fluid, the analytical solutions indicate zero drag on the cylinder, which is well known as d'Alembert's paradox.

The incompressible Navier-Stokes equations without internal source are as follows:

$$\frac{\partial \mathbf{u}}{\partial t} + (\mathbf{u} \cdot \nabla)\mathbf{u} - \nu \nabla^2 \mathbf{u} = \mathbf{g}, \tag{1.3}$$

where $\nu = \frac{\mu}{\rho_0}$ is the kinematic viscosity. There is an analytical solution of Navier-Stokes equation (Eq. 1.3) for fluid flow around a sphere in low Reynolds number region. However, Stokes cannot take the convective term ($(\mathbf{u} \cdot \nabla)\mathbf{u}$) as a small correction to get an analytical solution for an infinitely long cylinder in low Reynolds number flow, as what he has done for a sphere. Proudman and Pearson (Proudman and Pearson, 2006) have used expansion methods to get an approximation for the solution for a circular cylinder in low Reynolds number flow. More recent work, with the help of computers, have been done for higher Reynolds number flow around the cylinder with different boundary conditions.

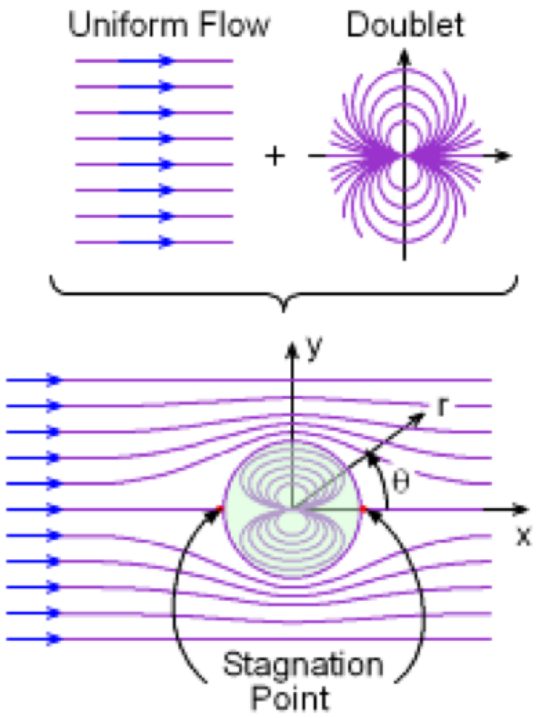

FIGURE 1.7: Flow around a fixed circular cylinder, considered as superposition of uniform flow and doublet.(Gramoll, 2017)

Potential flow around an infinitely cylinder

Potential flow around a fixed circular cylinder is a classical solution for an inviscid, incompressible fluid flowing around a transverse cylinder. The flow far from the cylinder is uniform with constant velocity. The space is infinitely large in this case with no other boundaries. Here flow has no vorticity and no viscosity and thus can be regarded as potential flow. Unlike a real fluid, this solution indicates no net drag force on the cylinder, a result known as d'Alembert's paradox.

Besides calculating the velocity directly from the Laplace's equation for the flow potential, flow around a circular cylinder can be obtained by combining uniform flow with a doublet flow, as shown in Fig. 1.7. A doublet flow is a superposition of a sink and a source with the same strength.

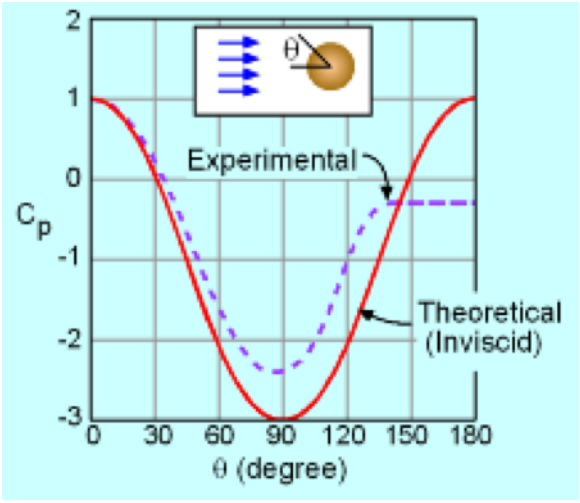

FIGURE 1.8: Comparison between Experimentaland Theoretical C_p (Gramoll, 2017), where C_p is the dimensionless pressure coefficient.

$$C_p = \frac{p_s - p_o}{\frac{1}{2}\rho U^2} = 1 - 4\sin^2\theta, \tag{1.4}$$

where C_p is the dimensionless pressure coefficient, p_s is the pressure on the cylinder surface, p_o is the pressure in the free-stream flow, U is the free-stream flow velocity, ρ is the density of the free-stream flow, θ is the angle between the corresponding radius of the surface point and the free-stream flow's opposite direction. This C_p is called theoretical value of the dimensionless pressure coefficient. Also, experiments can give this empirical value of the dimensionless pressure coefficient.

The discrepancy between the experimental and theoretical C_p is shown in the Fig. 1.8 (Gramoll, 2017). This difference is due to the viscous effects.

Low Reynolds number flow around a circular cylinder

The problem of determining the steady flow past fixed bodies in a slow uniform stream of viscous incompressible fluid was first considered by Stokes (1851), and has been discussed subsequently by many authors like Oseen (1910). (Stokes, 1851;

Oseen, 1910)

With very few exceptions, however, these authors have been concerned with finding the flow past various shapes of body in the limit of zero Reynolds number. Yet many of the effects that arise when the Reynolds number is not negligibly small are also of considerable physical and mathematical interest.

The flow around a circular cylinder in steady cross-flow is extensively studied and Zdravkovich (Zdravkovich, 1997)presents a thorough review of this work. The governing parameter for viscous flows is the Reynolds number, expressing the ratio of inertia to viscous forces. The Reynolds number is defined as: $Re = \frac{UD}{\nu}$. Here U is the free-stream flow velocity, D is the diameter of the cylinder and ν is the kinematic viscosity.

The flow around cylinder is characterized by the formation of a wake depending on Re. Fig.1.9 (a)-(f)(Sumer and Fredse, 1997) depicts the flow around a circular cylinder in uniform cross-flow for different Re below 162. For circular cylinders at $Re > 47$ (Norberg, 2003), the wake is characterized by the eddies which are shed at a frequency.

For our dynamic pull-out experiments, the granular particles flow is a low Reynolds number case, with similar flow folder as the fluid flow folder with Re=32. The flow folder will be shown clearly in the unpolarized videos taken during the dynamic experiments.

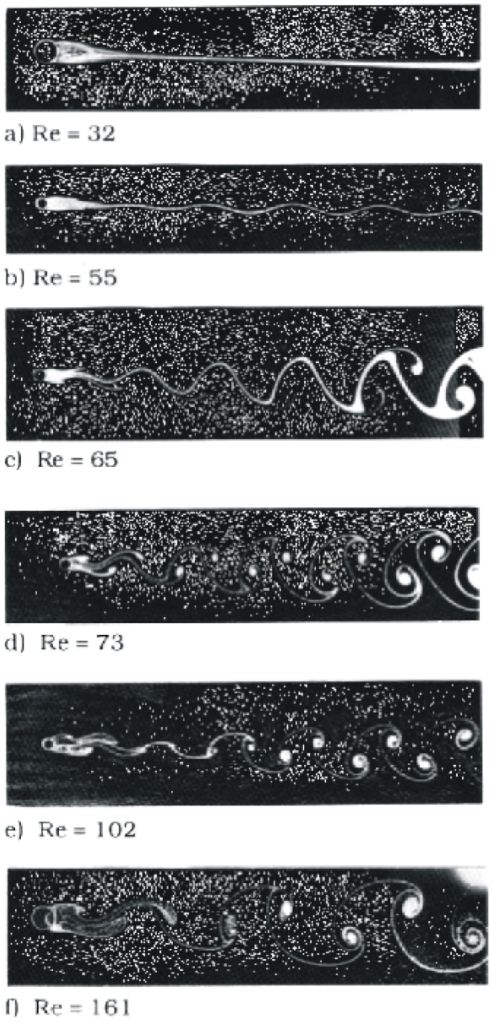

FIGURE 1.9: (a)-(f) Flow around a circular cylinder for different Reynolds number. (Sumer and Fredse, 1997)

2

Experiment Design

The idea behind this pull-out experimental design is to provide a way to understand the dynamics of the circular object pulled out from a granular material and the response of the granular system during the pulling process. For a complete description of the pull-out experiment, it is desirable to have information on the intruder trajectory as well as the particle flow fields and stresses. For this reason, we designed and built the granular system with small quasi-2D photoelastic disks placed inside the walls made of two big transparent glass plates. The glass plates are fixed to aluminum frames.

The other problem that needs to be solved is how to provide a pulling force. The idea is to provide a constant pulling force statically. So we connect the circular object through a string above two pulleys with a bottle of water, whose weight can be continuously changed and measured before the experiment. Now the question is how much water should be added to the bottle to pull the buried object out from the granular materials. So we designed a pre-failure experiment during which we keep adding small quantized weights on the bottle side until the critical pulling force that breaks the granular system and pulls the object out is reached. Those

quantized weights are made of plastic bags with certain numbers of small steel balls inside, whose total weight is 44 grams. The static pre-pull experiment is captured with ordinary camera video, which shows the evolution of the force networks in the granular system when the pulling force on the buried object is gradually increased to the critical point.

After we know the value of the critical pulling force, we use a corresponding weight of water as the pulling force to conduct the pull-out experiment. For the pull-out experiment, we capture this 2-second process with a fast camera, Photron FASTCAM SA5, by taking from 1000 to 7000 images per second. The two-dimensional nature of this pull-out process allows us to visualize and quantify the entire system using high-speed video. We can obtain the trajectory of the intruder by tracking its position at each frame. The photoelasticity of granular quasi-2D disks allows us to quantify the stresses on grains at each frame. Although a two-dimensional experiment is simple in terms of data collecting and processing, it is unclear if the two-dimensional results are similar to three-dimensional systems. So a three-dimensional version of the pull-out experiments with sand and glass bead have also been done by Payman Jalani and Yuchen Zhao in our group.The material discussed in this chapter is primarily the basic techniques used to gather and process the data from videos.

2.1 Experimental Apparatus

The Fig. 2.1 shows the basic schematic for the pull-out experimental apparatus. The intruder is pulled out from the quasi-2D photoelastic particles by the thread connected with a bottle. The initial depth of the intruder, the mass of the bottle and the boundary width of the granular system can be tuned. During the pull-out process, the photoelastic response from the particles above the intruder can be visualized, which indicates the internal stress in those particles.

The photograph (Fig. 2.2) shows the main apparatus used in this experiment.

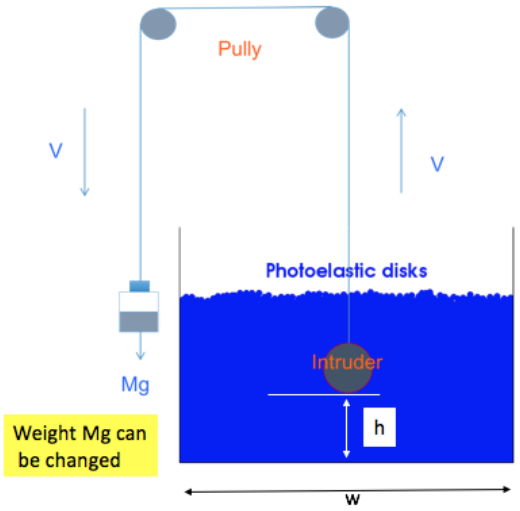

FIGURE 2.1: Schematic of the experimental apparatus for pull-out experiments in quasi-2D granular materials. Photoelastic particles are sandwiched between the two sheets of the glass, and the circular intruder positioned inside the particles can be pulled out from different initial depth(h) by the thread connected to a bottle, whose weight can be changed continuously. The width(w) of the granular system can also be changed with two parallel aluminum bars.

A bidisperse mixture of about 10,000 photoelastic particles (with density about 1.20 g/cm^3, thickness about 0.32 cm, diameters about 0.89 cm and 0.56 cm, masses about 0.24 g and 0.09 g, with similar numbers of each size) are sandwiched between two sheets of transparent annealed glass. The particular photoelastic particles used in the pull-out experiment are made from sheets of polyurethane manufactured by Precision Urethane. The particles have a hardness rating of 60, measured on the Shore Durometer scale, type A, corresponding to an elastic modulus of 1 MPa (Qi et al., 2003; Clark et al., 2015).

No tempered glass can be used in this experiment because the tempered glass has internal stress which produces unexpected fringes under polarized light, which can be seen in our first unsuccessful trial. The distance between the two glass sheets is 0.41 cm so that the particles can move smoothly while loosely constrained by glass sheets. Each annealed glass sheet is 0.95 cm thick, 122 cm wide and 92cm high. The

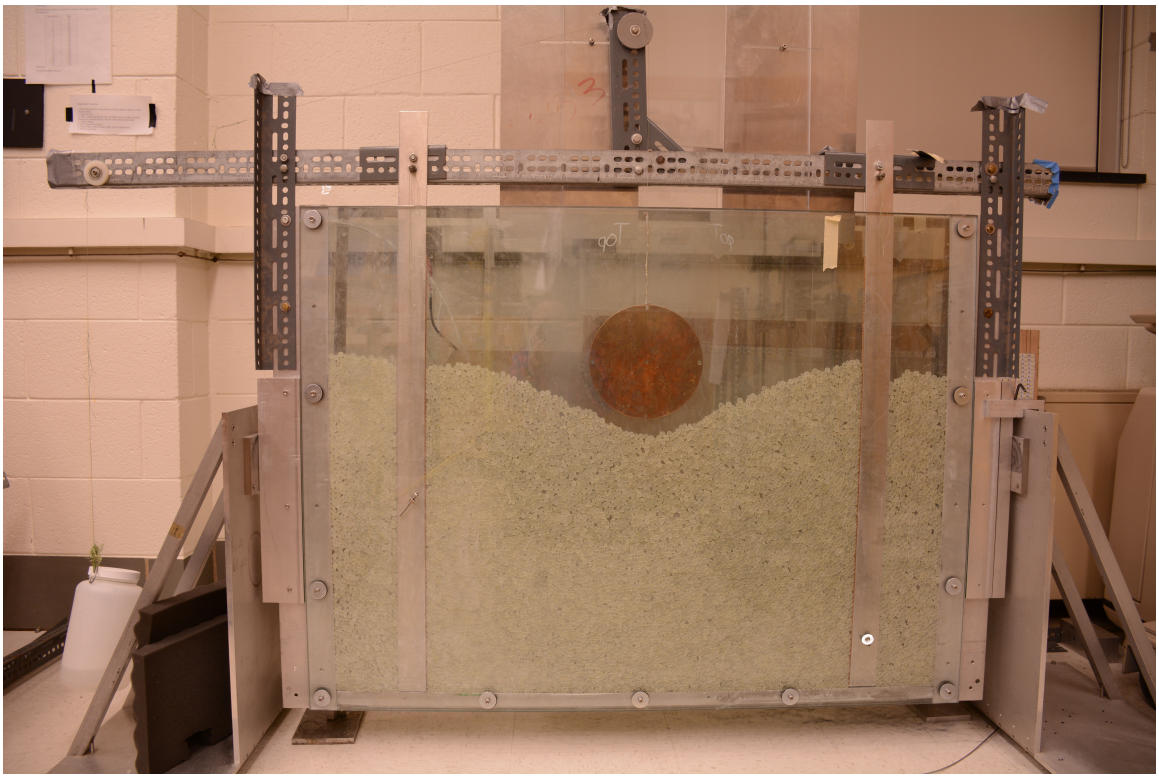

FIGURE 2.2: Picture of the experimental apparatus for pull-out experiments in quasi-2D granular materials. Two pieces of glass plates are fixed to the aluminum frame, photoelastic particles are sandwiched between the two sheets of the glass, while the boundary width of the granular system can be changed with two parallel aluminum bars whose distance can be tuned. The circular intruder positioned inside the particles can be pulled out by the thread connected to a bottle, whose weight can be changed continuously. The thread is made from stiff fish line and constrained in the particles plane by two pulleys on top of the aluminum frame.

granular layers are with depth about 60 cm and with width ranging from 31 cm to 112 cm.

The reason for using bidisperse particles instead of monodisperse particles is to avoid crystallization in this granular system. The small particle diameter is intentionally chosen bigger than the distance between the two glass sheets in order to keep all particles arranged in the same direction, which is quite important for the quasi-2D assumption for the granular system.

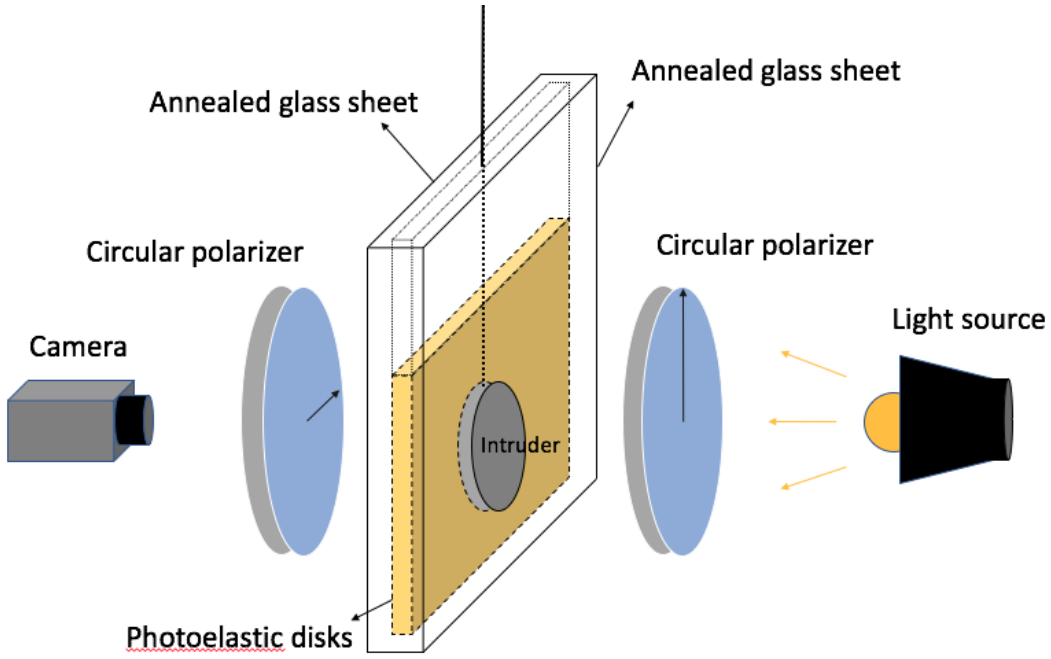

FIGURE 2.3: Cartoon of the experimental apparatus side view for pull-out experiments in quasi-2D granular materials. From left to right subsequently are a camera(fast camera or normal camera), a circular polarizer, an annealed glass sheet, quasi-2D photoelastic granular materials with an intruder embedded, another annealed glass sheet, another circular polarizer, a light source. This arrangement of polarizers and light source provides a way to visualize the internal stress in the granular system while pulling the intruder out. The camera is used to record the pull-out process.

Circular intruders used in the pull-out experiment are machined from bronze sheet (with bulk density of 8.91 g/cm^3, thickness of 2.3 mm) into various sizes, with diameters 20.4 cm, 12.8 cm, 10.0 cm and 6.4 cm (with masses 671 g, 260 g, 166 g and 63 g). They are buried in the granular assembly and are attached to a long thread which connects to the bottle on the other side containing water inside. The thread made from stiff fish line is constrained in one plane by two pulley grooves. The total frictional forces between the thread and pulley grooves are less than 0.5 N.

The recording techniques used in a pull-out experiment are almost the same as in an impact experiment, which also can visualize the force structures inside the

granular system. As is shown in the carton schematic of side view for the pull-out experiments(Fig. 2.3), the natural light comes out from the light source, and goes through a circular polarizer and becomes polarized light and goes through the granular system, then goes through another circular polarizer and is recorded by the camera. These images of the granular system with bright and dark fringes give us the information on the internal stress during the pull-out process.

Light from 62 parallel fixed LED strips (each strip has 63 bulbs) passes through the first circular polarizer, one annealed glass sheet, one layer photoelastic particles, the other annealed glass sheet and the second circular polarizer before it arrives at a camera. The reason for using these LED strips instead of several bright bulbs is that distributed light is more uniform and light source is rectangle with a similar size as the glass sheet in the pull-out experiment.

Pre-pull static experiments are recorded with a normal digital camera, a Nikon D7100. Movies recorded with the Nikon D7100 is taken at 30 frames per second (fps), with a resolution of about 1920×1080 pixels. Images taken with the Nikon D7100 have a resolution of about 6000×4000 pixels.

Dynamical pull-out experiments are recorded with a high-speed camera, Photron FASTCAM SA5, because the whole process of the pull out happens in seconds.

This fast camera has a maximum output of 7000 megapixels per second, which means the maximum frame rate is 7000 frames per second (fps) at the full frame resolution of 1024×1024pixels (or one megapixel). Higher frame rates (up to 775,000 fps) can be achieved by reducing image resolution or the field of view. For dynamical pull-out videos, the camera is typically set at 2500 fps because the light source composed of thousands of small LED bulbs is not bright enough for faster speed, and because otherwise the camera memory is not enough to capture the whole pull-out process.The pixel resolution and the aspect ratio of the videos varies for each experiment depending on the desired field of view.

2.2 Experiment Techniques

Several experimental techniques have been used to extract physical information from the images taken during the pull-out experiments. First, there is an empirical quantity called G-square, which can be used as measure of the internal stress inside the granular material. Second, there is an effective algorithm for position detection of the circular object in images, which tracks the trajectories of the intruder while pulling it out from a granular material. Third, there is an established method called Particle Image Velocimetry (PIV), which yields a macroscopic velocity field in the granular system.

2.2.1 Photoelasticity

Before introducing the G-square method, we need to first understand photoelasticity. Photoelasticity is stress-induced birefringence, exhibited by many transparent materials under polarized light condition. The refractive indices at any point in a photoelastic material depend on the local eigenvalues of the stress tensor. As a result, light polarized along the different principle stress directions have different velocities. Consequently, light polarized along different principle stress directions emerge from the material with phase differences.

On one side of my experiment, the photoelastic system has a light source and a circular polarizer(the polarizer), while on the other side is another circular polarizer (the analyzer)and a camera as in Fig. 2.4. Both circular polarizers consist of a linear polarizer and a quarter-wave plate whose fast axis is at 45 degrees relative to the linear polarizer. The only difference between two circular polarizers is that the linear polarizer in the analyzer is oriented at 90 degrees relative to the linear polarizer in the polarizer. Polarized light coming from the polarizer that does not go through the photoelastic material, e.g. above the particles, will be blocked by the analyzer.

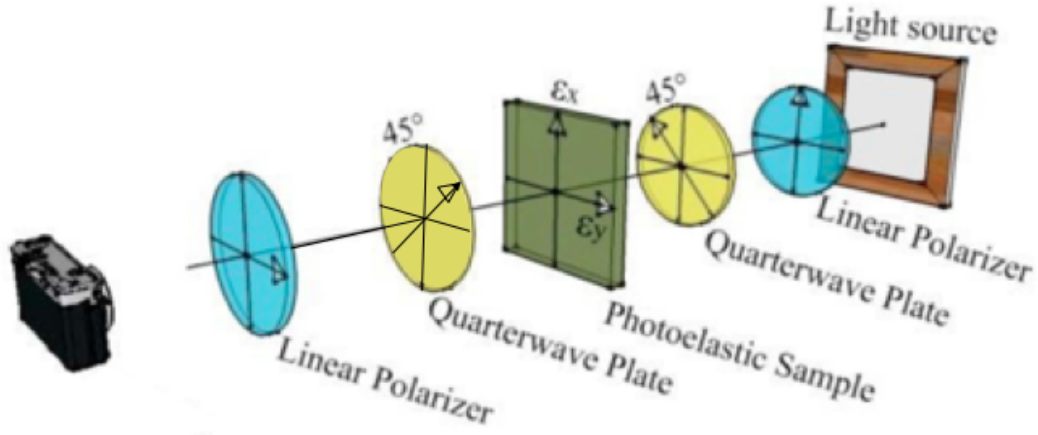

FIGURE 2.4: Graph of the apparatus to produce photoelasticity

The stresses inside the sampled photoelastic material causes the polarized light has a phase retardation, which cause phase shifts, which cause dark and bright fringes. The relation between the stress inside the sample and the light intensity has been shown to follow:

$$I = I_0 \sin^2[(\sigma_2 - \sigma_1)CT/\lambda_l], \tag{2.1}$$

where I is the light intensity coming through the sample, I_0 is the light intensity going into the sample, C is the stress-optic coefficient, T is the thickness of the sample, λ_l is the wavelength of the light source, and σ_1, σ_2 are the two principal stresses.(Majmudar and Behringer, 2005)

The particular photoelastic material used in the pull-out experiment is made from sheets of polyurethane manufactured by Precision Urethane. The particles have a hardness rating of 60, measured on the Shore Durometer scale, type A, corresponding to an elastic modulus of 1 MPa (Qi et al., 2003). This material consists of approximately 12,000 disks with diameter 9 mm and 6 mm, with similar num-

bers of each size.(Clark et al., 2015) Although we have two stiffer particles sets, the pulling-induced internal stress is not big enough for available photoelastic effect.

Roughly, stressed regions in photoelastic images appear bright while stress-free areas appear dark. The photoelastic response needs to be calibrated through a method known as the G-square method, which is basically the gradient of the intensity in pixels, as is shown by the Eq. 2.2:

$$\begin{aligned} G^2(x,y) = \frac{1}{4}\{&[I(x+1,y) - I(x-1,y)]^2 + [I(x,y+1) - I(x,y-1)]^2 \\ &+[I(x+1,y+1) - I(x-1,y-1)]^2/2 \\ &+[I(x+1,y-1) - I(x-1,y+1)]^2/2\}, \end{aligned} \tag{2.2}$$

where I(x,y) is the intensity value of the pixel positioned at (x, y) in a photoelastic image. There is a linear relationship between G^2 and stress in the photoelastic material for moderate stresses, which is quite useful in the analysis of the granular system.

2.2.2 Tracking

To obtain the dynamics of the circular object pulled out from a granular material, we need to know the position of the object at every moment. In order to capture the position of the intruder, we make use of its shape by the Hough Transform (Ballard, 1981). There is a function, imfindcircles, in MATLAB, which uses Circle Hough Transform (CHT) in its algorithm. The input of the imfindcircles function includes an image, radius range (in pixels) of the circle and the sensitivity (from 0 to 1) of the detection.

The CHT is a map from position space{(x, y)} to parameter space {(a, b, r)}, and then picking out the most frequently appeared (a, b, r). Here (x,y) is the position of one pixel point on the edge of circles that need to be detected. Then the returned

(a, b) is the center position coordinate and r is the radius of circle region in the image. All the (x, y) and (a, b, r) should all be in pixels unit. What the map inside CHT does is plotting new circles with centers at (x, y)s and with radius of r, then all theses circles will have many points of intersection. The intersection point of most such circles in the parameter space would be corresponding to the center point of the original circle. In practice, the "supposed-to-be-dark" regions in the granular material allow some small amount of light to pass, which allows the contrast adjusting and intruder's edge sharping possible. The typical error for finding the center of the intruder varies, but is theoretically smaller than a single pixel. The radii of circular intruders are ranging from 3.2cm to 10.2cm and all are about hundreds of pixels in images. All these can be done with the help of MATLAB Image Processing Toolbox.

With the data of the intruder trajectories, we obtain the intruder's velocities and accelerations. Naively, we can calculate the velocity from the displacement by doing the time derivative. The velocity at each frame is calculated as the difference in position between the current frame and the previous, divided by the sampling time. However, this simple method amplifies the experimental noise in the intruder's position, so a low-pass filter must be applied before doing the derivative. Clark et al. use a simple low-pass filter, to calculate the slope of a linear fit of N points of the intruder position versus time, centered at the frame of interest. Velocity data are processed similarly to obtain accelerations. The numbers of data points of acceleration are N points fewer than the velocity data points, and is 2N points fewer than the position data points. Clearly the value of N should be chosen properly. If N is too small, then the experimental error still has a huge effect on the calculation of the velocity and the acceleration. If N is too big, then the physical fluctuations in the dynamics, which will be shown in a later chapter, will be eliminated. Usually, for 2500 fps sample rate, I use $N = 299$ to achieve a balance between eliminating experimental noise and keeping physical fluctuations. This empirical value of N is

different for different sample rates in different experiment runs.

2.2.3 Particle image velocimetry (PIV)

Particle image velocimetry (PIV) is a powerful and widely used tool in fluid mechanics(Tropea et al., 2007) for measuring the full velocity field and is beginning to find application more generally in soft matter physics.

Unlike the techniques for tracking every particle used in some other quasi-2D experiments of our group, I use unpolarized images to do PIV analysis in order to obtain a sense of the average motion of particle groups within the same subregion. The assumption implicit here is that particles in an interrogation area move similarly, and the diffferences between those particles' behaviors can be treated as noise instead of dynamical effects.

Single images can only provide position information, and without time-resolved measurements, PIV analysis is not possible. The canonical PIV method records two images separated by a short time lag, δt. Measurement of the displacement of all image subregions, e.g. every 32×32 pixels window, tells us the approximate velocity field when scaled by δt.(Adrian, 1991) The time lag must be kept small for two reasons: first, the quality of the finite-difference derivatives increases as the time lag between the image decreases; second, the uncertainties due to out-of-region motion of tracers can be minimized.

We would like to calculate a single displacement vector for each subregion of the image. To find the vector, we compute the cross-correlation function:

$$R_{12}(\boldsymbol{x}) = \int W_1(\boldsymbol{x}) I_1(\boldsymbol{x}) W_2(\boldsymbol{x}+\boldsymbol{s}) I_2(\boldsymbol{x}+\boldsymbol{s}) d\boldsymbol{s}, \tag{2.3}$$

where $I_1$and I_2 are the spatially intensities of two images, and W_1 and W_2 are corresponding window functions that specify the subregion in each image. The R_{12} gives a peak if the conditions for the PIV calculation are met. Using Gaussian profile

gives an estimation of the center of the peak, which is the displacement vector for the subregion in the image.(Westerweel, 1997) The accuracy of the PIV method can reach sub-pixel unit.(Cowen and Monismith, 1997)

In the pull-out experiment, the use of PIV can give us a reliable quantitative velocity field when choosing a proper window size and time lag. For the pull-out experiment in a granular system, the velocity measurement tell us directly the evolution of the relative positions of various particle groups. However, at the edge of the intruder and the particles, the velocity field has many errors that are produced by intensity fluctuations, which is reasonable because the homogeneous assumption for PIV is broken near the interface. The software OpenPIV is an open source code for solving PIV problems. The software has a convenient GUI and is generally user-friendly. I have used this PIV package in the data analysis for unpolarized images.

2.3 Experiment Steps

In the pull-out experimental set up, the quasi-2D granular system is arranged in a vertical direction. Then it is very difficult to insert the object into the granular material. So we designed a rotatable glass box, which is helpful when preparing the system. The vertical annealed glass box can be turned around for 90 degrees to a horizontal direction, which makes it much easier for the circular object to be inserted into the granular material.

We prepare the buried intruder in each run by tipping the glass sheets, placing the intruder in a predetermined marked position and letting particles rain back. As a result, the particles are randomly packed. The intruder is pulled by a thread connected to a bottle whose weight can be changed to provide different pulling forces. We have two separate sets of experiments, a static pre-pull experiment and a dynamic pull-out experiment. The static pre-pull experiment finds the minimum force that can break the granular system and pull the intruder out. Then we conduct the

dynamic pull-out experiment with this minimum force to determine the dynamics of the circular object and response of the granular system.

2.3.1 Steps for static pre-pull experiment

In the static pre-pull experiment, we gradually increase the pulling force by repeatedly adding small increments of weight on the bottle side, until the object is pulled out.

The whole process is captured by Nikon D7100 at 30 frames per second (fps). A hand-made flag was waved at front of the object each time right before adding weight, to inform me of the change in pulling force when processing images. The movies taken by the Nikon D7100 are separated into images with `ffmpeg`, an open source software, before image processing. Also, each second in a movie is separated into 30 frames of images.

2.3.2 Steps for dynamic pull-out experiment

In the dynamic pull-out experiment, the minimum pulling force found in static experiment is exerted on the object after we trigger the fast camera to take a video. We use the fast camera to capture this process, which takes only about 2 seconds. The most important thing is to choose the right time to release the bottle, as the video has a limited length because of the storage limitations.

3

Data and analysis for static pre-pull experiment

This chapter will mainly describe the results from static pre-pull experiments. As introduced in the second chapter, these pre-pull experiments are designed to find the minimum pulling force to pull the intruder out and break the granular system. However, more than what we have expected was found in these pre-pull experiments, including the small "jump" of the intruder before the final failure, the change in the force structure when adding pulling force step by step, and the minimum pull-out force's dependance on frictional boundary widths but not frictionless boundary widths.

3.1 Intruder motion

The pre-pull experiments are conducted with the intruder still inside the granular material. At the end of each such experiment, the intruder is finally pulled out. In this section, the movement of the intruder before being pulled out will be investigated.

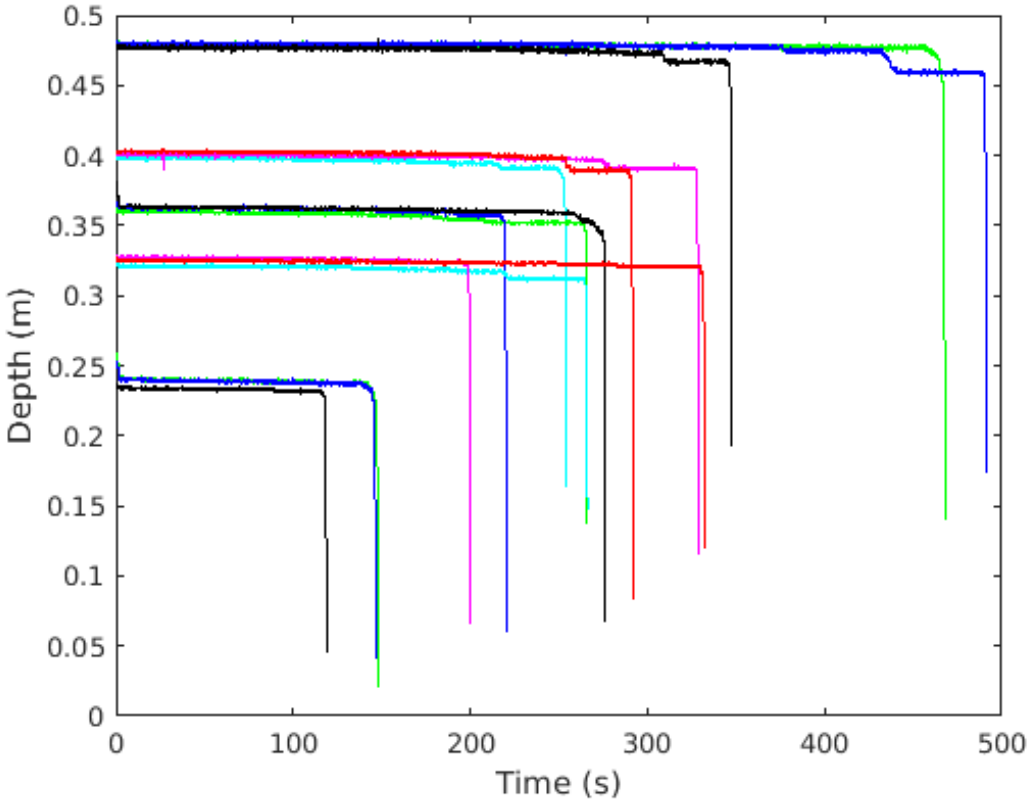

FIGURE 3.1: Depth of intruder vs. time. For each initial depth we have three runs. The experiment is done with the width=75.5 cm frictional boundary. During the experiment, the weights (each with mass of 44g) are added step by step until the intruder goes out. For the initial depth from deep to shallow, the weights are totally added 14±1 times, 12±1 times, 10±1 times, 9±1 times, 5 times.

During the experiment, we add a given amount (about 0.44N) of pulling force on the intruder at each step. Although the total pulling force is not big enough to break the granular system and pull the intruder out, the intruder still exhibits some small motion each time after the addition of an incremental (0.44N) pulling force. As shown in Fig. 3.1, the depth of the intruder remained almost unchanged, after each increment of pulling force. This continued until at certain times the intruder had a small jump, just after I added 0.44N of pulling force. The displacement of the intruder was very small at first, but when the pulling force was close to the

critical failure force, the displacement of the intruder became much larger with each additional weight. Although these displacements of the intruder cannot be ignored, the intruder still remains inside the granular system. Necessarily, at each step, some small stick-slips happened in the pre-failure process, with reorganization of particles above the intruder during stick-slips. The structural response of the granular system under an increasing pulling force will be shown in the next section.

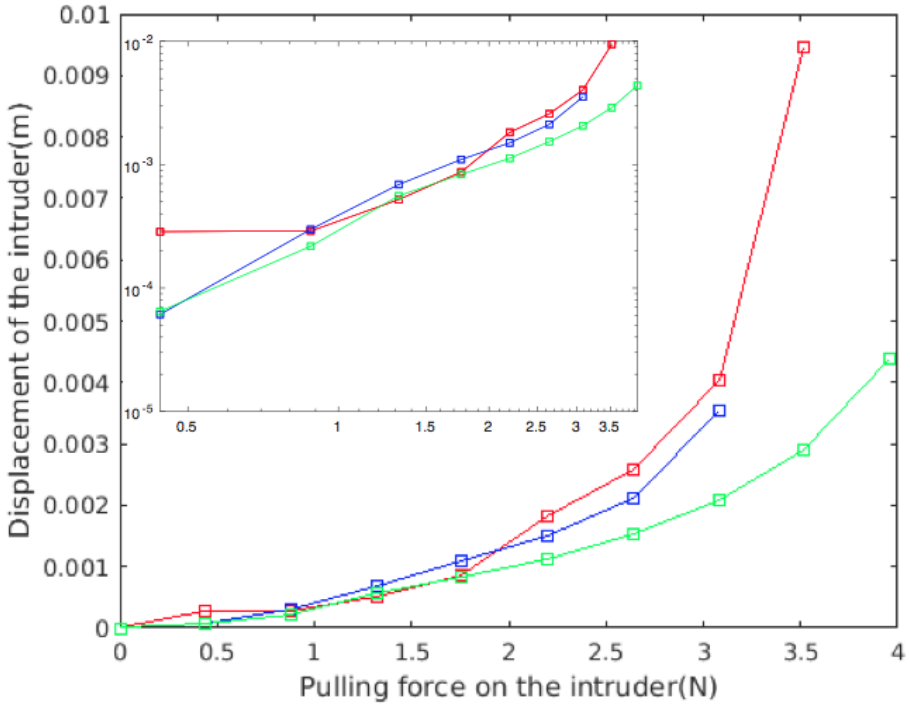

FIGURE 3.2: Displacement of intruder vs. pulling force on the intruder. The experiment is done with width=75.5 cm frictional boundaries and with the intruder's initial depth set to 31.8cm. The intruder has a radius of 10.2 cm. Different colors represent different independent runs. The intruder was pulled out after adding another 0.44N to the pulling force of the last data point, which ends each curve. In the upper left small figure, the displacement and the pulling force are plotted in log-log scale indicating a power law.

Fig. 3.2 shows the details for displacements of the intruder after adding increments of pulling force of 0.44N. In this example, the intruder is initially positioned

at a depth of about 31.8 cm in a granular system with frictional boundary of width 75.5cm; the initial weight of the bottle is the same as the weight of intruder. Then at each step we add 44 grams to the bottle side, which provides an extra pulling force. In Fig. 3.2, we see that bigger displacements of the intruder happen near the critical failure force. The intruder was pulled out after adding the last increment of 0.44N to the pulling force after the last data point. The intruder displacement vs. extra pulling force obeys a power law: $D(F_{pulling}) = 4.31 * 10^{-4} * (F_{pulling})^{1.61}$. The statistical error for the exponent 1.61 is 0.21.Here, the intruder displacement is in units of meters and the pulling force is in units of newtons.

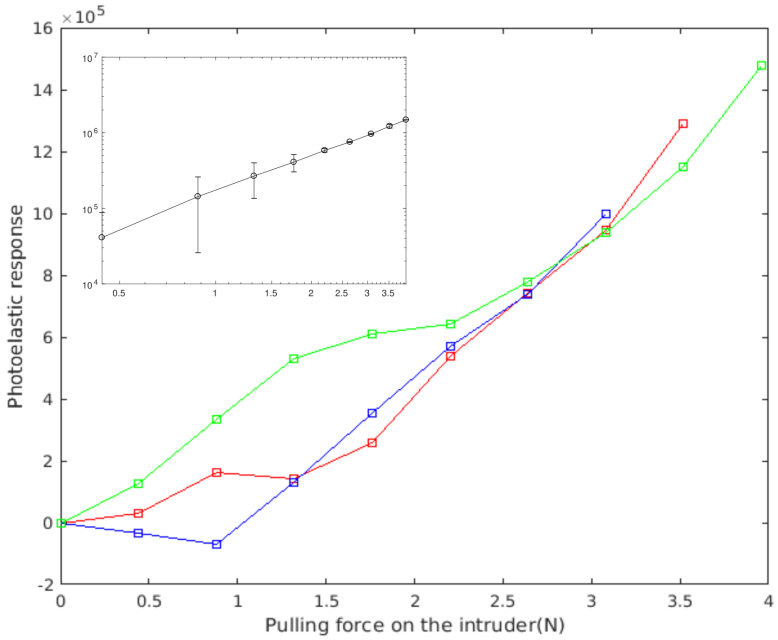

FIGURE 3.3: Intensity from photoelastic image vs. pulling force on the intruder. The experiment is done with width=75.5 cm frictional boundaries and with the intruder's initial depth set to 31.8cm. The intruder has radius 10.2 cm. Different colors represent different independent runs. The intruder was pulled out after adding another 0.44N to the pulling force of the last data point, which ends each curve. In the upper left small figure, the averaged intensity and the pulling force are plotted on log-log scales suggesting a power law.

Similarly, the stress response (photoelastic response in images) in the granular material vs. extra pulling force on the intruder roughly obeys a power law: $Intensity(F_{pulling}) = 1.72 * 10^5 * (F_{pulling})^{1.71}$, as shown in Fig. 3.3. The statistical error for the exponent 1.71 is 0.33. The photoelastic response is calculated by adding up the total intensity of each pixel in the image after removing the very first image when the extra pulling force is zero. Here, the intensity has arbitrary units and the pulling force is in units of newtons. These two results above is reminiscent of the Ramberg-Osgood equation, which describes a power law relation between strain and stress for strain hardening of solid materials around a yield point. The power law is also found in the uniaxial compression of the granular materials.

Additionally, we find that the final displacement of the intruder before the system failure, depends on the initial depth of the intruder. The final displacement of the intruder is defined as the distance between the initial position and the final position before the intruder is pulled all the way out. As shown by Fig. 3.4, the final displacement increases with initial depth linearly, which is fitted to a straight line with the slope 0.035 ± 0.014 and the intercept (-0.00487 ± 0.00497)m. In Fig. 3.4, the frictional boundary width is 75.5 cm. The increase of the intruder's final displacement is monotonous for this wide boundary. Error bars in Fig. 3.4 are standard errors calculated from standard deviation for 3 independent runs. The standard error of the final displacement, as shown in Fig. 3.4, increases with the initial depth, i. e. as the initial depth of intruder increases, the final displacement of intruder varies more for several independent repeat runs.

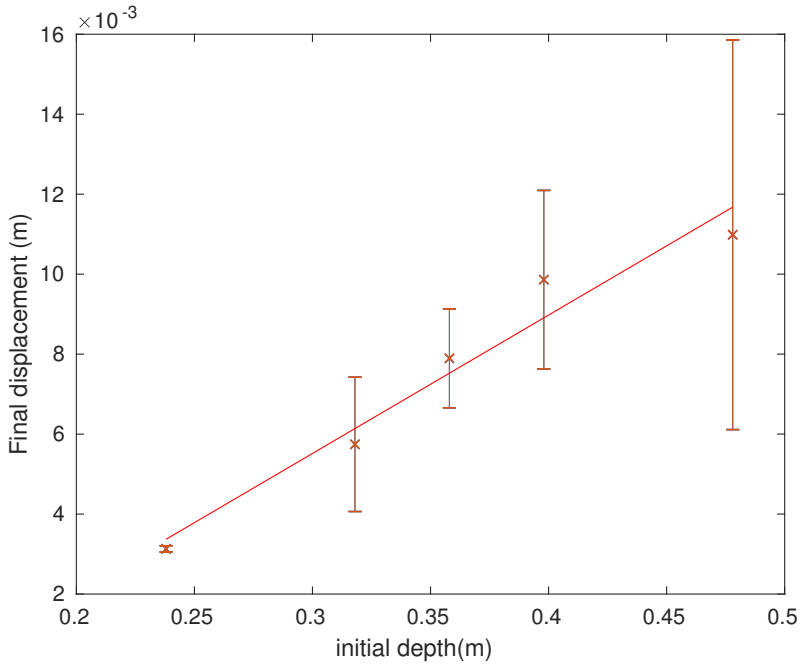

FIGURE 3.4: Final displacement of intruder vs. intruder's initial depth. The intruder moves the final displacement accumulatively at the last step before the system fails during the pre-failure experiments. The experiments are done with width=75.5 cm frictional boundary and with various initial depths of the intruder. The intruder has radius 10.2 cm. Bars are standard errors calculated from standard deviation for several independent repeated runs. Red line represents the linear fit with the slope 0.035±0.014 and the intercept (-0.00487±0.00497)m.

However, if we decrease the boundary width, the situation is different. As shown in Fig. 3.5, a monotonous increase of the final displacement is no longer valid for cases with boundaries of width=34.5cm and 38cm. For smaller widths, the boundary plays an important role in keeping the intruder inside the granular system. Error bars in Fig. 3.5 are standard errors calculated from the standard deviations for several independent runs.

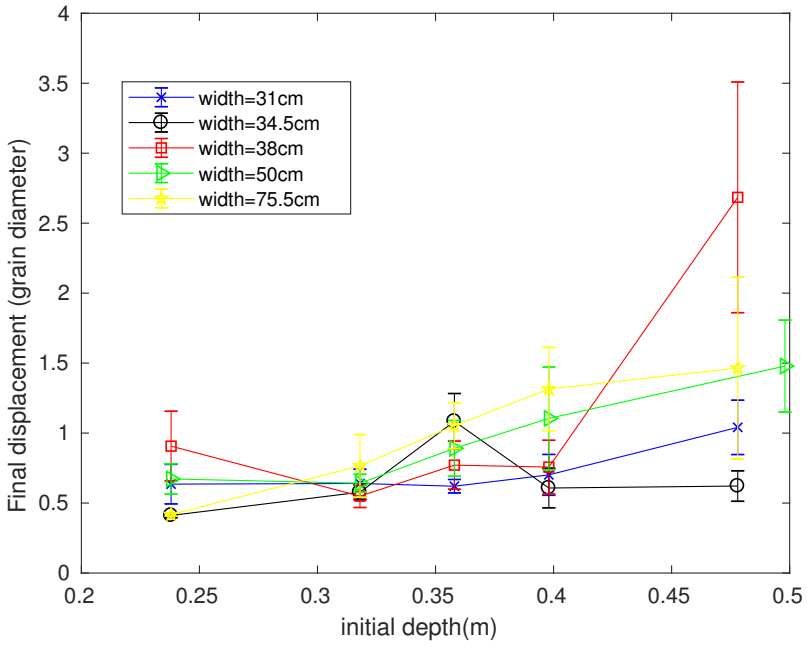

FIGURE 3.5: Final displacement of intruder vs. intruder's initial depth for various boundary widths. The experiments are done with width=31, 34.5, 38, 50, 75.5 cm frictional boundaries, represented with different colors. Intruder is with radius 10.2 cm. Error bars are standard errors calculated from standard deviation for several independent repeat runs.

To better understand the different behavior of the intruder for various boundary widths, we can compare the stress response of grains above the intruder when the initial depth of intruder is 47.8 cm, as shown in Fig. 3.6. For the images with boundary widths less than 75.5cm, the force networks are much denser and the force networks connect to the boundary with an angle less than 90°. Both the stronger force networks and the smaller angles formed between the force networks and the frictional boundaries, result in those distinguishable behaviors of the intruder.

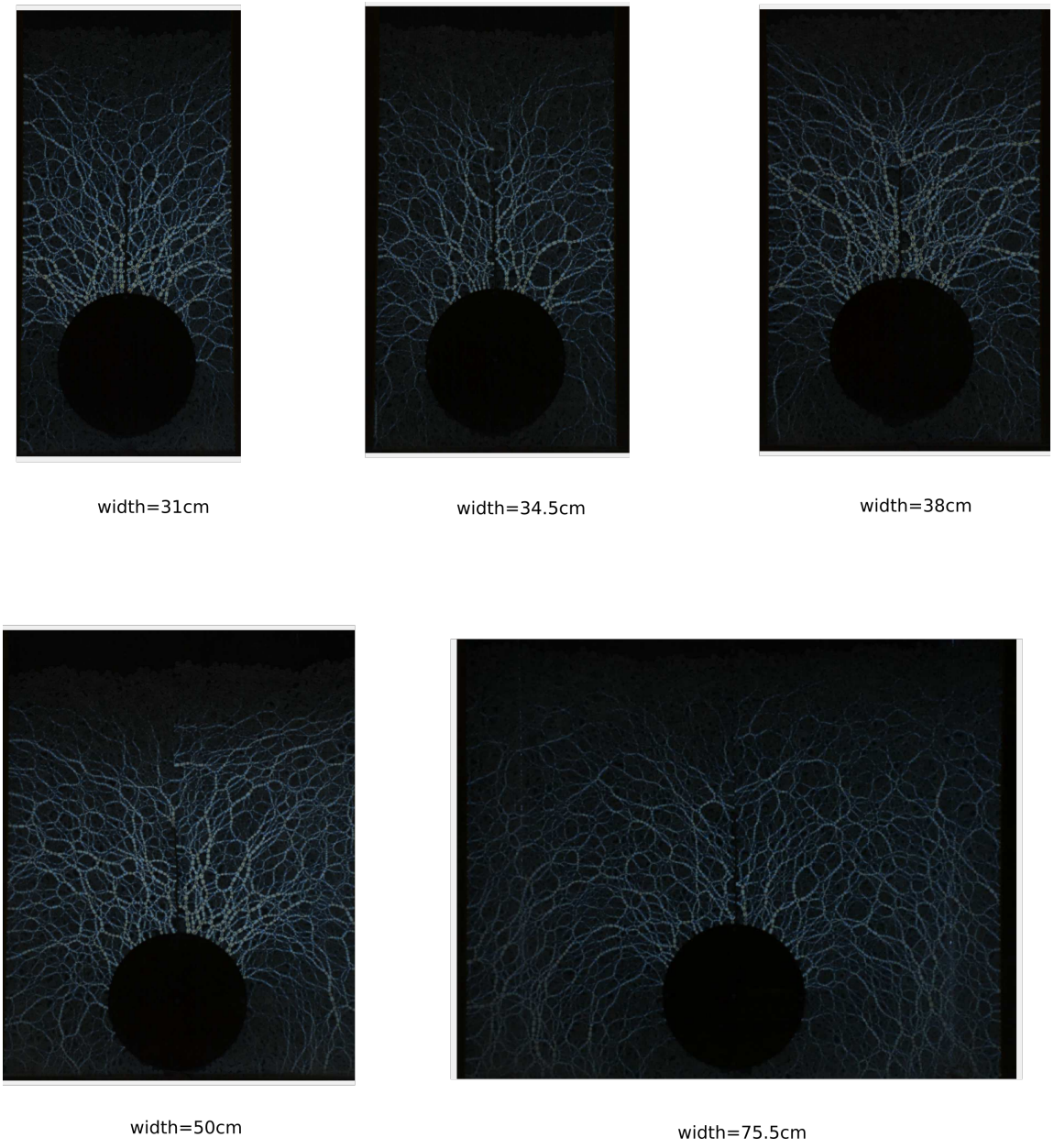

FIGURE 3.6: Final photoelastic image before failure for various boundary widths. The experiments are done with width=31, 34.5, 38, 50, 75.5 cm frictional boundaries. Intruder is with radius 10.2 cm and with initial depth about 47.8 cm.

Both the trend of the final displacement vs. initial depth and the minimum breaking force's relation with initial depth show complex behavior.

3.2 Minimum breaking force

Here, the minimum breaking force is defined as the difference between the smallest pulling force that is essential to pull the intruder out of the granular system and the weight of the intruder. In this section, we will discuss related factors that affect the minimum breaking force, e. g. the initial depth of the buried intruder, the friction of the granular system's boundary, and the width of the granular system's boundary. The circular intruder used in this section has a radius of 10.2 cm, and a weight of 671 grams.

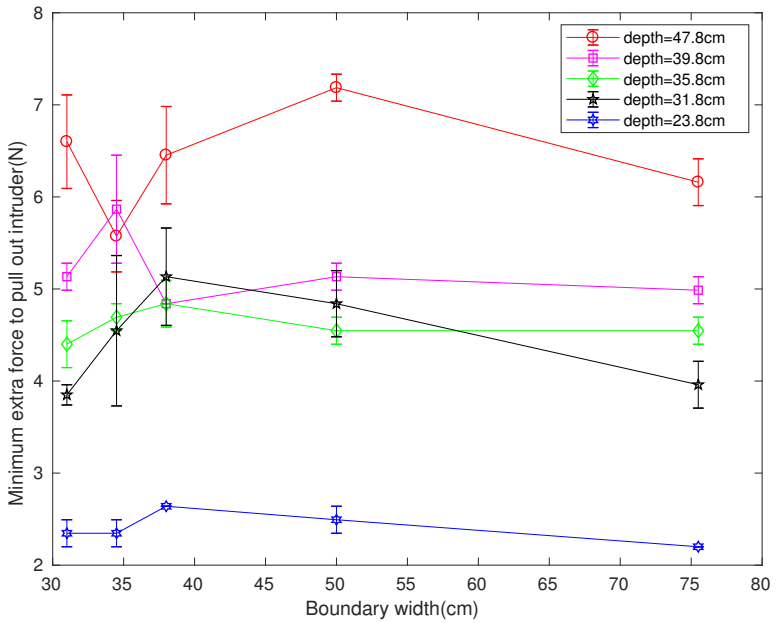

FIGURE 3.7: Minimum breaking force vs. frictional boundary's width. Different colors represent different initial depths of the intruder. For each initial depth, the minimum breaking force fluctuates with frictional boundary widths.

Fig. 3.7 shows that the minimum pulling force to break the granular system depends not only on the buried depth of the intruder, but also depends on the frictional boundary width of the granular system. When the granular system has a

boundary width of 31cm and 75.5cm, with intruder radius 10.2cm, the breaking force monotonously increases with initial depth of the intruder. However, for boundary width of 34.5cm, 38cm and 50cm, the breaking force is even bigger for some shallower cases.

Surprisingly, for frictional boundaries with width 38 cm and 50 cm, when the intruder's initial depth increases from 31.8 cm to 39.8 cm, the increase in minimum breaking force with initial depth is much smaller than the cases when intruder's initial depth increases from 23.8 cm to 31.8 cm and from 39.8 cm to 47.8 cm, although these three comparisons have the same initial depth's increase, which is 8 cm.

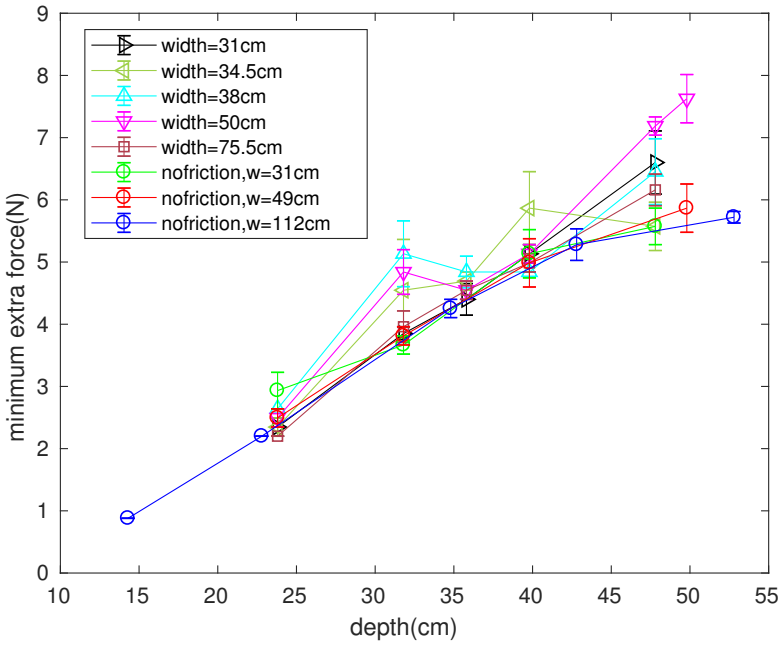

FIGURE 3.8: Minimum breaking force vs. intruder's initial buried depth. Triangle or square symbols represent frictional boundaries, while different colors represent different boundary widths. The circle symbol represent the frictionless boundaries, while different colors also represent different boundary widths. For frictionless boundaries, the minimum breaking force smoothly increases with the initial depth of the intruder. For frictional boundaries with widths of 31cm and 75.5cm, the minimum breaking force also smoothly increases with the initial depth of the intruder, while for other three frictional boundaries with widths of 34.5cm, 38cm and 50cm, some fluctuations appear in the minimum breaking force vs. initial depth relation.

The bump found in the case of frictional boundaries with width= 38cm and 50cm at intruder's initial depth=31.8cm, as shown in Fig. 3.8, indicates there is an unusual "force structure" formed in the granular system. This structure presumably does not form for smooth boundaries (e. g. nofriction, w=49cm). That "structure" does not seem to form with too narrow frictional boundaries (width=31cm) or too wide frictional boundaries (width=75.5cm), because the bumps are absent in data with frictional boundaries of widths 31cm or 75.5cm. The "structure" is the force arch located in the 25° region, which will be described in the next section.

Additionally, if the initial depth of the intruder is deep enough, the differences in the curves in Fig. 3.8 between frictional and smooth boundaries is quite clear. All the experiment runs with the smooth boundaries of various widths have almost the same minimum breaking force even at the deepest data point, while the runs in frictional boundaries with different widths show minimum breaking forces that are all bigger than the smooth case.

3.3 Photoelastic response and explanation for "bump"

In this subsection, we consider the photoelastic response to increments of weight. As shown in Fig.3.9, the force chains above the intruder build up step by step, forming a fan shape in the granular system. If we change the boundary width of the granular system from 75.5cm to 31cm, we obtain the images in Fig. 3.10, showing that the force chains grow until they touch the boundary, spreading throughout the whole granular system. One of most interesting things we want to get from the photoelastic images is an explanation for different critical pulling forces for different boundaries and widths.

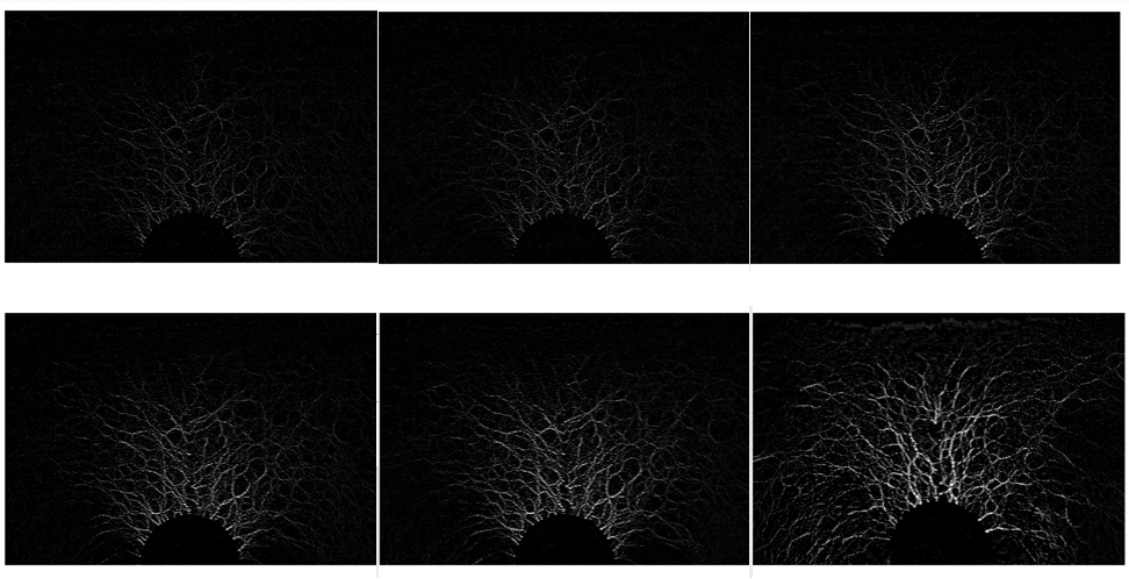

FIGURE 3.9: The build-up process of force structures in the 2D granular system while incrementally increasing the pulling force on the intruder during the pre-failure experiments with frictional boundary width of 75.5cm and intruder initial depth of 47.8cm. The six selected images show the typical change in the granular system while increasing the pulling force acting on the intruder(radius of 10.2 cm).

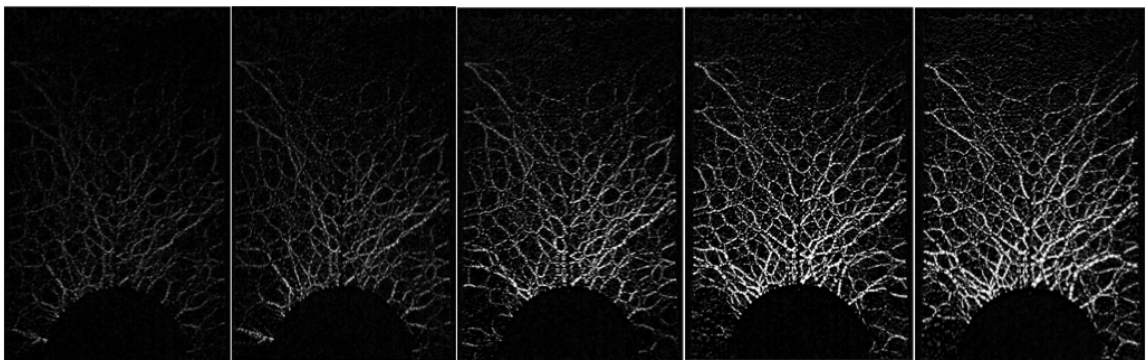

FIGURE 3.10: The build-up process of force structures in the granular system while incrementally increasing the pulling force on the intruder during the pre-failure experiments with frictional boundary width of 31cm and intruder initial depth of 47.8cm. From left to right, the five selected images show the typical change in the granular system while increasing the pulling force acting on the intruder(radius of 10.2 cm).

One possibility is that the boundary width changes the angular preference of gran-

ular response, which will determine how much force from the intruder the boundary friction can bear. As shown in Fig. 3.11, we calculate the average intensity in each angular region above the intruder. We cut the left 15.5cm region in photoelastic image above the intruder into 9 regions (each region with 10 degree angular span). For each run, we choose the last few images which correspond to the maximum pulling force the system can bear. Keeping only the middle 31cm part, we divide the left half into 9 angular regions. (For images of granular system with boundaries wider than 31cm, we only keep the corresponding middle 31cm part.)

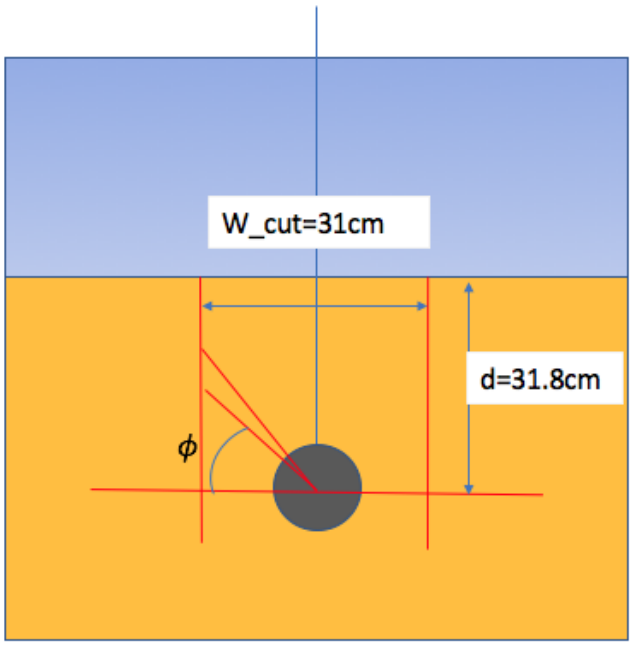

FIGURE 3.11: Graph for calculating the angular response of granular system. For each run, we choose the last few images, which correspond to the maximum pulling force the system can bear. Then we keep the middle 31cm region and divide the left 15.5cm part into 9 angular regions, which means the ϕ is 0, 10, 20, 30, 40, 50, 60, 70 and 80 degrees in this analysis.

The results in Fig.3.12 show that the maximum photoelastic response in an angular region for the width=34.5cm, 38 cm and 50cm cases are at $\phi = 25^{\circ}$, while for

width=31cm and 75.5cm, the maxima are both at $\phi = 45°$. The friction coefficient of the boundary is around 0.6, which means that a larger force coming from a direction of $25°$ can be more readily balanced than a force coming from direction of $45°$. This suggests a reason for the bump found at initial depth 31.8cm for widths of 34.5cm, 38cm and 50cm in the Fig. 3.8.

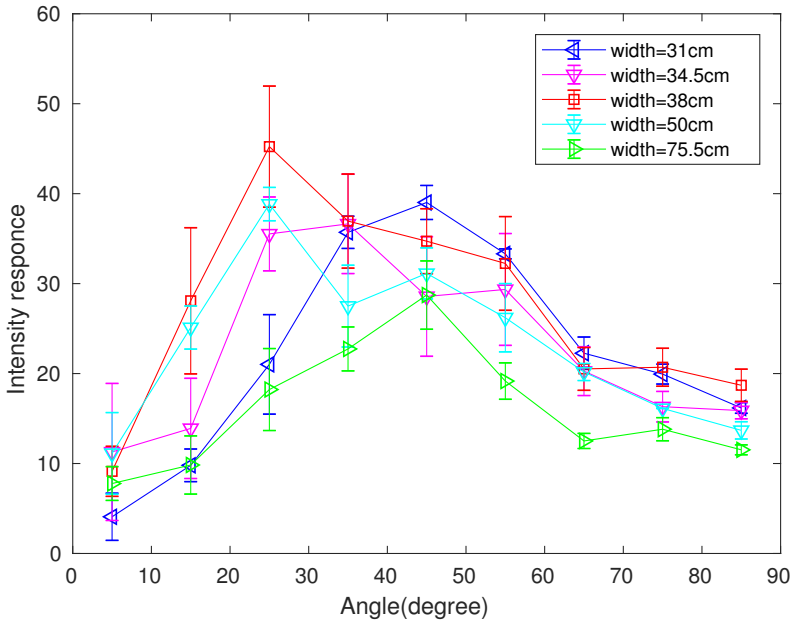

FIGURE 3.12: Graph for angular photoelastic response: Intensity vs. angle. Different colors represent different boundary widths. All the boundaries are with friction. The initial depth of intruder is 31.8cm. For the boundaries with widths of 31cm and 75.5cm, the maximum intensity response (stress) appears in the $45°$ region. However, for the boundaries with widths of 34.5cm, 38cm and 50cm, the maximum intensity response (stress) comes in the $25°$ region.

Now, we need to know why the difference occurs. What is inside the $25°$ region around the intruder at an initial depth of 31.8cm when the boundary width is 34.5cm, 38cm or 50cm? The simple way is to check the original photoelastic image, as shown in Fig. 3.13. The arch near the $25°$ and $155°$ regions provide the strong resistance to the upward loading of the intruder. To form a stable arch, the length of the arch

should be proper and the other side of the arch has to be fixed by the frictional boundary.

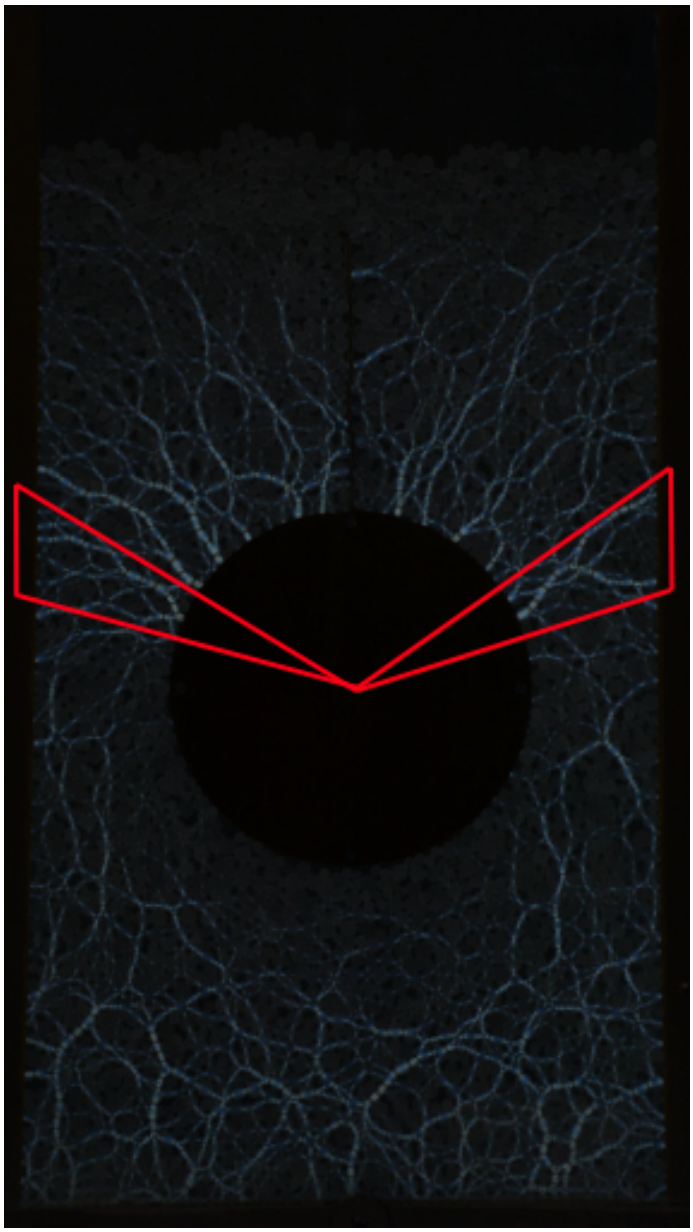

FIGURE 3.13: Arches (formed with bright force chains) inside the 25° and 155° regions (marked by red triangle) of the photoelastic image. The force chain arches formed between the intruder and the two vertical boundaries result in the increase of the maximum pulling force the granular system can bear. The initial depth of intruder is 31.8cm. The boundary width is 34.5cm.

4

Data and analysis for dynamic pull-out experiment

This chapter will mainly present experimental data and analysis for the dynamic pull-out experiments. There are at least three questions to be asked about this experiment:

- What is the dynamics of the circular intruder in this pull-out process?
- How does the granular system respond during the pull-out process?
- What is the relationship between the intruder dynamics and the granular particle response?

Additionally, several parameters can be tuned to check their effects on the pull-out process, e. g. the radius of intruder, the depth of the intruder's initial buried position and the width of the boundary for the granular system among others.

I will discuss the corresponding results in the following sections.

4.1 Intruder's size effect

After the static pre-pull experiment, we know the minimum force that is needed to pull the intruder out of the granular material. Now we conduct dynamic pull-out experiments with the smallest pulling force to achieve failure. High speed video visualizes the fast pull-out process once the intruder begins to move. At first, the intruder is stuck, but then it accelerates and escapes quickly from the bed.

We track the intruder to obtain the relation between intruder's position and time, as shown in Fig. 4.1. The intruder used here has a radius of 6.4cm and the net pulling force is 3.41N after eliminating the intruder weight of 260g. Several runs are repeated with different initial configurations of photoelastic particles, but all the curves of position-time relation collapse together. The t=0s point is chosen when intruder's velocity equals 0.15m/s, in order to collapse different runs with various initial imaging times.

After we get the position-time relation, we can obtain velocity vs. time curves, as shown in Fig. 4.2. For the dynamic pull-out experiment, a fast camera taking images with a speed of 1000fps is used to capture the dynamic pull-out process which lasts about 1 second.

As is shown in Fig. 4.2, the main part of the v vs. t curves can be fitted with exponential functions $v = \boldsymbol{a} * \exp(\boldsymbol{b}t) + (0.15 - \boldsymbol{a})$, indicating a linear relationship between velocity and acceleration as in Fig. 4.3. Here the t=0 point is chosen when the velocity equals 0.15m/s.

The slope in Fig. 4.3 is the reciprocal of $\boldsymbol{b}$ in the exponential fitting function of the velocity. Loops can be found in Fig. 4.3, because the grains reorganize during the process, creating renewed resistance to the intruder. During that time, the acceleration drops significantly. This is related to stick-slip processes, which will be shown in detail later. Intruders of radius 3.2cm, 6.4cm and 10.2cm have been used

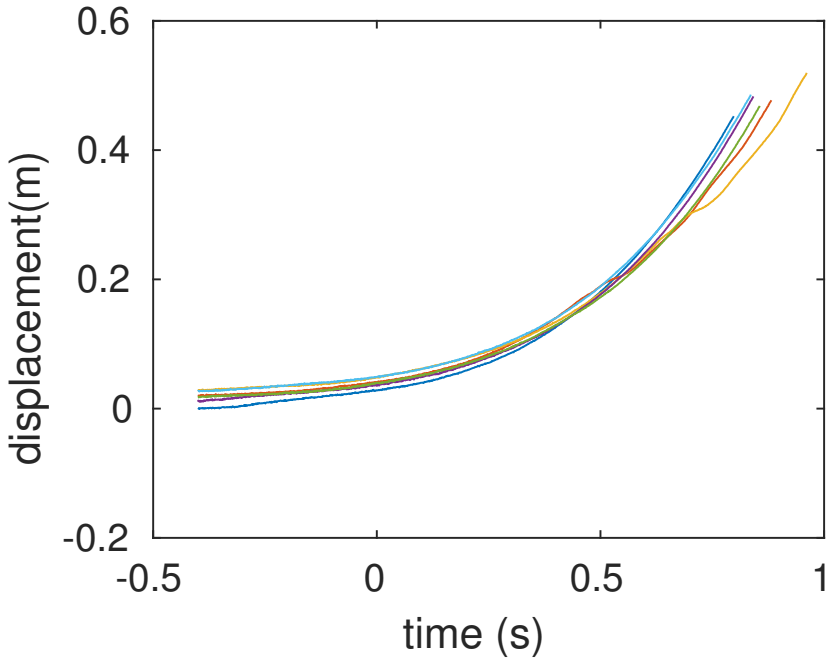

FIGURE 4.1: The graph of R=6.4cm intruder's displacement vs. time. Different colors stand for different runs with the same circular intruder R=6.4cm. The time zero point (t=0s) is chosen when intruder's velocity equals 0.15m/s.

in the experiments. After repeating the pull-out experiment with different circular intruders from the same initial position, we find $\boldsymbol{b}$, the reciprocal of the slope in the velocity vs. acceleration graph, which decreases as the radius increases, as shown in 4.4. This means it takes a longer time for a bigger intruder to be pulled out with the critical pulling force. The resistance faced by a bigger intruder is relatively larger than a smaller intruder during the pull-out process. However, parameters $\boldsymbol{a}$ in the fitting function of velocity are independent of the intruder radius.

In order to understand what is happening inside the granular system, we also extract the force chains (bright parts) from high speed photoelastic images, as shown in Fig. 4.5.

Force chains are components of the granular system that are under a pressure bigger than some threshold, as visualized by photoelasticity. We have chosen a

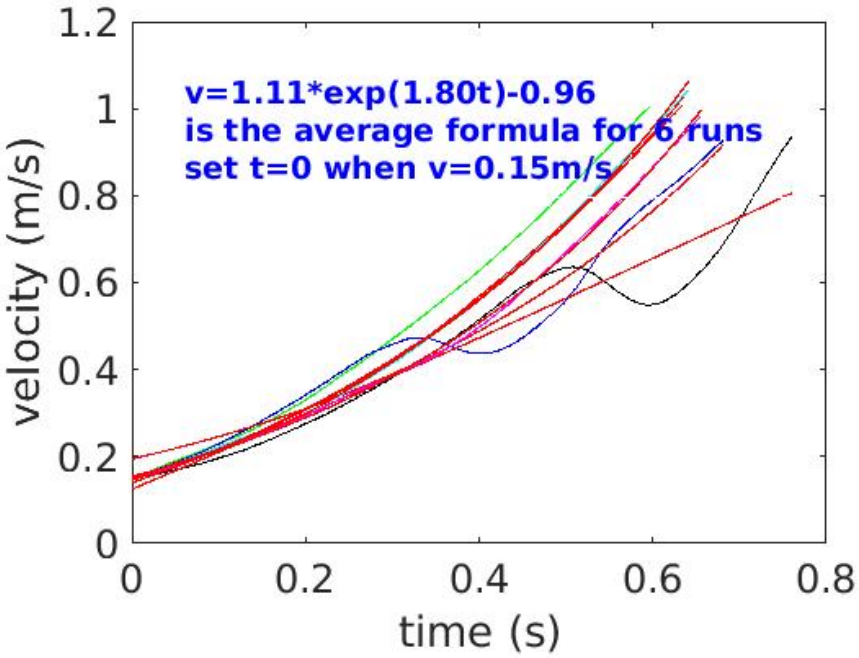

FIGURE 4.2: The graph of R=6.4cm intruder's velocity vs. time. Different colors stand for different runs with the same circular intruder with radius R=6.4cm. Wiggles for some runs are a result of stick-slip processes. The velocity-time curves can be fitted on average with an exponential function: $v = 1.11 * exp(1.80t) - 0.96$.

particular threshold which helps with converting grey images to black and white images that highlight the force chains as white components. The Matlab function ***graythresh*** is used in choosing the threshold using Otsu's method(Otsu, 1979), which searches for the threshold that minimizes the intra-class variance of intensity. If I manually tune the threshold to a value that is not too far away from this threshold, the force chains do not change much. Because the force chains are connected with each other forming a network with hot spots, I separated single chains by cutting at the "hot spot", where multiple chains meet. Then I can pick out each single chain and calculate a geometric quantity, namely the curvature. The curvature is defined here as the reciprocal of the radius for the circle fitted best into the single force chain.

Then I calculate each force chain's curvature, and obtain the distribution of curvatures. The force chain curvature distributions in the first and last half of the

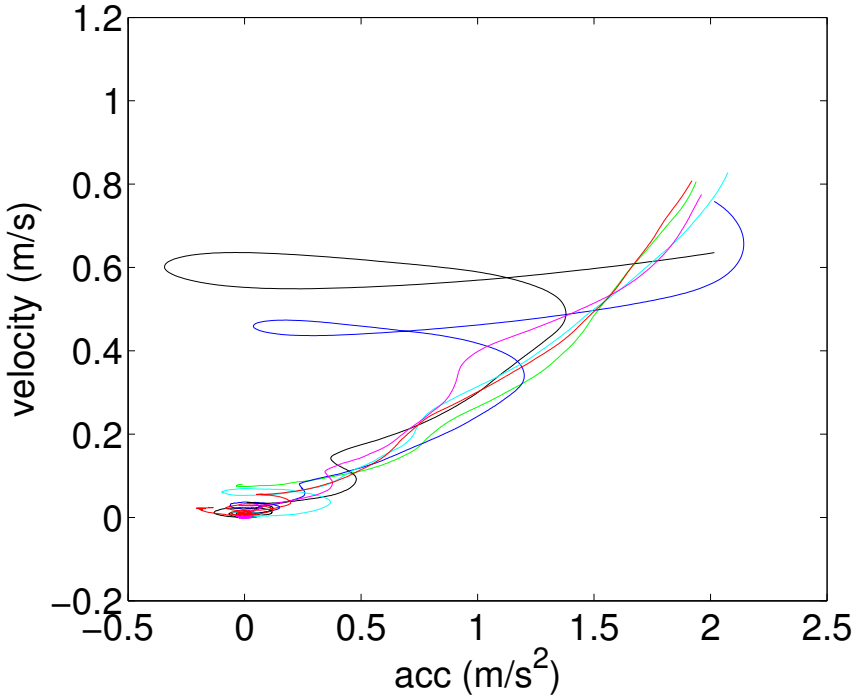

FIGURE 4.3: The graph of velocity vs. acceleration for intruder with radius R=6.4cm. Different colors stand for different runs with the same intruder. The velocity increases linearly with acceleration except that loops are found in some runs as a result of stick-slip processes.

runs follow the same distribution for different intruder sizes, as shown in Fig. 4.6. Separating a complete run into two different parts is intended to show that the curvature distribution in the force network of granular particles is independent of time, once the intruder starts to move. Different colors stand for different intruder sizes, while triangle "$\bigtriangledown$" and square "$\square$" represent first and last half run, respectively. The y-axis is the normalized frequency (calculated by dividing the total number of force chains) and the x-axis is the curvature. After normalization, the distributions can be collapsed into a single fitting function: $y = s_1 * \exp(-s_2 * |log(x) - s_3|^{s_4})$, where $s_1 = 0.033 \pm 0.002, s_2 = 1.49 \pm 0.06, s_3 = 2.88 \pm 0.02$ *and* $s_4 = 1.66 \pm 0.09$.Before this self-defined fitting, I have fitted the curvature distribution with Weibull distribution: $y = \frac{k}{\lambda}(\frac{x}{\lambda})^{(k-1)} * exp(-(\frac{x}{\lambda})^k)$, where k=1.97$\pm$0.05 and λ=29.88$\pm$0.77. However, the

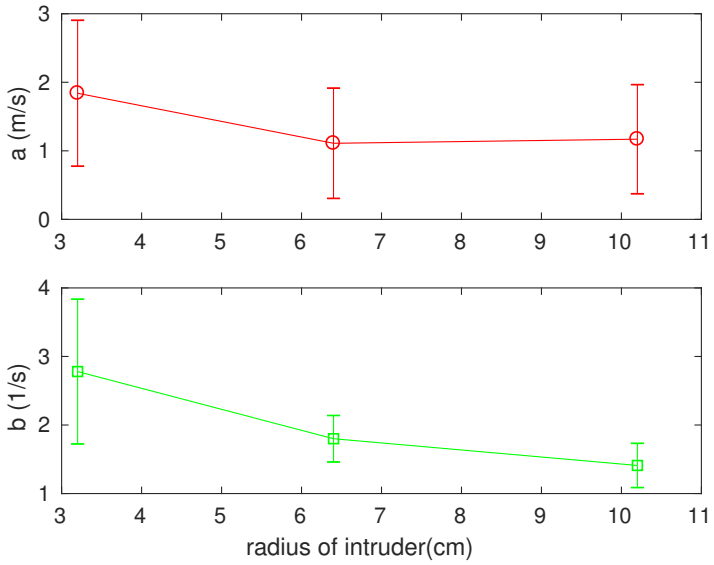

FIGURE 4.4: Fitting parameters ($\boldsymbol{a}$ and $\boldsymbol{b}$) in velocity-time relation vs. radius of intruder. Intruders of radius 3.2cm, 6.4cm and 10.2cm were used starting from the same initial position. The velocity vs. time relations are fitted with the same exponential form,$v = \boldsymbol{a} * \exp(\boldsymbol{b}t) + 0.15 - \boldsymbol{a}$, except that values of fitting parameters vary. The fitting parameter $\boldsymbol{b}$ decreases with intruder radius, while the parameter $\boldsymbol{a}$ does not decrease monotonously with intruder size, and may be constant within the error bars.

problem is that the peak value in the data is much higher than the peak value calculated from the Weibull fitting function.

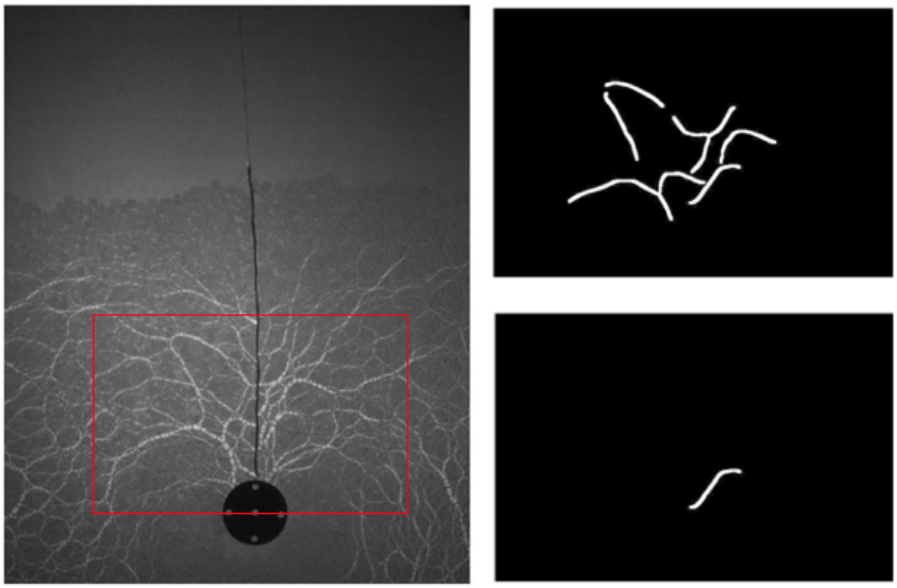

FIGURE 4.5: Extraction of single force chain: the left image is an original image from the dynamic pull-out experiments, the upper right image shows the force chains in a chosen box area above the intruder, and the lower right image shows one of those force chains in that box area.(Zhang and Behringer, 2017)

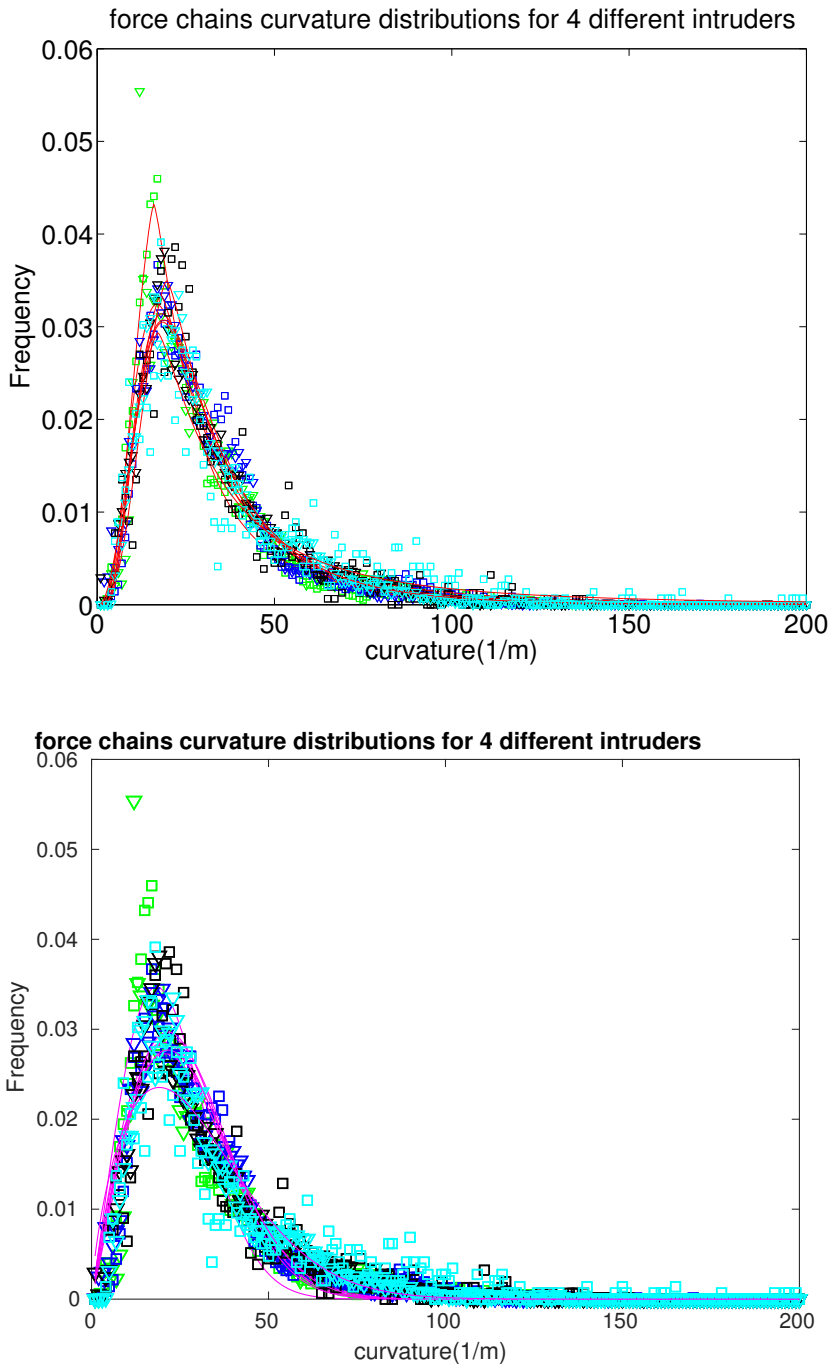

FIGURE 4.6: Force chains curvature distribution for 4 different circular intruders, with radii of 3.2cm, 5.0cm, 6.4cm and 10.2cm. Different colors stand for different intruder sizes, while triangle "▽" and square "□" represent first and last half run, respectively. In the upper part, the curvature distribution is fitted with a self-defined function(red line): $y = s_1 * \exp(-s_2 * |log(x) - s_3|^{s_4})$, where $s_1 = 0.033 \pm 0.002, s_2 = 1.49 \pm 0.06, s_3 = 2.88 \pm 0.02$ *and* $s_4 = 1.66 \pm 0.09$. In the lower part, the curvature distribution is fitted with the Weibull distribution(magenta line): $y = \frac{k}{\lambda}(\frac{x}{\lambda})^{(k-1)} * exp(-(\frac{x}{\lambda})^k)$, where k=1.97±0.05 and λ=29.88±0.77 .

4.2 PIV field for particle flow

As discussed in experimental techniques, particle image velocimetry (PIV) is a powerful tool for measuring the full velocity field, that I have applied to the dynamic pull-out experiments. In this procedure, unpolarized images are taken at frame rates around 5000fps with the fast camera. The software OpenPIV is used for image analysis, and the window size is chosen as $32pixels \times 32pixels$ for the convolution calculation. (On average, there are about 9 particles in one window.) As shown in left Fig. 4.7, the red arrows represent the average velocity of particles in a small window. The direction of each arrow represents the local flow direction, the length of the arrow represents the relative local magnitude. The granular system acts somewhat like a fluid flow around a cylinder during pull-out. Specifically, the particle flow field looks like a magnetic doublet field superposed on a constant field, which starts from the top of the intruder, and bends and goes back to the other side of the intruder. However, a hole without granular particles inside is formed below the intruder, which is quite different from the fluid flow around an infinite cylinder, which is shown in right Fig. 4.7. The amount of noise in the images makes quantitative analysis difficult. But the flow field gives a general sense of granular particle motion in the pull-out process.

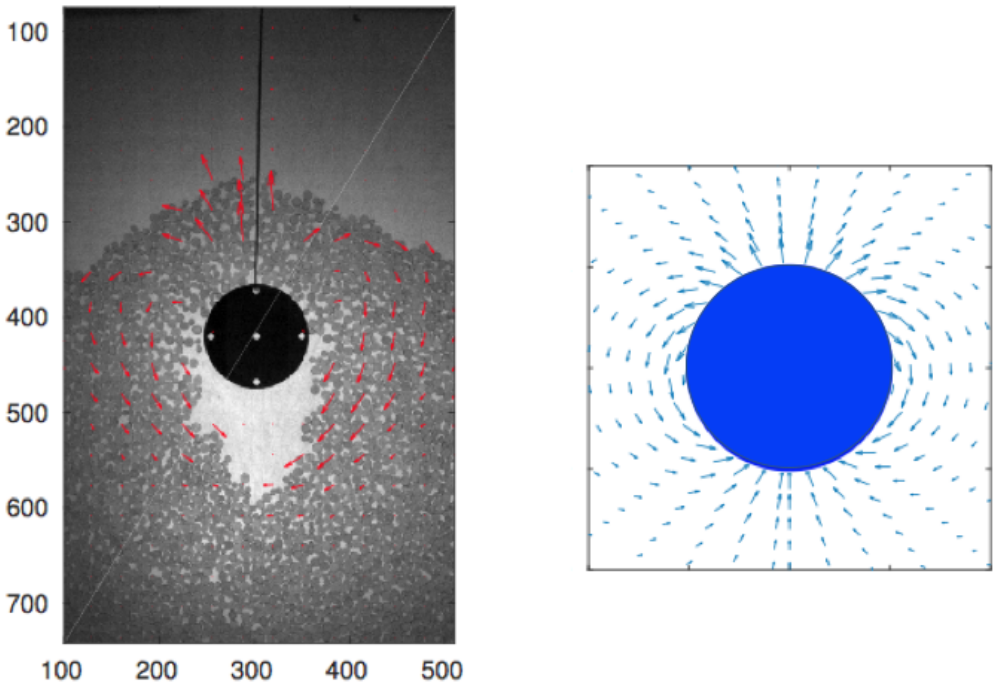

FIGURE 4.7: Left: Velocity field at the 7000th frame in a quasi-2D granular system in a pull-out experiment with a frame rate about 5000 fps. Here red arrows represent local velocity. Right: Velocity field around an infinite cylinder for a constant ideal fluid flow in the reference frame with fluid at rest at infinity. (In the lab reference frame, the constant fluid flow is from top to bottom at infinity point.) Here arrows represent the local velocity and circle represents a cross section of an infinite (into the plane) cylinder.

4.3 Stick-slip phenomenon

Here, I characterize stick-slip in the pull-out experiment, and compare it to other stick-slip phenomena. In a block-plane spring system, stick-slip is caused by the difference between larger static friction coefficient and smaller dynamic friction coefficient for the same contact surface(Braun et al., 2009). Specifically, as shown in the Fig.4.8, when the block on the table is pulled by a spring, the block will stay still when the spring is not stretched enough, which is the "stick" process. Once the spring has a large enough deformation to provide a pulling force at least as great as

the static friction force on the block from the surface, the block will start to move until the block comes to rest and the spring is relaxed so that pulling force is smaller than the static friction on the block from the surface. This is the "slip" part.

Stick-slip phenomenon can also be found in granular materials under certain loading. In granular medium system, similar stick-slip behavior is mainly caused by the friction between grains and interlocking of grains.(Albert et al., 2001) However, as the particles' dilatancy varies, the friction threshold for the granular medium is not constant as in block-plane system for each shift.

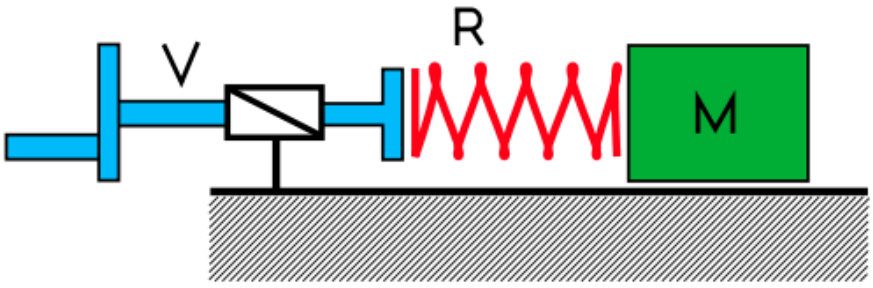

FIGURE 4.8: Stick-slip for block on the table(Kligerman and Varenberg, 2014). The block (M) on the table is pulled to the left with a spring (R). The block will stay still when the spring is not stretched enough, which is the "stick" process. Once the spring has a large enough deformation to provide a pulling force at least as great as the static friction force on the block from the surface, the block will start to move until the block comes to rest and the spring is relaxed so that pulling force is smaller than the static friction on the block from the surface. This is the "slip" part.

A related stick-slip phenomenon can be found in my pull-out experiment. The intruder starts in a "stuck" state when a constant load is added. Then the intruder starts to move out. Intuitively, the resistance on the intruder comes from the granular materials above the intruder, and it should decrease monotonously because the particle number above the intruder decreases monotonously. However, the acceleration of the intruder does not monotonously increase. Some loops can be found in Fig. 4.3, because the grains reorganize during the process, creating renewed resistance to the intruder. During that time, the acceleration drops significantly. This is another

example of stick-slip in granular materials.

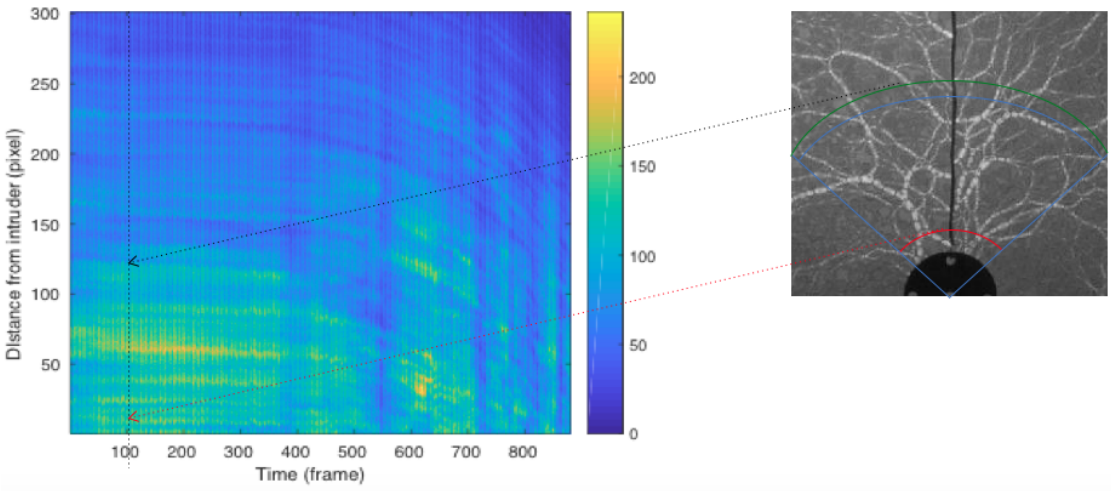

FIGURE 4.9: Space-time graph and its physical meaning. I average the intensity on an arc with width of 1 pixel between 45° and 135° , which gives us one point in the space time graph. The color bar shows the magnitude range of the averaged intensity on the arc after removing the background intensity. Local stresses in the granular system are proportional to local averaged intensities of images.

To visualize what is happening during the fluctuations of the acceleration, we plot space-time graphs of the image intensity. As shown in the left graph of Fig. 4.9 , the x-axis is time with units of frames, and the y-axis is the distance above the intruder in units of pixels. The right graph of Fig. 4.9 is part of a typical experimental image. I average the intensity on an arc with width of 1 pixel between 45° and 135°, which gives us one point in the space-time graph. Brighter colors in the space-time graph represent higher pressure inside the arc area at that particular time during the pull-out dynamic process. The failure event in this run is marked by the vertical blue band at frame 400. The horizontal striations in intensity before that time are grain scale effect due to inhomogeneities in the stresses on single grains.

Vertical gaps in the intensities in Fig. 4.10 represent moments the force network has broken and the intruder is accelerating more rapidly. This local fluctuation in

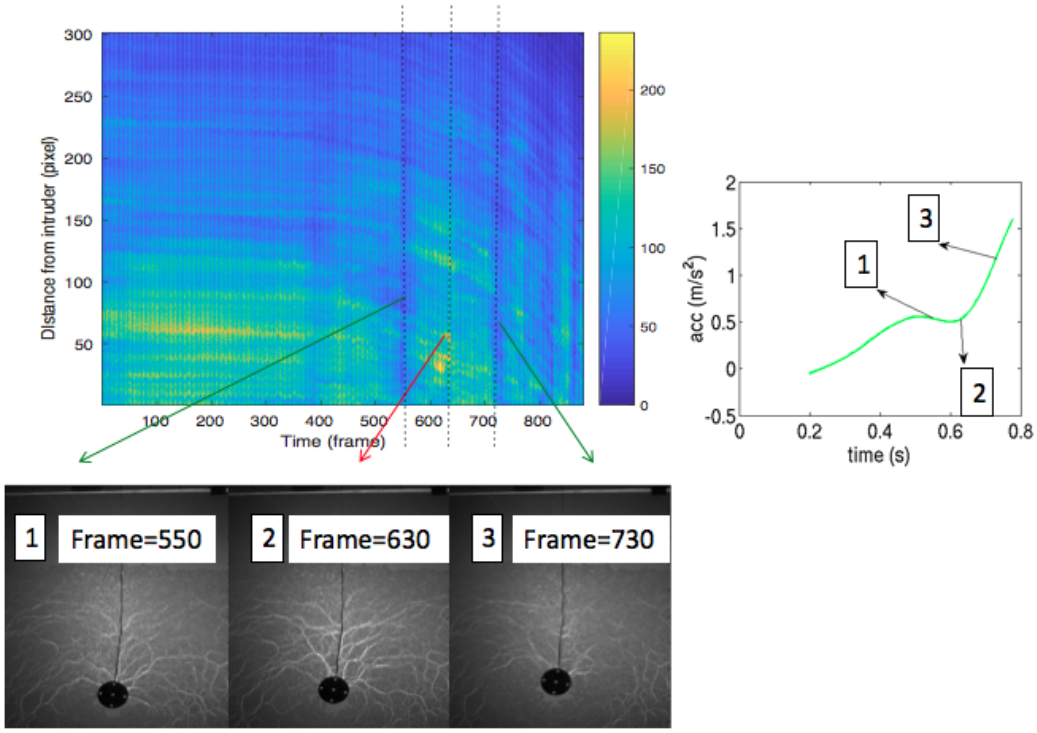

FIGURE 4.10: Discontinuities in space-time graph corresponding to fluctuations in acceleration. In the upper left space-time graph, the yellow (bright) vertical strips correspond to strong force networks above the intruder at a particular moment, as pictured around Frame=630, while the blue (dark) vertical strips correspond to weak force chains above the intruder, as pictured around Frame=550 or 730. During the pull-out process, force chains build up (from frame=550 to 630) and break down (from frame=630 to 730), giving rise to the fluctuation in the acceleration. The image on right shows the fluctuation in the smooth acceleration calculated from the slope of a linear fit of 199 points in the velocity vs. time curve.

acceleration corresponds to the stick-slip process in the pull-out experiment.

4.4 Effect from intruder's initial depth

In experiments described in this section, the intruder is buried originally at different depths in the granular material, then pulled out with the same force, which is large enough to achieve pull out of the deepest buried intruder. In this section, all of the dynamic experiments are conducted with the same intruder whose radius is 10.2cm. From the static result in chapter 3, we know the smallest force needed to pull the intruder out increases with the initial depth of the intruder. So we can use the force, which is just big enough for the deepest positioned intruder, to pull the intruder out from different original positions. We obtain the position of the intruder over time, as shown in Fig. 4.11. (The t=0 s point is chosen when intruder position has changed by 0.02m.) To simplify the description, we define a quantity $h = H_p - d_0 - r_{intruder}$, which represents the initial position. In this equation, $H_p = 0.63m$ is the height of granular bed, d_0 is the initial depth of the intruder and $r_{intruder} = 0.102m$ is the radius of the circular intruder.

In the position vs. time figure (Fig. 4.11), there are data for three different initial depths, h=0.1 m, 0.18 m and 0.26 m, corresponding to the three clusters of collapsed curves in the figure. Different colors in each cluster are several independent runs with the same initial depth. The shapes of those position vs. time curves are similar for different initial depths.

Subtracting the initial position from the position of the intruder gives us the displacement of the intruder. As shown in Fig. 4.12, the displacement of the intruder can be fitted with an exponential function: $Z = a_z * \exp(b_z * t) - a_z$, where a_z and b_z vary for different initial positions. As shown in Fig. 4.13, parameters a_z and b_z increase if we bury the intruder shallower. The physical meaning of b_z is the reciprocal of the characteristic time for the pull-out process. If the intruder is buried shallower, it will take less time for the intruder to be pulled out. For a practical

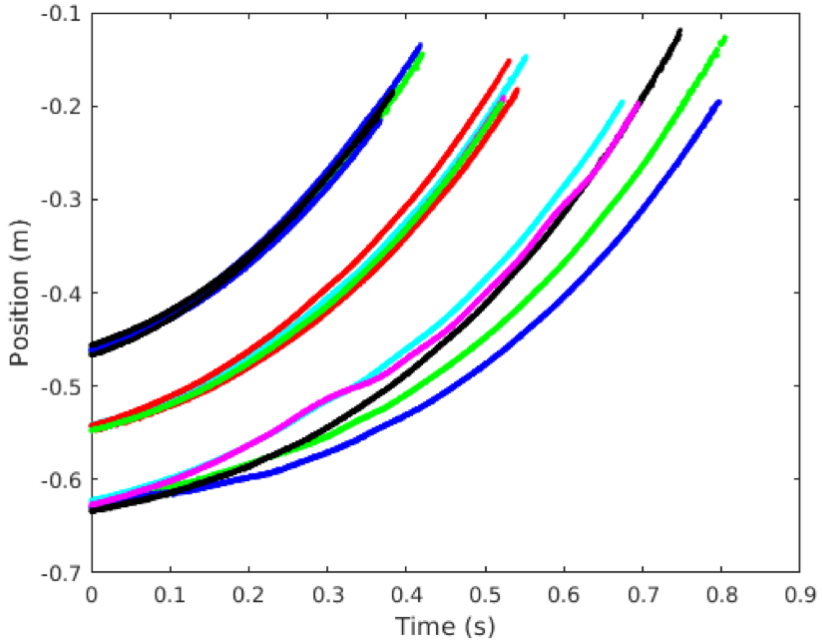

FIGURE 4.11: Relation between intruder position vs. time. The three bunches of collapsed curves represent three different initial positions of the intruder, while different colors in each bunch represent independent runs.

reason, time zero point is chosen when the intruder has moved 0.02m to collapse all the independent runs. Additionally, the 0.02m position is set as the new initial position, z(t=0)=0 m.

From the static experiments, we know that there is a dependence between the depth of the intruder and the smallest pre-failure force. So there might exist a dependence between the drag force on the intruder and the depth of the intruder during the pull-out process. We can track the thickness of particles above the intruder even in the dynamic pull-out process because of the transparent glass filled with quasi-2D granular system. As the intruder moves up, the particle thickness above the intruder also changes. We track the top edge of the particles, which is part of the estimated calculation for the particle thickness above the intruder. This process yields the evolution for thickness of the particles above the intruder throughout

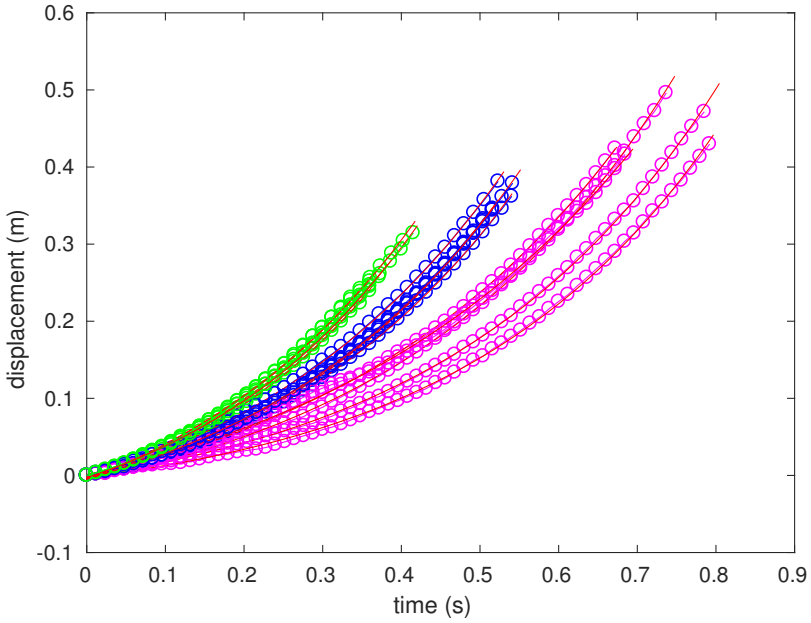

FIGURE 4.12: Fitting of intruder displacement vs. time with exponential functions. The three bunches of collapsed curves with different colors represent three different initial positions of the intruder. Pink circles represent 5 independent runs for the initial depth of 0.43m. Blue circles represent 5 independent runs for the initial depth of 0.35m. Green circles represent 5 independent runs for the initial depth of 0.27m. Red curves show fitting functions.

an experiment. The thickness is defined as the distance between the particles' top edge and the intruder center. This thickness can also be fitted with an exponential function: $T_p = a_p * (\exp(b_p * t) - 1) + T_0$, where T_0 is the known thickness of particles at t=0 s, and fitting parameters a_p and b_p vary for different initial positions. As shown in Fig. 4.15, a_p and b_p also increase if we bury the intruder shallower. The behavior of particles thickness and intruder's displacement are quite similar in the sense of the two fitting parameters' relation with intruder's initial depth.

Of the parameters in the intruder displacement and particles thickness fittings, the most interesting ones are the parameters b_z and b_p, whose reciprocals are both characteristic times. As shown in Fig.4.13 and Fig.4.15, the characteristic time for the particle thickness evolution is shorter than that of the intruder displacement for

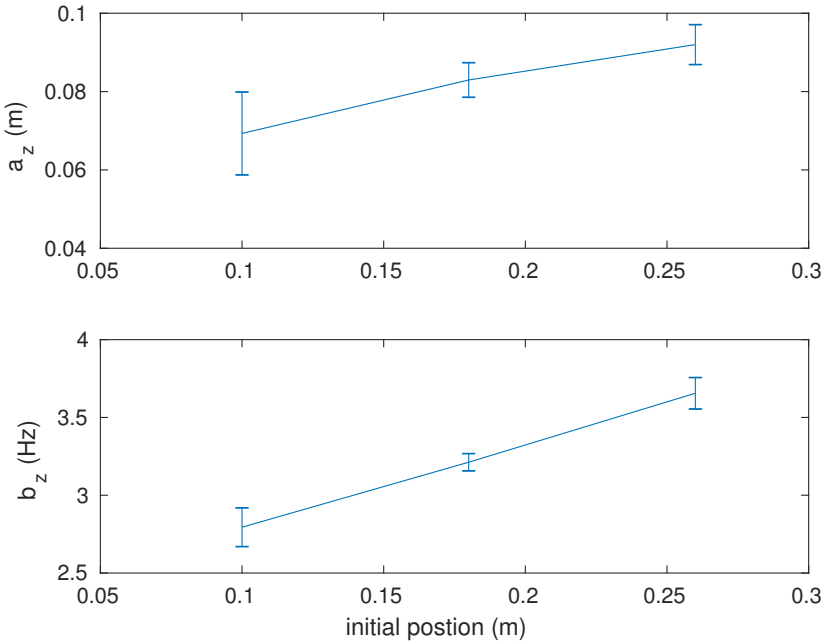

FIGURE 4.13: Parameters a_z (m) and b_z (Hz) in displacement fitting function vs. intruder's initial position h(m), where bigger h(m) means shallower intruder initially.

the same initial intruder position. I still do not quite understand why it works this way. Both characteristic times decrease as the initial position gets shallower. This is intuitively understandable as it takes a shorter time for a shallower intruder to come out with the same pulling force.

We want to understand the physics behind the exponential form fitting in this dynamics process. The first derivative of the displacement of the intruder gives us the intruder's velocity. The second derivative of the displacement of the intruder gives us the intruder's acceleration and the particle drag force acting on the intruder. Here the drag force (F_d) is calculated from the formula:

$$F_d = (W - M) * g - (W + M) * a_{intruder}, \tag{4.1}$$

where W is the mass of the bottle pulling the intruder, M is the mass of intruder, g is the gravitational acceleration, $a_{intruder}$ is the acceleration calculated from the second derivative of the displacement of the intruder. As shown in Fig. 4.16, we

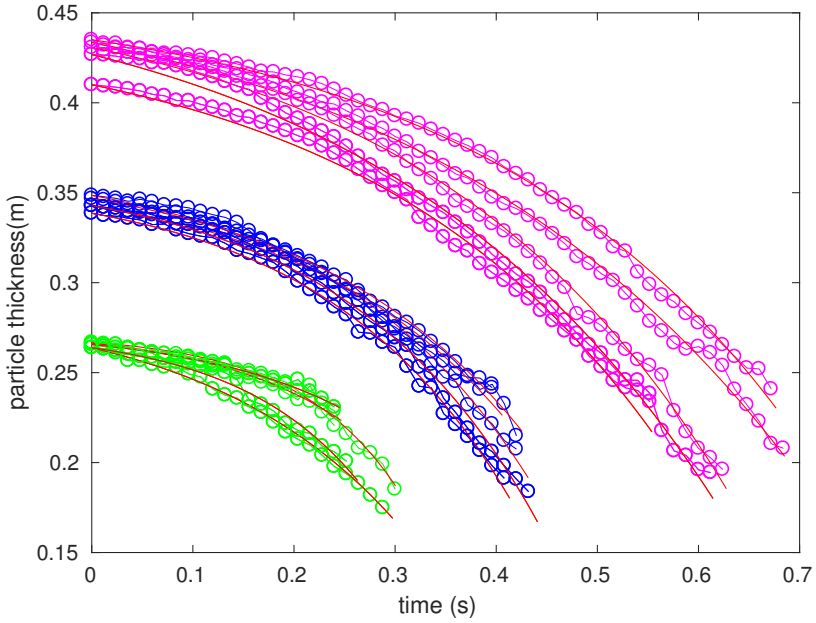

FIGURE 4.14: Particle thickness above the intruder vs. time. Curves with different colors represent runs with different initial positions of the intruder. Here, pink circles represent 5 independent runs for the initial depth of 0.43m, blue circles represent 5 independent runs for the initial depth of 0.35m, and green circles represent 5 independent runs for the initial depth of 0.27m. Red curves show fitting functions.

find that the acceleration changes linearly with velocity, ignoring the fluctuations caused by the stick-slip process associated with force chains. In the acceleration vs. velocity graph (Fig.4.16), the starting point is neither with zero velocity nor with zero acceleration, because the t=0s point is chosen when position has changed 0.02m to align different runs. Curves with different colors stand for runs with different initial positions of the intruder. Also, the granular drag force decreases during the dynamic process, which is shown in Fig. 4.17. Additionally, the drag force has a linear relationship with particles thickness above the intruder (in Fig.4.18). Here the particles thickness is calculated as the distance between the granular particles top edge and the intruder center.

As is shown in Fig. 4.18, the linear relationship aside from large stick-slip events between the drag force and the particle thickness suggests that the origin of drag force

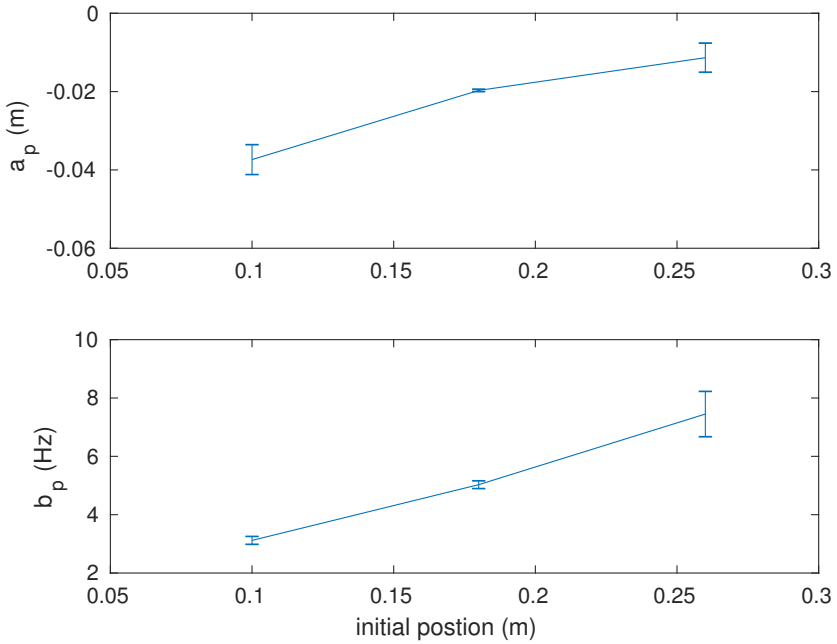

FIGURE 4.15: Parameters a_p (m) and b_p (Hz) in the particles thickness fitting function vs. intruder's initial position h(m), where bigger h(m) means shallower intruder initially.

is the weight of particles involved in the force network above the intruder. Also we can plot the ratio (α) between the drag force and particle layer thickness vs. the particle thickness, as in the Fig. 4.19. The value of α is around 10 N/m although it decreases a little during the pulling process. The density of the 2D granular particles is estimated to be about $2.77kg/m^2$, and a straightforward calculation indicates that the width of the particles involved is about 0.36m. This value for the width of "active" particles is reasonable, because the brightest force networks in the photoelastic images have a similar width range. Note that the intruder we use is about 0.204m in diameter, and from the subtracted photoelastic image data, the strong network's width is between one and two intruder diameters. When the intruder moves to the position close to the particle surface, the force chains widths become smaller.

The drag force from particles above the intruder also shows large fluctuations.

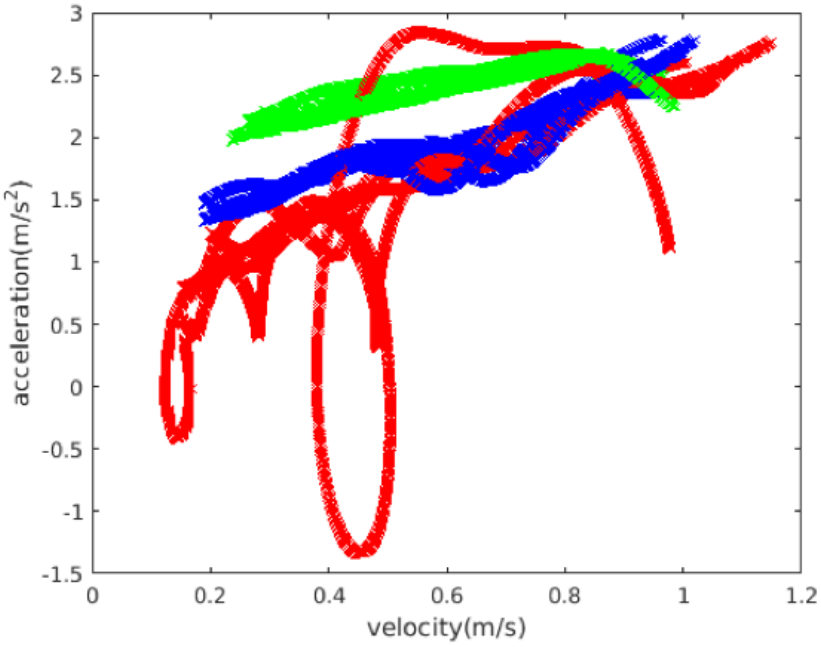

FIGURE 4.16: Intruder's acceleration vs. velocity during the pull-out process. Curves in different colors stand for runs with different initial positions of the intruder. Here, green curves stand for initial depth of 27cm, blue curves stand for initial depth of 35cm and red curves stand for initial depth of 43cm.

These fluctuations are stronger for deeper buried intruders, shown by comparing the red curves with the blue or green curves in the Fig. 4.17.

Without considering the fluctuations (or by just taking the average and eliminating the fluctuations), we can find a more mathematical way to describe the dynamics. As shown in the free body diagram Fig. 4.20, the intruder has three external forces, including the thread tension T, the gravitational force Mg, and the granular drag force F_d. The bottle has two external forces, including the thread tension T and the bottle gravity Wg.

The granular drag force F_d comes primarily from the weight of the grains above the intruder and also includes the collective effect of frictional forces between granular particles. The data in Fig. 4.18 indicates that F_d is proportional to the thickness of the layer of particles above the intruder. We made a crude assumption that this

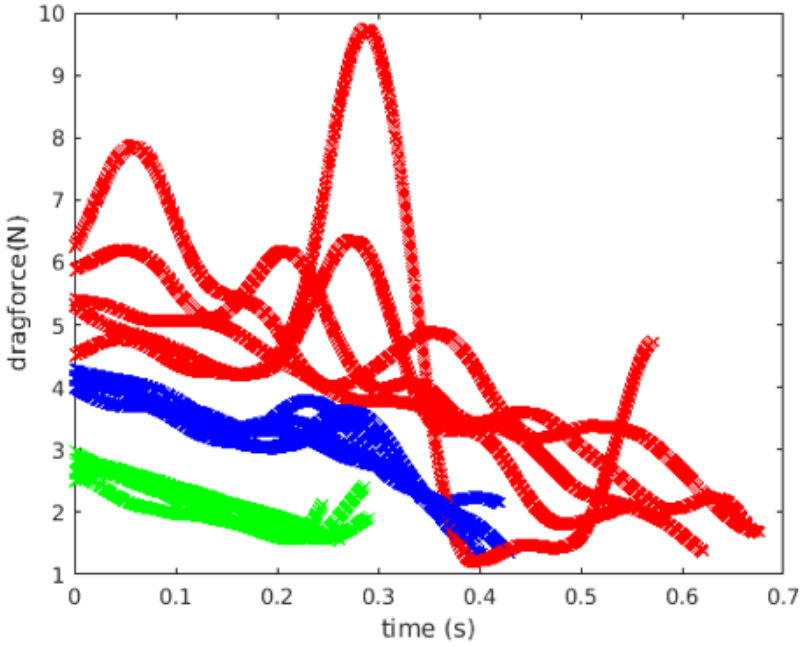

FIGURE 4.17: Drag force (N) from the particles acting on the intruder during the pull-out process vs. time (s). Curves in different colors stand for runs with different initial positions of intruder. Here, green curves stand for initial depth of 27cm, blue curves stand for initial depth of 35cm and red curves stand for initial depth of 43cm.

drag force term can be written as βd, where $d = d_0 - Z$.

Then the ODEs corresponding to the depth of the intruder (d) that describe the dynamic process are as follows:

$$Wg - T = -W\ddot{d} \tag{4.2a}$$

$$T - Mg - \beta d = -M\ddot{d}, \tag{4.2b}$$

where W is the mass of the bottle pulling the thread, T is the thread tension, M is the intruder mass, g is the acceleration of gravity, β is a ratio between the drag force and depth of intruder, d is the depth of intruder. The initial condition is:

$$d(t = 0) = d_0 \tag{4.3}$$

Additionally, there is a constraint requiring that the exponent inside the expo-

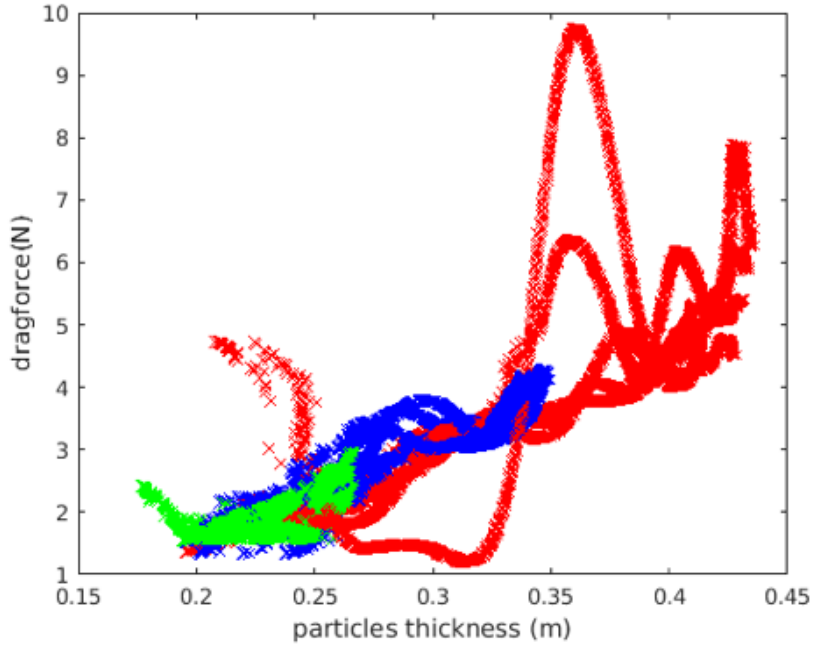

FIGURE 4.18: Drag force (N) from the particles acting on the intruder during the pull-out process vs. particles thickness above the intruder (m). Curves in different colors stand for runs with different initial positions of intruder. Here, green curves stand for initial depth of 27cm, blue curves stand for initial depth of 35cm and red curves stand for initial depth of 43cm.

nential function should be positive. (No negative exponents inside the exponential function is allowed in the solution.) Then we can solve these two ODEs by adding them together to eliminate the tension T. Finally, the solution to the ODEs ((4.2)) with initial condition (4.3) is

$$d(t) = (d_0 - \frac{(W-M)g}{\beta}) * \exp(\sqrt{\frac{\beta}{W+M}}\, t) + \frac{(W-M)g}{\beta} \tag{4.4}$$

This formula matches quite well with experimental data, as shown in Fig.4.21. (Note that the fitted points extend to negative values of d, where the justification for the drag force approximation is not clear.) The thick blue curves are plotted with intruder depth data and the thin red curves are from the formula (4.4) with only one tuned parameter, β. The graph shows that the model can well describe the

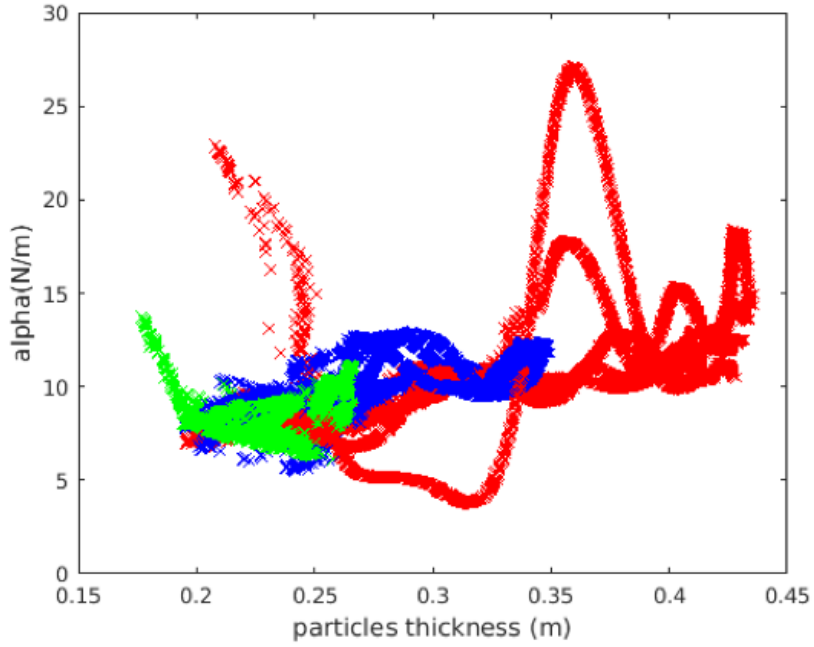

FIGURE 4.19: Ratio alpha (N/m) (between drag force and particle layer thickness) vs. particles thickness(m) above the intruder during the pull-out process. Curves in different colors stand for runs with different initial positions of intruder. Here green curves stand for initial depth of 27cm, blue curves stand for initial depth of 35cm and red curves stand for initial depth of 43cm.

dynamics of the intruder. But the fitting parameter β decreases with intruder initial depth. The value of β becomes closer to the value of α, if the intruder is buried deeper initially. The reason is that the thickness of particles is closer to the value to the intruder depth if the surface shape change during most of the pull-out process can be ignored.

To understand the dynamics of the intruder from another perspective, we consider the photoelastic response of the particles. First, we plot the space-time graph (Fig. 4.22) by mapping the intensity in arc lines of width one pixel above the intruder in each image vs. the image number. The x-axis is the image number, with a frame rate of 2500Hz. The y-axis is the pixel position of the arc with width 1 pixel and angle between 45° and 135° above the intruder. Yellow means stronger stress

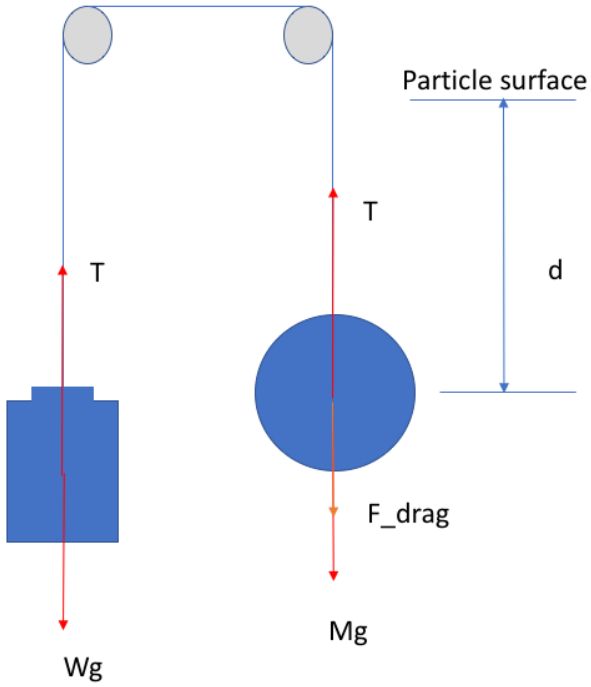

FIGURE 4.20: The free body diagram for the pull-out experiment. The intruder is connected through a thread with the bottle providing the load. The system can be separated into two objects, the intruder and the bottle. The intruder has three external forces: its own gravity Mg, the thread tension T and the granular drag force F_{drag}. The bottle has two external forces: its own gravity Wg and the thread tension T.

(larger intensity) while blue represents weaker stress (smaller intensity). The gaps, e.g. the blue strips between adjacent yellow regions from the 1400th frame to the 1600th frame in this space-time graph, correspond to the stick events, which are also revealed in the fluctuations in Fig. 4.16.

Also, if we focus on the time evolution of the average intensity in an arc of width 5 pixels at the position about 50th pixels above the intruder, we can calculate the Fast Fourier Transform (FFT) of the force evolution during the dynamic process of the pull out. We show the FFT on a log-log scale spectrum in Fig. 4.23. Red represents the deepest intruder case and green represent the shallowest intruder case. The data indicate an approximate power law with an exponent that varies weakly with depth

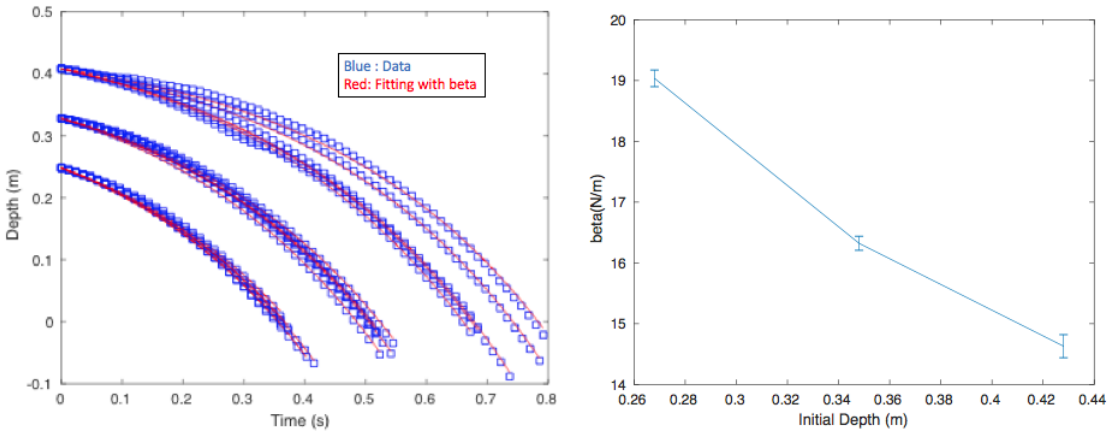

FIGURE 4.21: Intruder depth vs. time(s) curves and model matching curves with different intruder initial depths. Curves in blue stand for data plotted from trajectories of the intruder. Different starting points at t=0s stand for runs with different initial positions of the intruder. Curves in red represent the model (4.4) fitting curves, which end at the point when the intruder depth is 0.1 m (same as the intruder's radius). The only fitting parameter used is β, which decreases with initial depth of the intruder, as shown in right.

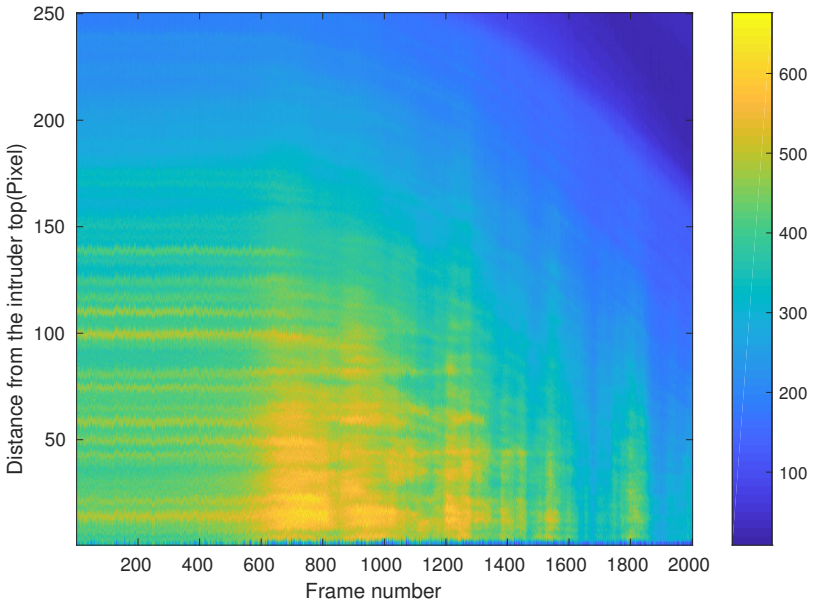

FIGURE 4.22: Space (in unit of pixel) vs. time (in unit of frame) graph. Y axis represents distance from the intruder and x axis represents time in the pull-out process. Video is taken with 2500 fps.

as shown in Fig. 4.24.

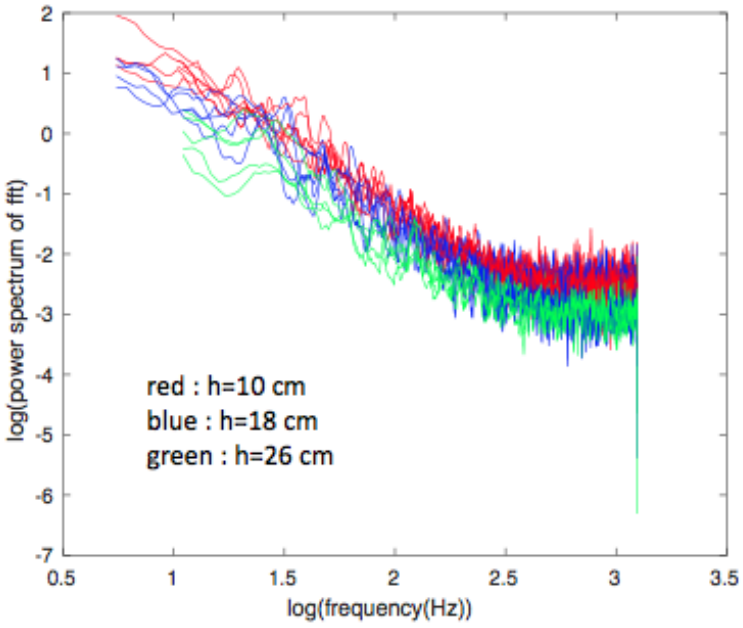

FIGURE 4.23: FFT power spectrum of intensity in the arc 50th pixel away from the intruder in log-log scale

Fig. 4.24 shows that, the shallower the initial depth, the larger the exponent of the power law of FFT power spectrum is. The exponent changes from -2.389±0.071 to -2.113±0.096, when initial depth changes from 0.53m to 0.37m. But the difference in the exponent for different initial depths is not large. The average of the slopes for all depths and runs is -2.268±0.056. Similar spectra can be obtained if we choose a different portion of the image in the intensity calculation. Many phenomena in nature have similar power laws for the spectrum, which is sometimes called Black noise.

The stress's relation with the local depth of the arc area chosen for the stress calculation is exponential during the pulling process, as shown in Fig. 4.25. The y-axis is the average intensity in an arc line (representing stress in that arc line) above the intruder on a log scale. The x-axis is the height of particles above the arc line

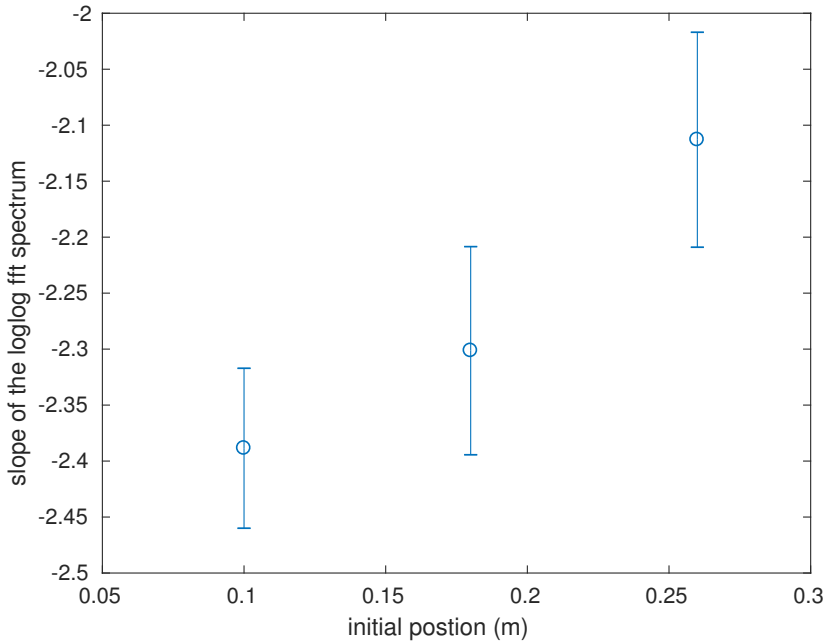

FIGURE 4.24: Slope in the FFT fitting vs. initial position h(m)

on a linear scale. Different colors represent different times (image numbers) during the pulling process. The blue curve is from the start of the experiment and the dark red curve is from the end of the pulling process. The movement of the intruder does not change the vertical distribution of stress during the pull out process. This result is quite striking.

Additionally, there are two methods used to calculate the drag force on the intruder, one is from the trajectory of the intruder and the other is from the photoelastic response of the granular disks above the intruder. When we average the intensity in the arc region above the intruder (as shown by Fig. 4.26) and normalize appropriately, we can match the drag force calculated from the intruder's position information (blue curve) and the photoelastic signal (red curves) in the Fig.4.27. Even the fluctuation in the drag force can be roughly matched. This graph supports the hypothesis that the drag force acting on the intruder mainly comes from the particles in an arc above the intruder (the 3rd term in ODE (4.2b)).

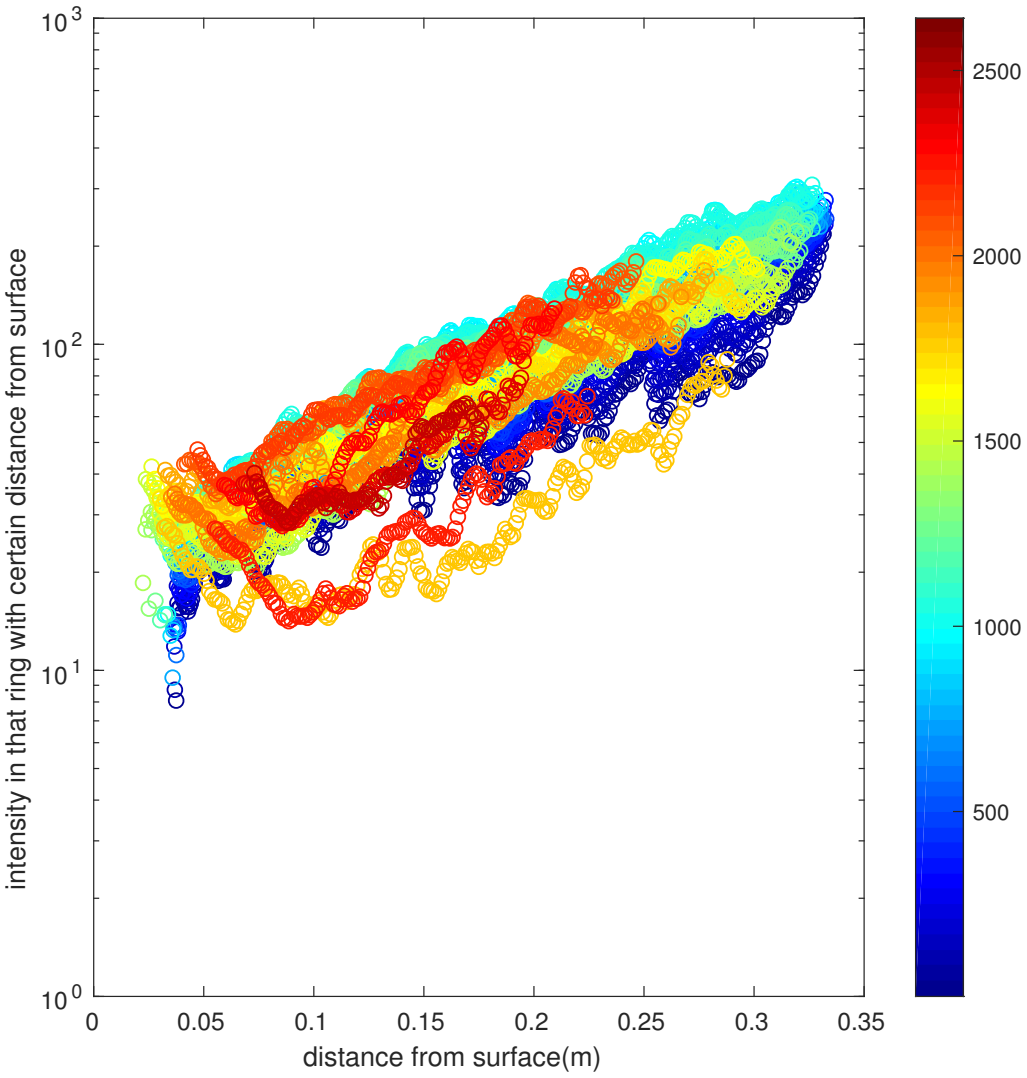

FIGURE 4.25: Stress (Intensity) in the particles for an arc of width 1 pixel between angle 45° and 135°above the intruder vs. distance from the arc top to the surface of granular system. The figure is plotted on a log-linear scale, indicating an exponential increase for the arc stress vs. thickness of particles above the arc. Different colors represent different times (with frame rate 2500 fps)during the pull-out process. For this run, the intruder had an initial depth of 43cm.

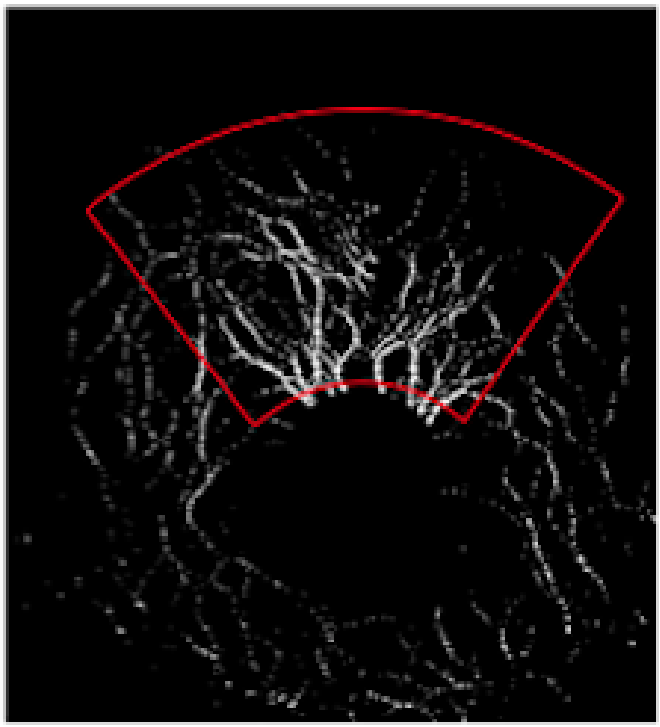

FIGURE 4.26: Arc region inside red boundary is used in calculation of drag force

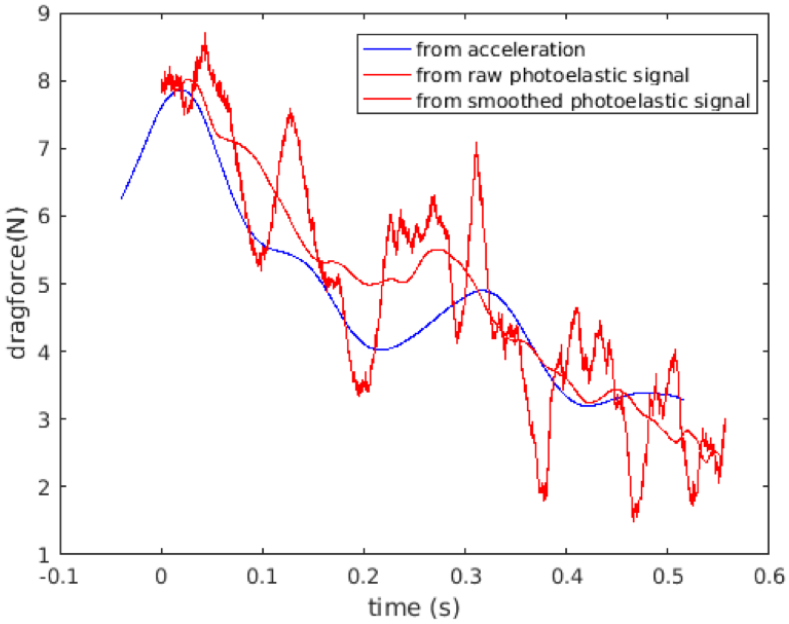

FIGURE 4.27: Drag force calculated by two different methods vs. time (for one run with initial position h=0.1m)

4.5 The boundary widths' effect

In this section, we use two aluminum bars to change the width of the granular system, and pull the circular intruder (r=10.2 cm) out of the granular material with the smallest critical pulling force found in the static pre-pull experiments. With the fast camera, we can capture the position of the intruder by taking 2500 frames per second. Using the position information, we can calculate the velocity and acceleration by differentiation.

Unlike the "peak " found for the medium boundary widths in the graph of the smallest critical pulling force vs. the initial depth of the intruder in pre-pull experiments, the dynamic pull-out experiments with different boundary widths do not show much variation. For every boundary width, we also have experiments with five different initial depths of the intruder, pulling with the critical forces found in corresponding pre-pull experiments. This is different from what was done in the last section where the pulling force is the same for different initial positions. We choose the time when the intruder displacement is 0.02m as t=0 for the same practical reason as former chapters. Then we reset the displacement to zero at t=0.

As shown by Fig. 4.28, the dynamics of the intruder pulled from the same initial depth 47.8 cm but with various boundary widths, are similar. Different colors represent different boundary widths. As mentioned before, we calculate the velocity and acceleration of the intruder by differentiating displacement data. Fig. 4.29 shows a roughly linear relation between the velocity and acceleration for different boundaries here. Specifically the boundary width of the granular system does not have much effect on the dynamic process of the intruder for the case where initial depth is 47.8 cm.

Given that there is a "peak" for an initial depth of 31.8 cm (h=18 cm, $depth_{intruder} = 60cm - h - r$ in this section) in the static pre-pull experiments for various widths,

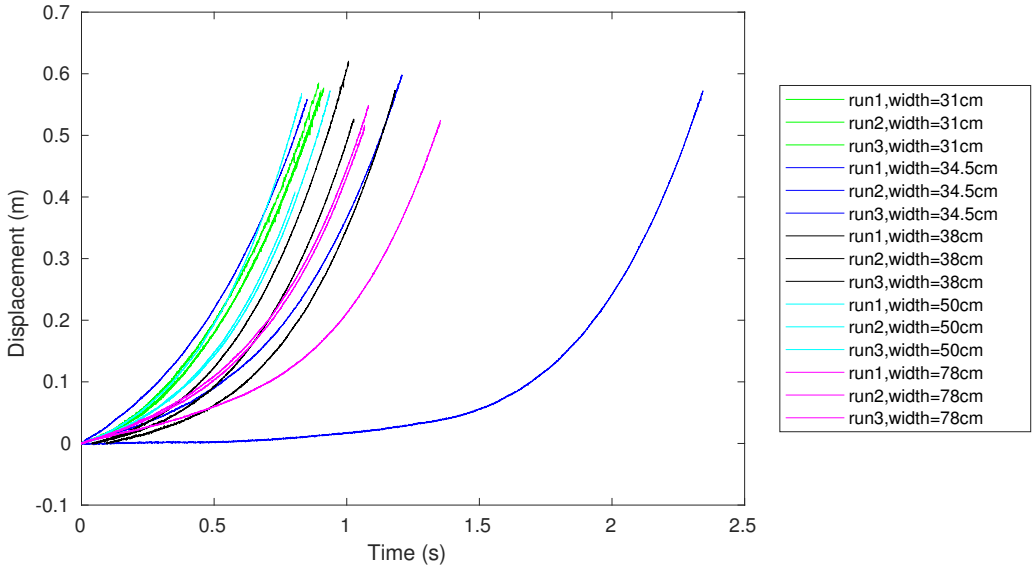

FIGURE 4.28: Displacement vs. time for motion of intruder (r=10.2 cm) pulled from granular system with different boundary widths from initial depth equals 47.8cm. Different colors represent different boundary widths and for each width there are three independent runs. There was one run of boundary width 34.5 cm with a delayed starting point because the intruder was stuck at first. But the delayed movement did not affect the dynamics of the intruder once it started to move.

we ask whether something unusual happens for that initial depth vs. the boundary width? The answer is no. For h ranging from 2cm to 26cm, and widths ranging from 31cm to 78cm, all runs have similar dynamics as long as the intruder is pulled with the critical pulling force, which varies for different initial depths and boundary widths. Specifically, we can fit the depth of intruder vs. time curves with the parameter β in model (4.4). For example, as shown in the Fig.4.30, intruder depth vs. time curves are fitted well with the parameter β when the system boundary width is 38cm and the intruder has five different initial depths.

In these experiments, we use the average minimum breaking force found in the static experiments for a given width and depth. (Sometimes the intruder cannot be pulled out for this force, so I ignored those and redid the pull out experiment.) The quantity β used to fit the dynamic curves of intruder depth is a characteristic

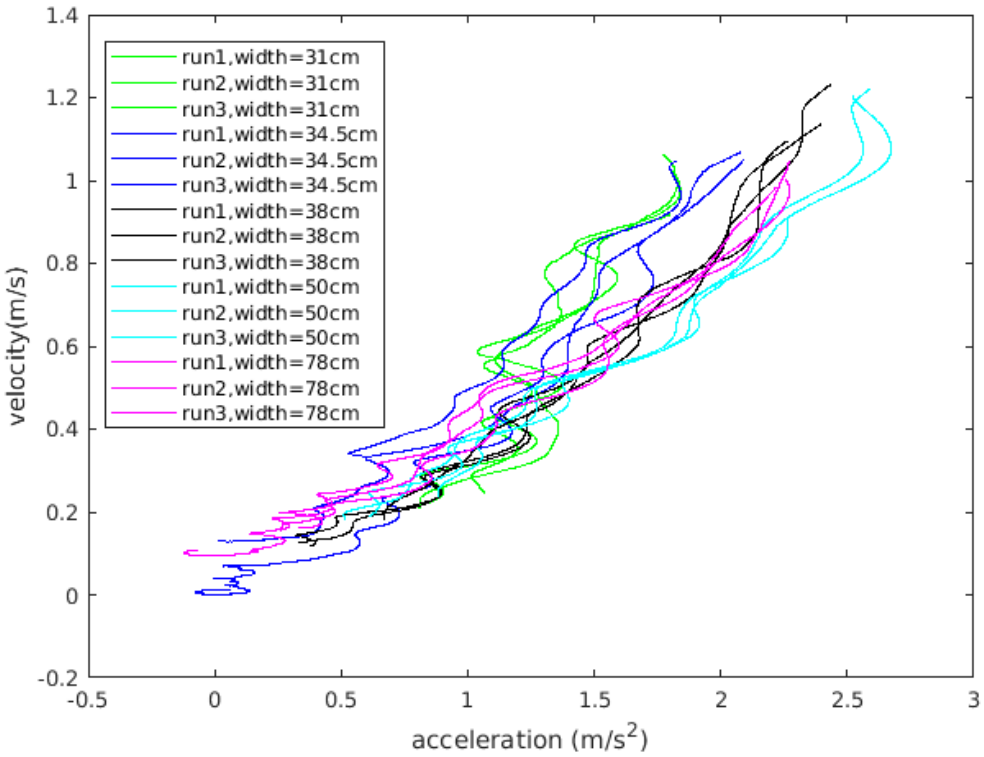

FIGURE 4.29: Velocity vs. acceleration for motion of intruder (r=10.2 cm) pulled from granular system with different boundary widths from initial depth equals 47.8cm. Different colors represent different boundary widths and for each width there are three independent runs.

quantity that can be used to describe the pull-out process. It is shown in Fig. 4.31, Fig. 4.32 and Fig.4.33 that the quantity β depends on the depth of intruder and pulling force on the intruder, but not on the width of the granular system. This means the boundary effect is limited for the pull-out dynamic process.

These data show that the frictional boundaries widths play a more important role in stabilizing the static granular system, but once the intruder starts to move, the effect from the boundary can be ignored.

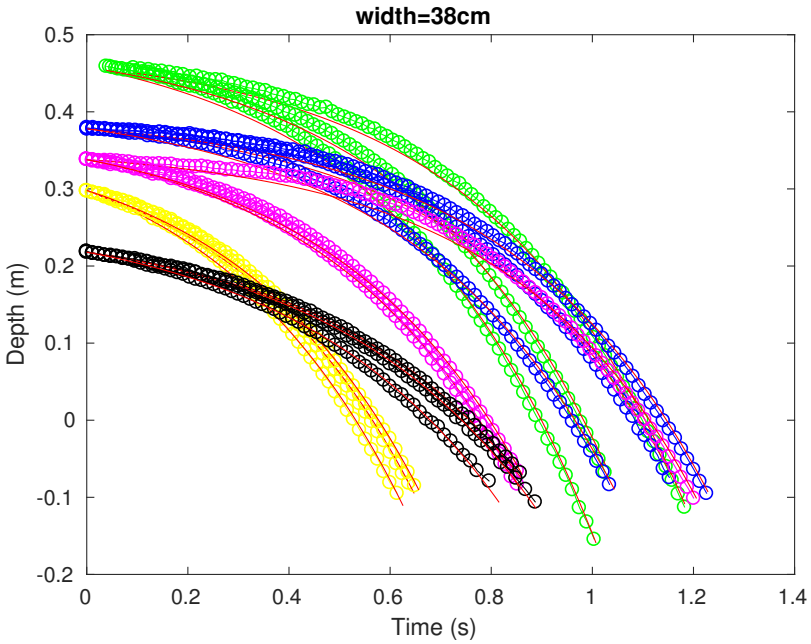

FIGURE 4.30: Depth vs. time for motion of an intruder (r=10.2 cm) pulled from the granular system of boundary width 38 cm with different initial depths (here black curves stand for depth of 23.8cm, yellow curves stand for depth of 31.8cm, magenta curves stand for depth of 35.8cm, blue curves stand for depth of 39.8cm, green curves stand for depth of 47.8cm). Each depth case has three independent runs. The thin red lines above those data curves are model fitting curves with β.

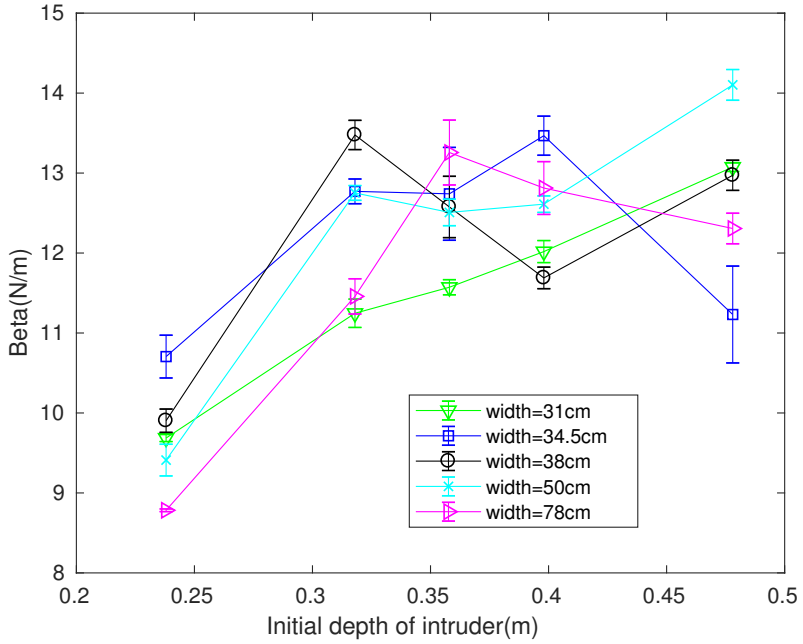

FIGURE 4.31: Beta vs. intruder initial depth for various boundary widths. Here β is the fitting parameter used in the model (4.4). Here green curves stand for width of 31cm, blue curves stand for width of 34.5cm, black curves stand for width of 38cm, cyan curves stand for width of 50cm, magenta curves stand for width of 78cm. Each data point has three independent runs and the error bars are calculated from standard deviations. β does not vary much for different boundary widths. However, the smallest β (around 10N/m) appears for the shallowest intruder regardless of the boundary width. All other runs with deeper buried intruders have a beta value around 12N/m.

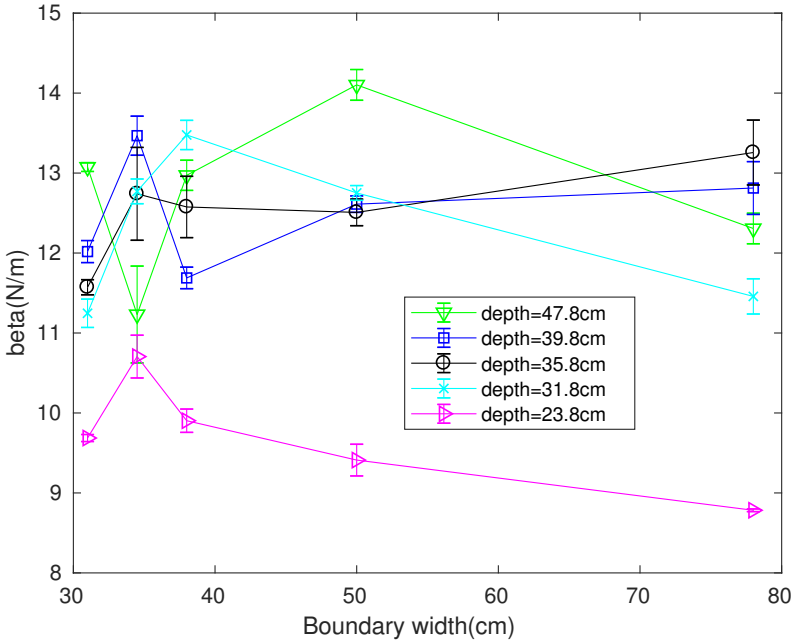

FIGURE 4.32: Beta vs. boundary widths for various intruder initial depths. Here magenta curves stand for depth of 23.8cm, cyen curves stand for depth of 31.8cm, black curves stand for depth of 35.8cm, blue curves stand for depth of 39.8cm, green curves stand for depth of 47.8cm). Each data point has three independent runs and the error bar are calculated from standard deviation. β does not vary much for different boundary widths. However, the smallest β appears for the shallowest buried intruder regardless of the boundary width.

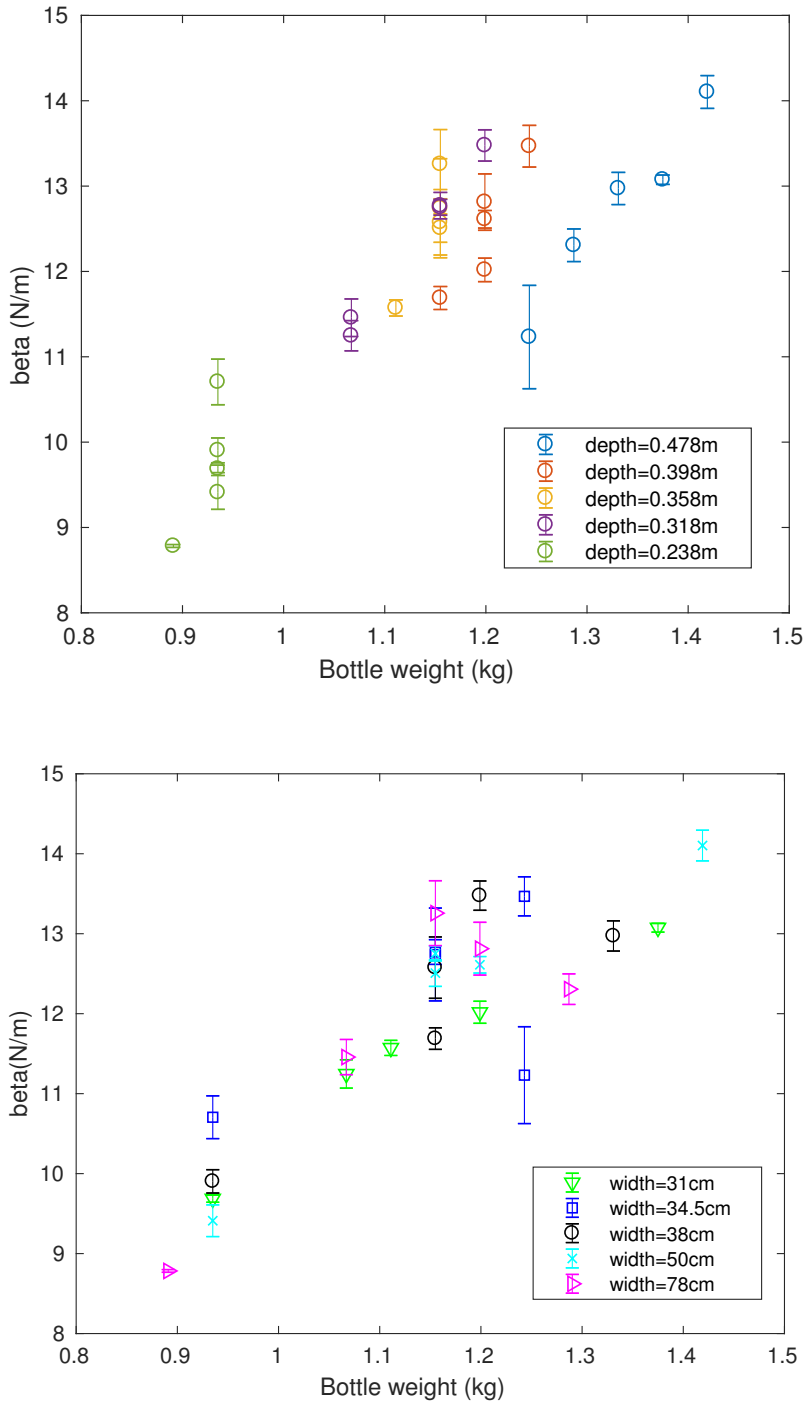

FIGURE 4.33: Beta vs. Bottle weight(pulling on the intruder) for various intruder initial depths and boundary widths. Each data point has three independent runs, with the standard error plotted as the error bar. This figure has two copies to indicate the intruder initial position and boundary width for each data point. This result indicates that β increases with the loading weight of bottle.

5

Force chain behavior in static pre-failure experiments

As shown in the chapter 3, when the loading on the intruder is increased incrementally in the static pre-failure experiments, the photoelastic response above the intruder becomes stronger and stronger until the whole granular system fails. The response of the granular system near the critical breaking point will be characterized with a pattern of force chains in this chapter. A continuous model (Blumenfeld, 2004) for an isostatic system can be applied to this critical state. For this chapter, no side boundaries will be considered as in the continuous model the system is treated as infinitely large.

5.1 Patterns of force chains near the critical breaking point

One typical polarized image taken near the critical breaking point is shown below in Fig. 5.1. With a loading close to the critical breaking point, most of the strongest force chains are found above the intruder. In the image, the dark circle in the middle is the intruder and the brighter chains are stronger. The most interesting part of the

image is marked out with the red rectangle.

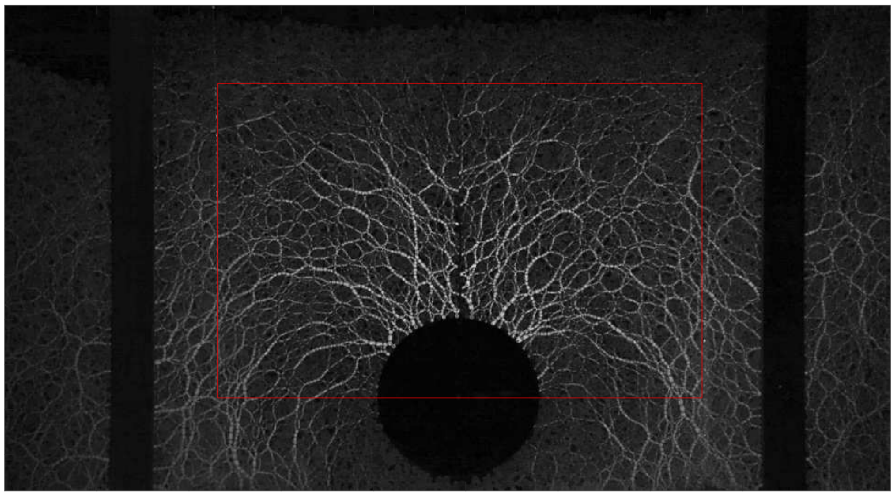

FIGURE 5.1: One typical polarized image in a pre-failure experiment near the critical breaking point. Brighter regions correspond to stronger stresses inside the granular system.

After a proper threshold is chosen and the force chain components inside the rectangle are extracted, the coordinates of force chain positions are transformed from Cartesian coordinates to polar coordinates. The threshold effect will be explained in the third section of this chapter. All positions of force chains are recorded in units of pixels. There are certain patterns in the positions and shapes for those force chains, as shown in Fig. 5.2. The trajectories of the force chains satisfy a linear relationship between θ and $ln(r)$. The linear relation (with slope called λ) between θ and $\ln(r)$ for force paths is consistent with the characteristic paths found in Blumenfeld and

Ma's continuum model(Blumenfeld, 2004; Blumenfeld and Ma, 2017), which will be discussed in the next section. Also I plot the relation between the slopes λ and the original angles of the force chains θ_0, as shown in Fig. 5.3. Here the original angle of a force chain is defined as the angular coordinate of the point with the smallest r-coordinate. The origin of polar coordinate is set at the center of the intruder. θ ranges between 0 and π, and only the upper part of image above the intruder center is considered.

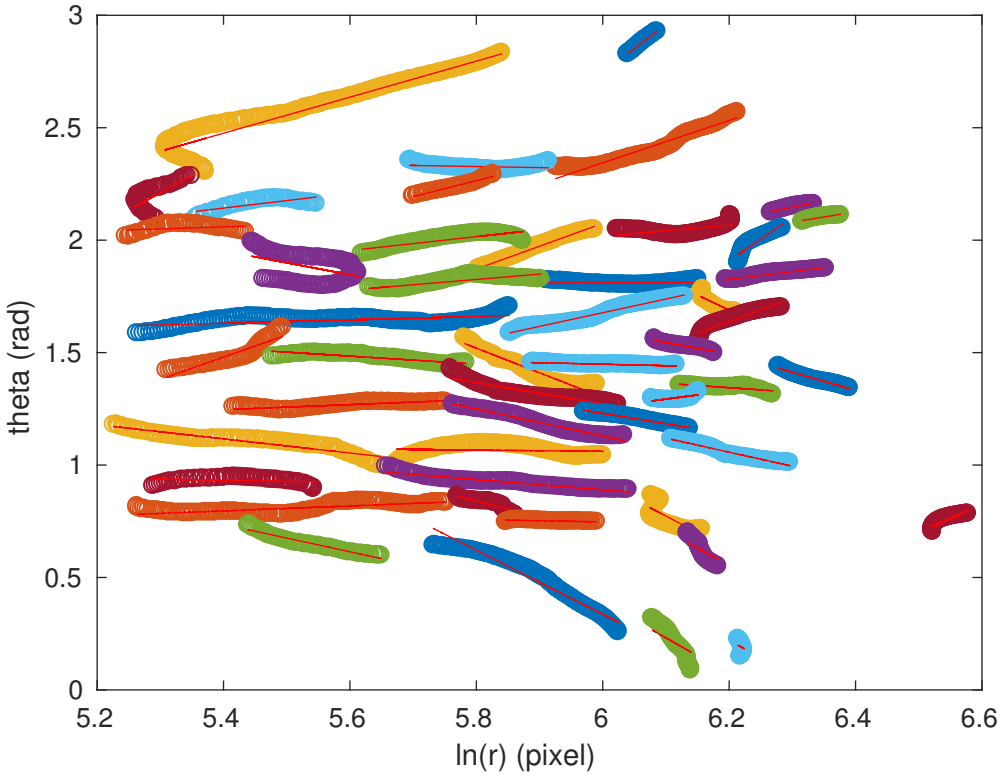

FIGURE 5.2: Force chain patterns found near the critical breaking point. The intruder used is with radius 10.2cm and the initial depth is 48.8cm. The force chains inside the rectangle with intensity above a certain threshold(50) are detected and mapped in the polar coordinate. Then all the force chain trajectories (different colored curves) are fitted linearly between θ and $ln(r)$ with red thin lines. λ is the slope in the linear fitting, $\theta - \theta_0 = \lambda ln(r/r_0)$.

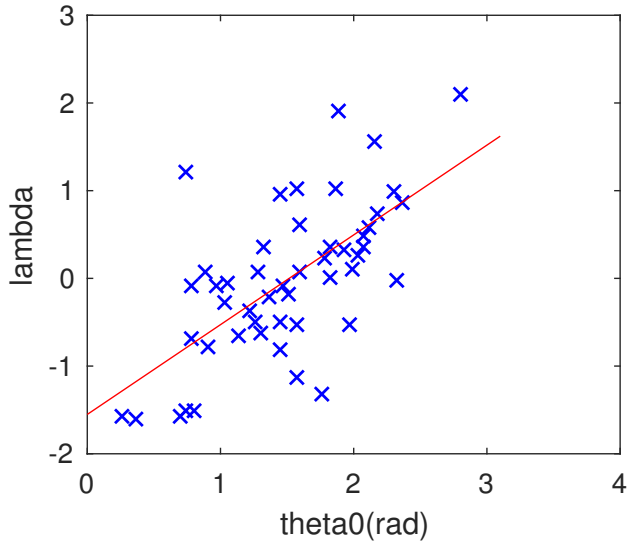

FIGURE 5.3: Linear fit between the slope λ and θ_0: $\lambda = 0.94 * \theta_0 - 1.41$, near the critical breaking point.

However, for a smaller load case, e.g., far below the breaking critical point, the pattern of force chains is different. Here, I process one typical image as shown in Fig. 5.4. After I extract the force chains with the same threshold and transform the Cartesian coordinates to polar coordinates, the coordinates θ vs. $ln(r)$ of force chains can no longer be well fitted with straight lines (with slope called λ), as shown in the Fig. 5.5. The pattern of force chains is apparently different from the one close to critical breaking point. Also, we can plot out the relation between the fitting slope λ and θ_0, and the data can not be fitted with linear line, as shown in Fig. 5.6.

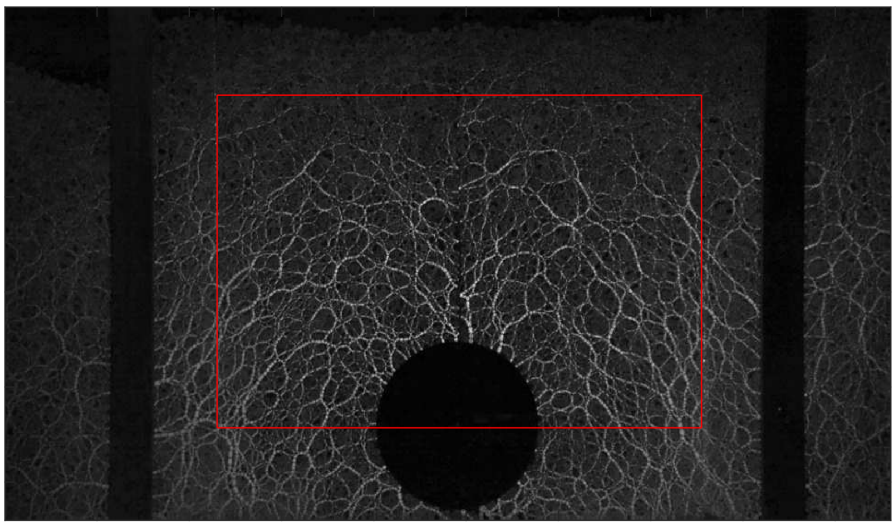

FIGURE 5.4: One typical polarized image in pre-failure experiment far below the critical breaking point. Brighter part means stronger stress inside the granular system.

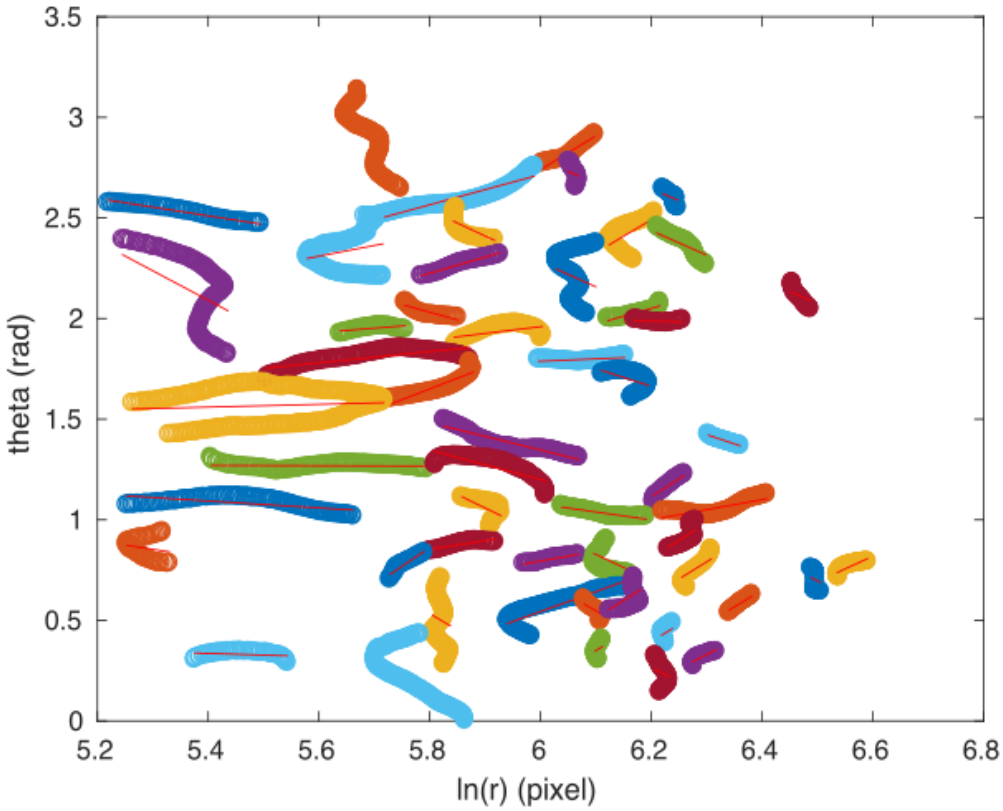

FIGURE 5.5: Force chains patterns found far below the critical breaking point. The force chains inside the rectangle area with intensity above a certain threshold(50) are detected and mapped in polar coordinates. Then all the force chain trajectories (different colored curves) are fitted linearly between θ and $ln(r)$, shown by red thin lines. As shown in the graph, the fittings do not collapse well with mapped force chains. The slope in the linear fitting is also called λ, although the λ is not well defined.

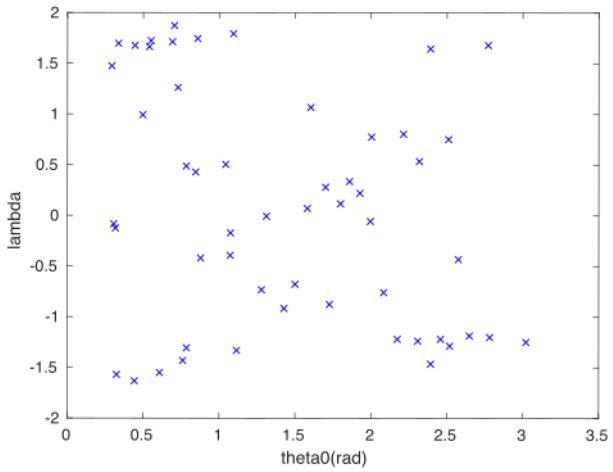

FIGURE 5.6: The slope λ vs. the original angle θ_0 far below the critical breaking point. No linear fit makes sense for λ vs. θ_0 calculated with the image taken far below the critical breaking point.

5.2 A continuous model near the critical breaking point

The granular material in the pre-failure pull experiment are close to an isostatic state when the loading is close to the critical breaking point. Here the isostatic state means a marginal stable state with average contact number of each particle close to 3 for this quasi-2D frictional system. For isostatic and spatial uniform system, a continuous model can well describe the stress distribution inside the granular system, as shown by R. Blumenfeld et al. (Blumenfeld, 2004; Blumenfeld and Ma, 2017). The force balance equation is as follows:

$$\nabla\sigma = \boldsymbol{g} \tag{5.1}$$

σ is the stress tensor in the isostatic granular system and the $\boldsymbol{g}$ is the body force in the granular system. In the pull system, the only body force that needs to be considered is the gravity, which is a constant in the equation. In polar coordinates, the equations of stress balance can be rewritten as two PDEs:

$$\partial_r(r\sigma_{rr}) + \partial_\theta\sigma_{r\theta} - \sigma_{\theta\theta} = rg_r \tag{5.2a}$$

$$\partial_r(r\sigma_{r\theta}) + \partial_\theta\sigma_{\theta\theta} + \sigma_{r\theta} = rg_\theta. \tag{5.2b}$$

There are only three instead of four unknown components in the stress tensor, because torque balance requires $\sigma_{r\theta} = \sigma_{\theta r}$. Now we need another equation together with the above two PDEs to calculate the stress tensor. In the model of Blumenfeld et al., particles form a network that are connected through force loops, and the fabric tensors ($\boldsymbol{\pi}$) can be calculated from the force network. (Blumenfeld, 2004) The fabric tensor ($\boldsymbol{\pi}$) is correlated with the stress tensor, which gives a stress-structure relation. More specifically, the fabric tensor ($\boldsymbol{\pi}$) gives an equation that effectively removes one unknown stress tensor component:

$$\pi_{rr}\sigma_{\theta\theta} - 2\pi_{r\theta}\sigma_{r\theta} + \pi_{\theta\theta}\sigma_{rr} = 0 \tag{5.3}$$

The boundary conditions are also very important for the solutions of the PDEs (5.2). In our pulling system, the top semicircular surface of the intruder acts as part of the boundary, on which there are several point forces. For numerical simplification, we use several narrow Gaussian functions to represent those point forces. The system is assumed to be infinite in the horizontal directions, and the force on the horizontal line: θ=0 and $\theta = \pi$ is set to zero. For simplicity, we also take $\pi_{r\theta} = 0$ everywhere. Blumenfeld's theory predicts characteristic paths in the isostatic system that satisfy: $\theta - \theta_0 = \lambda \ln(r/r_0)$ with $\lambda = \widetilde{q_{r\theta}} \pm \sqrt{\widetilde{q_{r\theta}}^2 - \widetilde{q_{\theta\theta}}}$, where $\widetilde{q_{ij}} \equiv \frac{\pi_{ij}}{\pi_{rr}}$.(Blumenfeld and Ma, 2017) In the region $\frac{3}{8}\pi \leqslant \theta \leqslant \frac{5}{8}\pi$, we use the fits to λ from our stress measurements, which yield $\lambda = 0.94{*}\theta - 1.41$. Outside this region, we take λ to be constant matching the values on the $\theta = \frac{3}{8}\pi$ and $\theta = \frac{5}{8}\pi$ rays. Given $\pi_{r\theta} = 0$, we have $\pi_{\theta\theta}/\pi_{rr} = -\lambda^2$.

Thus our expression for $\pi_{\theta\theta}/\pi_{rr}$ is:

$$\pi_{\theta\theta}/\pi_{rr} = \begin{cases} -(0.94 * \frac{3}{8}\pi - 1.41)^2 & 0 < \theta < \frac{3}{8}\pi \\ -(0.94 * \theta - 1.41)^2 & \frac{3}{8}\pi \leqslant \theta \leqslant \frac{5}{8}\pi \\ -(0.94 * \frac{5}{8}\pi - 1.41)^2 & \frac{5}{8}\pi < \theta < \pi \end{cases} \tag{5.4a}$$

Solving Eqs. 5.2 and 5.3 using the Matlab function `pdex4`, we obtained the results for the stress tensor components σ_{rr} and $\sigma_{r\theta}$ shown in Fig. 5.7 and Fig. 5.8.

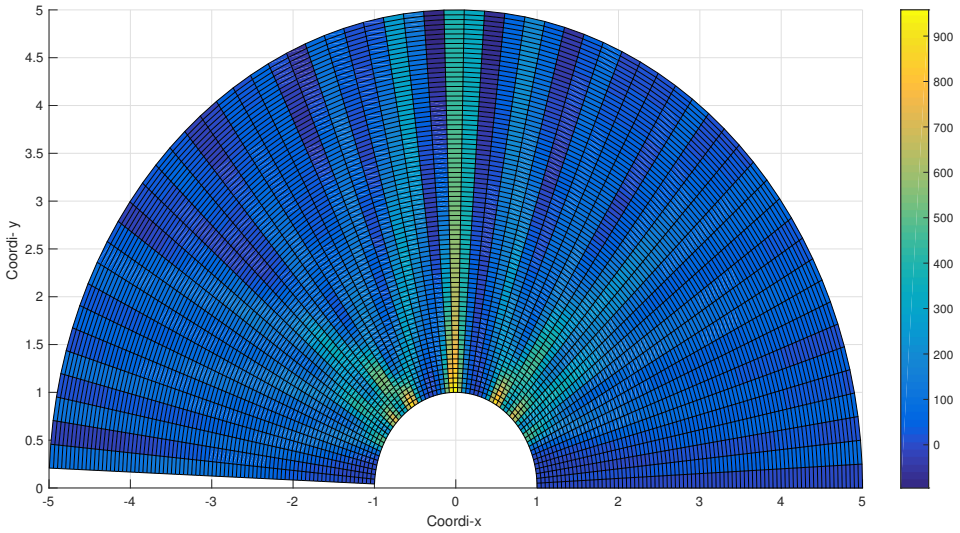

FIGURE 5.7: The distribution of the stress tensor component σ_{rr} in Cartesian coordinates from numerical solutions of the Blumenfeld model. Different colors represent different stress magnitudes. The white semicircle with radius 1 represents the upper half part of the intruder. The graph is not symmetric about line x=0, which is reasonable as the fabric tensor I choose is not symmetric.

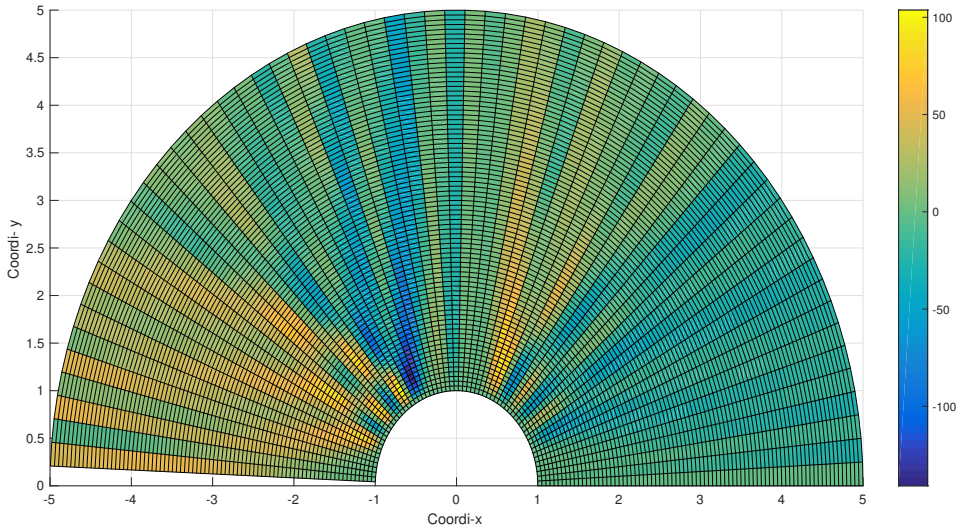

FIGURE 5.8: The distribution of the stress tensor component $\sigma_{r\theta}$ in Cartesian coordinate from numerical solution of continuous model. Different colors represent different stress magnitude. The white semicircle with radius 1 represents the upper half part of the intruder. Note the different color scale from Fig. 5.7.

Because σ_{rr} is an order of magnitude larger than $\sigma_{r\theta}$ and $\sigma_{\theta\theta}$, the light intensity in the experimental images is expected to be primarily determined by σ_{rr}, and we do observe a qualitative match: firstly, the bending of the force chains appear near the $\theta = \pi/4$ and $\theta = 3\pi/4$; secondly, there are strong, straight vertical force chains above the intruder. I do not calculate the fabric tensor from its original definition (Blumenfeld, 2004) because the experimental image resolution is not good enough.

5.3 Threshold effects on the analysis

The images taken in the pre-failure experiments are RGB images. In order to identify and extract force chains from the image data, we need to manually set a threshold. Only those image components with intensity above the threshold are identified as force chains, which provide the most important part for the stress field in the granular system. As there is not a principle in determining which value between 1 and 255

should be used as the threshold, we can try a few values to check their effect on the force chain calculations, as shown in Fig. 5.9.

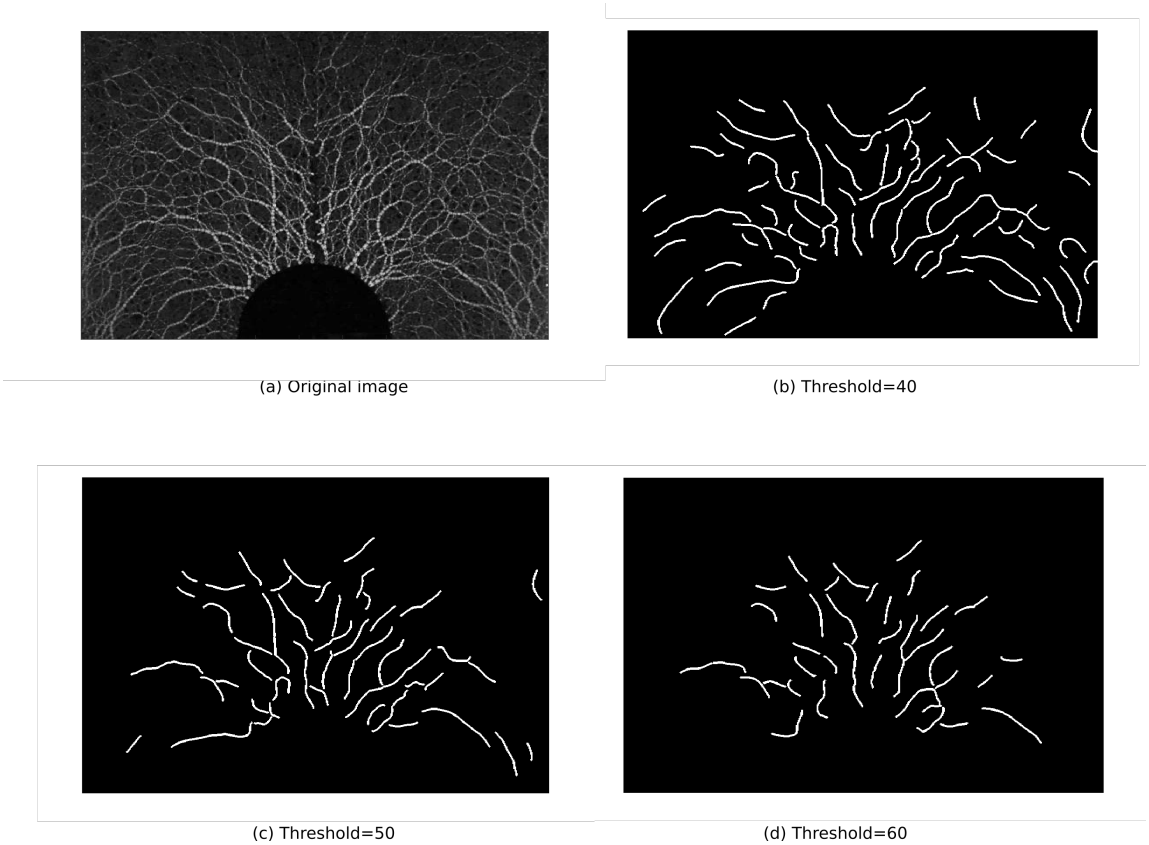

FIGURE 5.9: Force chains extracted near the critical breaking point with various different thresholds. The force chains inside the rectangle area with intensity above a certain threshold(40 or 50 or 60) are detected.

In the first section, I use the value 50 as the threshold for the image processing. If the threshold is 40 or 60, the results are not very different. As shown in the Fig. 5.10 and Fig. 5.11, most trajectories of force chains vary linearly between θ and $\ln(r)$. More and longer force chains are detected with a lower threshold.

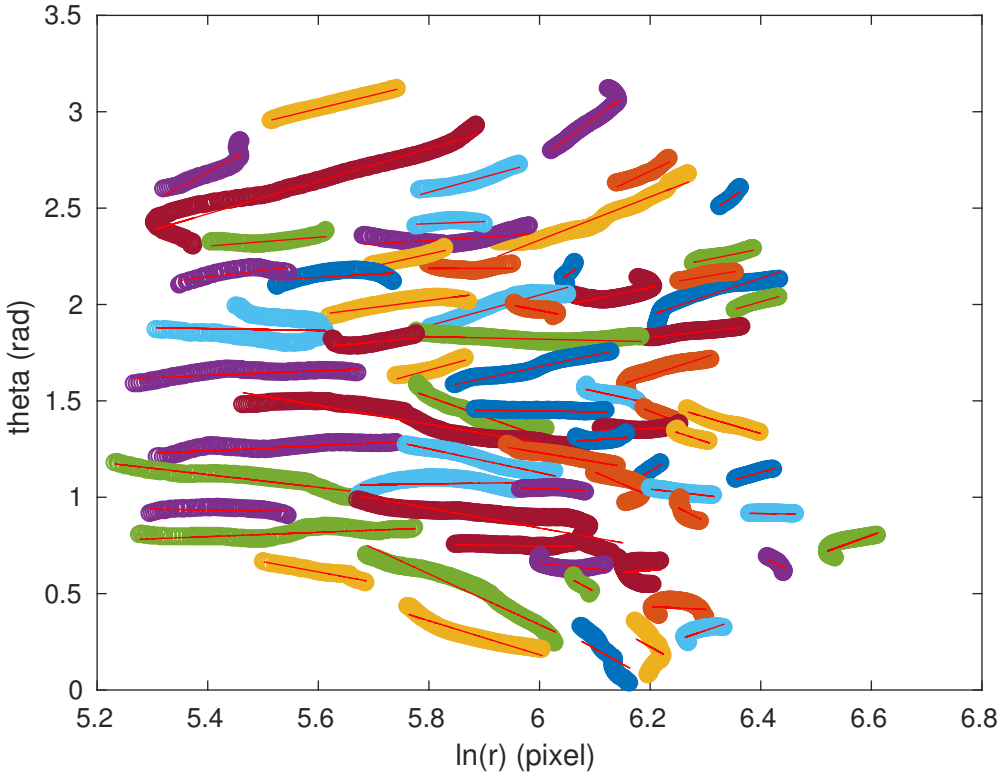

FIGURE 5.10: Force chains patterns found near the critical breaking point with threshold 40. The force chains inside the rectangle area with intensity above a certain threshold(40) are detected and mapped in polar coordinates. Then all the force chain trajectories (different colored curves) are fitted linearly, $\theta - \theta_0 = \lambda ln(r/r_0)$, shown by red thin lines.

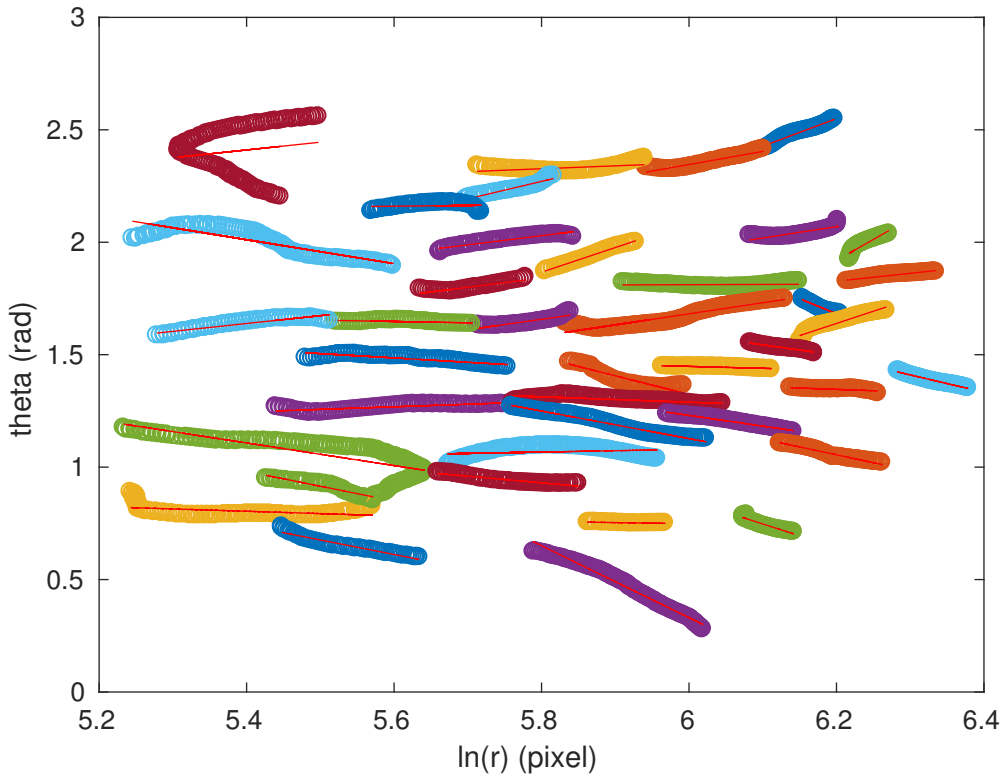

FIGURE 5.11: Force chains patterns found near the critical breaking point with high threshold 60. The force chains inside the rectangle with intensity above a certain threshold(60) are mapped in the polar coordinate. Then all the force chain trajectories (different colored curves) are fitted linearly, $\theta - \theta_0 = \lambda ln(r/r_0)$, shown by red thin lines.

Also as shown in the Fig. 5.12 and Fig. 5.13, the relations between λ and θ_0 are similar for both threshold cases. When threshold is 40, the relation is $\lambda = 0.75 * \theta_0 - 1.04$. And when threshold is 60, the relation is $\lambda = 0.86 * \theta_0 - 1.35$. These indicate that the λ is not sensitive about the threshold value. The pattern of the force chains for the isostatic system in the first section of this chapter is valid.

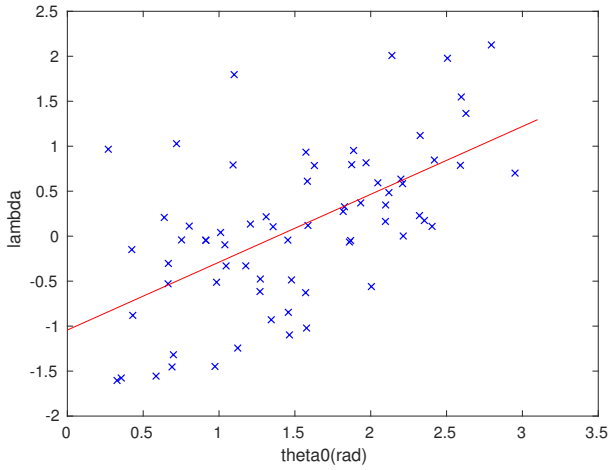

FIGURE 5.12: Linear fitting between the slope λ and θ_0: $\lambda = 0.75 * \theta_0 - 1.04$, near the critical breaking point, with a low threshold of 40.

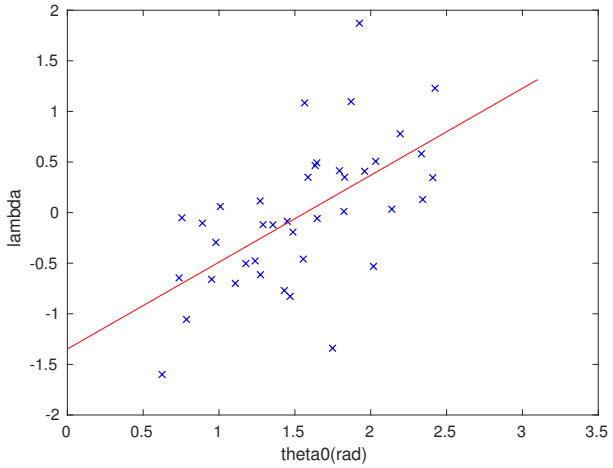

FIGURE 5.13: Linear fitting between the slope λ and θ_0: $\lambda = 0.86 * \theta_0 - 1.35$, near the critical breaking point, with a high threshold of 60.

6

Conclusions

This thesis describes experiments on pulling a circular object out of a granular system. Two types of experiments were performed with a bronze intruder embedded in a quasi-2D layer of photoelastic disks: the quasistatic pre-failure and the rapid dynamic pull-out. For the quasistatic pre-failure experiments, a Nikon D7100 camera is used to take videos at 30 frames per second as the pulling force applied to the circular intruder is steadily increased in small increments. For the dynamic pull-out experiments, a pulling force is applied that is bigger than or close to the critical pulling force found in the pre-failure experiment to get the intruder out. The dynamic process only lasts for about 2 seconds, a fast camera is used, operating at 2500 frames per second or 1000 frames per second.

6.1 Conclusions for static pre-failure experiments

There are several conclusions that can be reached from the data collected in the pre-failure experiment.

1) For sufficiently wide systems, the minimum force that is needed to pull the

intruder out increases monotonically with the intruder's initial depth. Additionally, if the boundary has no friction, the width of the system has little effect on the critical pulling force for the intruder. For frictional boundary walls, however, the width of the system matters. The increase of the critical pulling force with the initial depth of the intruder will no longer be monotonic but will fluctuate with depth for widths in the range [34.5cm, 50cm] for circular intruder size of 20.4 cm in diameter. The particles used in the system are of diameters 0.9cm and 0.6cm. With these geometric parameters, arches form that can create interactions with the boundary when the walls are sufficiently rough on the grain scale.

2) The intruder does not stay still when I add the pulling force step by step. The displacement of the intruder in each step becomes bigger and bigger when the total pulling force is increased up to the critical value, while the intruder still stays inside the granular system. During a complete pre-failure process, the total displacement of the intruder can reach up to about 2-3 particle diameters for the deepest (depth about 48cm) buried intruder (with radius of 10.2cm). If we increase the initial depth of intruder, the displacement that intruder can reach before the final failure of granular system will also increase monotonically, when the system is sufficiently wide. For narrower systems, the intruder's displacement will no longer monotonically increase with the initial depth.

3) The response of the granular system to the pulling force near the critical breaking point is characterized by a pattern of force chains. A continuous model (Blumenfeld, 2004) for an isostatic system can qualitatively describe this critical state, as the model can account for the bending of force chains shown in the photoelastic image. In the continuous model the system is treated as infinitely large. The model's prediction is qualitatively consistent with force

chain patterns observed in my sufficiently wide systems near the critical state.

6.2 Conclusions for dynamic pull-out experiments

There are also several conclusions that can be reached from the data I have collected in the dynamic pull-out experiment.

1) The intruder size has little effect on the form of the intruder's dynamics or the response forces in the granular system. The displacement of the intruder increases exponentially with time for various circular intruders with radii of between 3.2 and 10.2 cm. Additionally, the curvature distributions of the individual strong force chains that make up the full elastic network are the same for various intruder sizes. However, the intruder size does affect the characteristic time and prefactor of the exponential.

2) Once the intruder starts to move, the granular flow around the intruder shown by the PIV technique indicates a velocity field similar to an ideal fluid flowing around an infinite cylinder, though the PIV technique is not accurate enough to provide a quantitative description of the granular flow. However, the granular system is not a real fluid, as shown by the stick-slip phenomenon observed in the space-time plot of the average stresses in the granular material. Additionally, a hole is formed below the intruder, which represents another difference from the ideal fluid case.

3) Data from pull-out experiments done with different initial depths helped establish a model to describe the dynamics of the intruder. The success of the model in fitting the data suggests that the force exerted by the granular material on the intruder can be estimated as a constant β times the depth of intruder during the pull-out process. The model matches quite well the data I got in the

experiments, though we do not have a good understanding of the factors influencing the value of β, e.g. particles weight and interactional frictions etc. I found that β is independent of the initial depth of the intruder for deep enough buried intruder.

4) From the photoelastic response, the drag force calculated from the acceleration can be compared with the stress inside the granular material, and I find that the two are proportional. Also the Fourier spectrum of the photoelastic signal indicates "Black" noise, whose origin remains unknown to us. (The term "Black" noise refers to signals with a power law spectrum with slope less than -2.)

5) Although for rough boundaries in a certain range of system widths there is an enlargement of the critical pulling force that is needed to pull the intruder out, once the intruder starts to move under a close-to-critical pulling force, the dynamics are independent of the system width. The exponential relations between the displacement of intruder and time remain the same for runs with different initial depths and boundary widths.

6.3 Future outlook

There are many other research projects that can be done to extend the pull-out experiment results and find more applications in industry. Perhaps the priority ones that I have thought about are listed below:

1) The microscopic basis for the collective model I have used to describe the drag force here is worth exploring, as my rough model only shows that the drag force can be written as βd, where d is the depth of the intruder. There should be a more accurate and precise explanation relating the dynamics of the granular particles to the drag force.

2) Payman Jalali and Yuchen Zhao have already started work on a 3D version of pull-out experiments involving a sphere submerged in sands and glass beads. The preliminary result matches with what 2D experiments have shown: the intruder displacement follows an exponential relation with time for the dynamic pull-out experiment and the system width shows a complex effect on the critical force. Maybe a model that can universally explain the intruder's behavior in this complex granular system could be established.

3) In the 2D pull-out experiments, we use a constant weight on the thread to provide the pulling force, which changes the velocity of intruder during the pull-out process. We can also try to impose a constant intruder velocity, which will give a clue to how the velocity affects the drag force in the granular system, which may be compared to Reynolds number effects in fluids.

Bibliography

Adrian, R. J. (1991), "Particle-imaging techniques for experimental fluid mechanics," *Annu. Rev. Fluid Mech.*, 23, 261–304.

Albert, I., Tegzes, P., Albert, R., Sample, J. G., Barabási, A. L., Vicsek, T., Kahng, B., and Schiffer, P. (2001), "Stick-slip fluctuations in granular drag," *Phys. Rev. E*, 64, 031307.

Ballard, D. (1981), "Generalizing the Hough transform to detect arbitrary shapes," *Pattern Recognition*, 13, 111–122.

Blumenfeld, R. (2004), "Stresses in Isostatic Granular Systems and Emergence of Force Chains," *Phys. Rev. Lett.*, 93, 108301.

Blumenfeld, R. and Ma, J. (2017), "Bending back stress chains and unique behaviour of granular matter in cylindrical geometries," *Granular Matter*, 19, 29.

Braun, O. M., Barel, I., and Urbakh, M. (2009), "Dynamics of Transition from Static to Kinetic Friction," *Phys. Rev. Lett.*, 103, 194301.

Clark, A. H., Kondic, L., and Behringer, R. P. (2012), "Particle scale dynamics in granular impact," *Phys Rev Lett*, 109, 238302.

Clark, A. H., Petersen, A., Kondic, L., O'Hern, C., and Behringer, R. P. (2015), *Granular Impact: a grain scale approach*, Elsevier, Oxford.

Cowen, E. A. and Monismith, S. G. (1997), "A hybrid digital particle tracking velocimetry technique," *Exp. Fluids*, 22, 199–211.

Gramoll, K. (2017), *Online fluid course*, http://www.ecourses.ou.edu/.

Jaeger, H. M., Nagel, S. R., and Behringer, R. P. (1996), "Granular solids, liquids, and gases," *Rev. Mod. Phys.*, 68, 1259–1273.

Janssen, H. A. (1895), "Experiments on corn pressure in silo cells," *Engineer in Bremen, Germany*, 1045, 39.

Janssen, H. A. (1896), "On the Pressure of Grain in Silos," *Inst. Civ. Eng. Proc*, 553, 124.

Katsuragi, H. and Durian, D. J. (2007), "Unified force law for granular impactcratering," *Nature Physics*, 3, 420–423.

Kligerman, Y. and Varenberg, M. (2014), "Elimination of Stick-Slip Motion in Sliding of Split or Rough Surface," *Tribology Letters*, 53, 395–399.

Krishna, P. H. and Murty, V. R. (2013), "Pull-out Capacity of Granular Anchor Piles in Expansive Soils," *Journal of Mechanical and Civil Engineering*, 5, 24–31.

Majmudar, T. S. and Behringer, R. P. (2005), "Contact force measurements and stress induced anisotropy in granular materials," *Nature*, June, 1079–1082.

Norberg, C. (2003), "Fluctuating lift on a circular cylinder: review and new measurements," *Journal of Fluids and Structures*, 17, 57–96.

Nordstrom, K. N., Lim, E., Harrington, M., and Losert, W. (2014), "Granular dynamics during impact," *Phys Rev Lett*, 112, 228002.

Nusier, O. K. and Alawneh, A. S. (2004), "Micropile technique to control upward movement of lightweight structures over expansive soils," *Journal of Geotechnical and Geological Engineering*, pp. 89–104.

Oseen, C. W. (1910), "Über die Stokes'sche formel, und über eine verwandte Aufgabe in der Hydrodynamik," *Arkiv för matematik, astronomi och fysik, vi*, 29.

Otsu, N. (1979), "A Threshold Selection Method from Gray-Level Histograms," *IEEE Transactions on Systems, Man, and Cybernetics*, 9, 62–66.

Poncelet, J. V. (1829), *Cours de M'ecanique Industrielle*, Professé1828 à1829.

Proudman, I. and Pearson, J. R. A. (2006), "Expansions at small Reynolds numbers for the flow past a sphere and a circular cylinder," *Journal of Fluid Mechanics*, 2, 237.

Qi, J. H., Joyce, K., and Boyce, C. M. (2003), "Durometer Hardness and the Stress-Strain Behavior of Elastomeric Materials," 76, 419–435.

Sperl, M. (2005), "Experiments on corn pressure in silo cells-translation and comment of Janssen's paper from 1895," *Granular Matter*, 8, 59–65.

Stokes, G. G. (1851), "On the effect of the internal friction of fluids on the motion of pendulums," *Cambridge Phil. Soc.*, pp. 98–106.

Sumer, B. M. and Fredse, J. (1997), *Hydrodynamics Around Cylindrical Structures*, World Scientific Publishing Co. Pte. Ltd.

Tropea, C., Scarano, F., Westerweel, J., Cavone, A. A., Meyers, J. F., Lee, J. W., and Schodl, R. (2007), *Particle-based techniques*, Springer-Verlag.

Tsimring, L. and Volfson, D. (2005), *Modeling of impact cratering in granular media*, Powders and Grains.

Umbanhowar, P. and Goldman, D. I. (2010), "Granular impact and the critical packing state," *Phys. Rev. E*, 82, 010301.

Westerweel, J. (1997), "Fundamentals of digital particle image velocimetry," *Meas. Sci. Technol.*, 8, 1379–92.

Zdravkovich, M. M. (1997), *Flow Around Circular Cylinders*, Oxford University Press Inc.

Zhang, Y. and Behringer, R. (2017), "Pulling an intruder from a granular material: a novel depinning experiment," *Powders and Grains*, 140, 03040.

Biography

Yue Zhang was born on February 19, 1992 in Jingzhou, a historical city in Hubei Province of P. R. China. She graduated from Hubei Jingzhou High School in 2009. She obtained a Bachelor's degree in Nuclear Engineering, graduating from University of Science and Technology of China with honor in 2013. In the fall of 2013, she began her pursuit for a Doctor's degree in Duke Physics. She passed her Preliminary exam in April, 2016. She also obtained a concurrent Master's degree in Computer Science, from Duke University in 2018.

During her study in Duke, she joined American Physical Society and presented on March Meetings and DFD Meetings from 2015 to 2018. In 2017, she had a paper published on the 'Powders and Grains' Conference, France. More papers about pull experiments are on the way.